ABSTRACT

Title of Thesis: NONLINEAR RESPONSE OF ELECTRONIC ASSEMBLIES UNDER MULTIAXIAL VIBRATION EXCITATION

Samuel Massa, Master of Science, 2018

Thesis Directed By: Professor Abhijit Dasgupta, Department of Mechanical Engineering

Electronic packages are exposed to complex life-cycle environments, and in many cases that environment involves exposure to multiaxial vibration which can dangerously affect the integrity of the electronic package's functionality due to nonlinear amplification of the multiaxial response, in comparison to the corresponding uniaxial responses. This has particular implications in vibration durability testing of electronic assemblies, since conventional tests in industry are often run sequentially as set of uniaxial tests along orthogonal axes. This is in part because multiaxial vibration tests can be expensive and complex when the response becomes significantly nonlinear. The severity of the nonlinear response is known to depend both on the multiaxial excitation parameters and on the component architecture. Prior studies have investigated the nonlinear effects of varying the loading parameters through modeling and testing, while this study focuses on

quantifying the effects of component geometry. The approach is based on a combination of multiaxial vibration testing and modeling to conduct a parametric study with components of different geometries. The findings of this study will provide important guidance when developing guidelines about when multiaxial response is important, instead of sequential uniaxial testing along orthogonal axes.

NONLINEAR RESPONSE OF ELECTRONIC ASSEMBLIES UNDER MULTIAXIAL VIBRATION EXCITATION

by

Samuel Massa

Thesis submitted to the Faculty of the Graduate School of the
University of Maryland, College Park, in partial fulfillment
of the requirements for the degree of
Master of Science
2018

Advisory Committee:
Professor Abhijit Dasgupta, Mechanical Engineering, Chair
Professor Amr Baz, Mechanical Engineering
Professor Miao Yu, Mechanical Engineering

Acknowledgements

This paper would not be possible without the support and guidance of many people in my life.

My advisor, Professor Abhijit Dasgupta, is responsible for maintaining the direction of this project, and is vital to the discoveries made in this paper. He has handled this project through four previous graduate students, and provided guidance on all the work I completed as a part of this paper.

This thesis is a part of a continuing research project, at the CALCE lab, and all the work in this paper is based on the work of students before me. Raman Sridharan, Dr. Ed Habtour and Matthew Ernst laid the groundwork for everything presented in this thesis. In fact, much of the discovery is guided by the training and help from Raman Sridharan and Joel Hoksbergen at Data Physics Corporation.

Lastly, I could not have made it through the work for this thesis without the love and support of my fiancé, Amanda Phillips.

Table of Contents

Acknowledgements ii
Table of Contents iii
List of Tables v
List of Equations v
List of Figures vi
List of Symbols ix
List of Abbreviations xii
Chapter 1: Introduction 1
  Section 1.1: Introduction to Multiaxial Vibration 1
  Section 1.2: Introduction to Linearity and Literature Review 4
  Section 1.3: Introduction of Electronic Packaging 11
  Section 1.4: Research Goals 15
Chapter 2: Modeling of Electronic Packaging 16
  Section 2.1: Design for Modeling 16
  Section 2.2: Modeling of Mechanical Test Specimen 21
Chapter 3: Experimental Design 32
  Section 3.1: Experimental Setup 32
  Section 3.2: Test Excitation 35
    Section 3.2.1: Introduction of Vibration Control 35
    Section 3.2.2: Excitation Profile Design 38
  Section 3.3: Instrumentation 43
  Section 3.4: Test Matrix 45
Chapter 4: Experiment 48
  Section 4.1: Introduction 48
  Section 4.2: Sweep Test 48
  Section 4.3: Broadband Testing 50
    Section 4.3.1: Broadband Experimental Results 50
    Section 4.3.2: Broadband Experimental Analysis 56
  Section 4.4: 6 Hz Narrow Bandwidth Testing 61
    Section 4.4.1: 6 Hz Bandwidth Experimental Results 61
    Section 4.4.2: 6 Hz Bandwidth Experimental Analysis 64
  Section 4.5: 1 Hz Narrow Bandwidth Testing 67
    Section 4.3.1: 1 Hz Bandwidth Experimental Results 67
    Section 4.3.2: 1 Hz Bandwidth Experimental Analysis 71
Chapter 5: Finite Element Analysis of Experimental Results 80
  Section 5.1: Introduction 80
  Section 5.2: Broadband Excitation 83
  Section 5.3: 1 Hz bandwidth FEA Results 90
Chapter 6: Summary and Future Work 99
  Section 6.1 Introduction 99
  Section 6.2 Summary and Discussions 99
  Section 6.3 Research Contributions 101

Section 6.4 Limitations and Future Work 102
Appendices 104
Appendix A: Sine Sweep Test Acceleration FFT Results 104
Appendix B: Sine Sweep Test Acceleration FFT Results 106
Appendix C: Broadband Random Excitation Test Acceleration FFT Results ... 108
Appendix D: 6 Hz Bandwidth Random Excitation Test Acceleration FFT Results 110
Appendix E: 6 Hz Bandwidth Random Excitation Test Acceleration Global Percent Error 116
Appendix F: Matlab Code Excerpts 120
Appendix G: 1 Hz Excitation SOP 125
Bibliography 132

List of Tables

Table 2-1: Modeling Material Parameters 24
Table 2-2: Beam 1 Parameters for Mechanical Setup 30
Table 2-3: Beam 2 Parameters for Mechanical Setup 30
Table 2-4: Predicted Modes for Mechanical Setup 30
Table 3-1: Sine Sweep Test Matrix 45
Table 3-2: Broadband Test Matrix 46
Table 3-3: 6 Hz Bandwidth Test Matrix 46
Table 3-4: 1 Hz Bandwidth Test Matrix 47
Table 4-1: Sweep Test Result 49
Table 5-1: Broadband Random Excitation Matching Table 85
Table 5-2: Broadband Random Excitation Rayleigh Damping 85
Table 5-3: 1 Hz Bandwidth Random Excitation Matching Table 91
Table 5-4: 1 Hz Bandwidth Random Excitation Rayleigh Damping 91

List of Equations

Equation 1-1 4
Equation 1-2 4
Equation 3-1 36
Equation 3-2 36
Equation 3-3 36
Equation 3-4 36
Equation 3-5 37
Equation 4-1 56
Equation 4-2 63
Equation 4-3 63
Equation 4-4 63
Equation 5-1 82

List of Figures

Figure 1-1: Frequency Mode Shapes of Simple String....2
Figure 1-2: Six Degrees of Motion....3
Figure 1-3: Notched Beam....7
Figure 1-3: Beam with Tip Mass....8
Figure 1-4: Frequency Ratio of Component excited Sinusoidal in two axes....9
Figure 1-5: Amplitude under different excitation phases of Component excited Sinusoidally in two axes with frequency ratio of two....10
Figure 1-6: Amplification Factor changes with mass and standoff under worst case scenario of phase and frequency ratio....11
Figure 2-1: Broadband Excitation Response....16
Figure 2-2: Double Beam Mechanical Setup....17
Figure 2-3: Lead Frame Connection (Left) Comparison to Solder Bump Connection (Right)....18
Figure 2-4: Pi-Shaped Structure....20
Figure 2-5: Simple Conditions (Left) Comparison to Clamping Condition (Right)....23
Figure 2-6: Mechanical Setup Plane of Interest....25
Figure 2-7: Frequency Mode Shapes of Mechanical Setup....25
Figure 2-8: Change of Modal Frequency with changes in height of Beam 2....26
Figure 2-9: Change of Modal Frequency with changes in height of Beam 1....26
Figure 2-10: Mechanical Component Geometry Variations....28
Figure 2-11: Mechanical Setup Mode 2 Deformation Direction....29
Figure 2-12: Mechanical Setup Mode 3 Deformation Direction....29
Figure 2-13: Parametric Study Samples....31
Figure 3-1: TE6-900 Shaker....33
Figure 3-2: Experiment Fixture....34
Figure 3-3: Manufactured Sample....35
Figure 3-4: Beating from 6 Hz Bandwidth Random Excitation....40
Figure 3-5: Lack of Beating from 1 Hz Bandwidth Random Excitation....41
Figure 3-6: Square Function FFT....42
Figure 4-1: Sweep Test FFT Result....50
Figure 4-2: Random Excitation Time History....51
Figure 4-3: Sample 4 Broadband Excitation Averaged Acceleration Result....52
Figure 4-4: Sample 5 Broadband Excitation Averaged Acceleration Result....52
Figure 4-5: Sample 4 Strain Gauge FFT....54
Figure 4-6: Sample 5 Strain Gauge FFT....55
Figure 4-7: Sample 4 Broadband Acceleration FFT Normalized difference....56
Figure 4-8: Sample 5 Broadband Acceleration FFT Normalized difference....57
Figure 4-9: Broadband Random Excitation Strain Gauge Peaks Normalized difference based on FFT Resolution....58
Figure 4-10: Strain Gauge Peaks Normalized difference based on FFT Resolution....60
Figure 4-11: Broadband Strain FFT Normalized difference peaks for Tested Samples....61

Figure 4-12: Sample 2 6 Hz Bandwidth Acceleration Response Linear Superposition Estimation 1 63
Figure 4-13: Sample 2 6 Hz Bandwidth Acceleration Response Linear Superposition Estimation 2 64
Figure 4-14: Sample 2 6 Hz Bandwidth Acceleration Response Linear Superposition Estimation 3 64
Figure 4-15: Sample 2 6 Hz Bandwidth Acceleration Global Normalized difference 65
Figure 4-16: 6 Hz Bandwidth Strain FFT Normalized difference of Estimation Methods for Tested Samples....66
Figure 4-17: 6 Hz Bandwidth Strain FFT Normalized difference peaks for Tested Samples 67
Figure 4-18: Sample 2 1 Hz Bandwidth Acceleration Response.... 69
Figure 4-19: Sample 4 1 Hz Bandwidth Acceleration Response.... 69
Figure 4-20: Sample 5 1 Hz Bandwidth Acceleration Response.... 70
Figure 4-21: 1 Hz Bandwidth Strain Response.... 71
Figure 4-22: Sample 2 1 Hz Bandwidth Acceleration FFT Normalized difference ... 73
Figure 4-23: Sample 4 1 Hz Bandwidth Acceleration FFT Normalized difference ... 73
Figure 4-24: Sample 5 1 Hz Bandwidth Acceleration FFT Normalized difference ... 74
Figure 4-25: 1 Hz Bandwidth Acceleration FFT Normalized difference peaks for Tested Samples 75
Figure 4-26: 1 Hz Bandwidth Strain FFT Normalized difference 77
Figure 4-27: 1 Hz Bandwidth Strain FFT Normalized difference peaks for Tested Samples 79
Figure 4-28: 1 Hz Bandwidth Strain FFT Normalized difference peaks for Tested Samples 79
Figure 4-29: 1 Hz Bandwidth Strain FFT Normalized difference peaks for Tested Samples 78
Figure 5-1: FEA Sample Model.... 82
Figure 5-2: FEA Model Mesh.... 83
Figure 5-3: Broadband Random Excitation FEA Tip Acceleration Response FFT ... 86
Figure 5-4: Broadband Random Excitation FEA Strain Gauge FFT Response 86
Figure 5-5: Broadband Random Excitation FEA Tip Acceleration Global Normalized difference 87
Figure 5-6: Broadband Random Excitation FEA Strain Gauge Global Normalized difference 88
Figure 5-7: Broadband Random Excitation FEA Acceleration Normalized difference Peaks for Tested Samples 89
Figure 5-8: Broadband Random Excitation FEA Strain Normalized difference Peaks for Tested Samples.... 89
Figure 5-9: Broadband Random Excitation FEA vs Experiment Acceleration Normalized difference Peaks for Tested Samples 90
Figure 5-10: Broadband Random Excitation FEA vs Experiment Strain Normalized difference Peaks for Tested Samples 90
Figure 5-11: 1 Hz Bandwidth X-Axis Excitation Strain Response 92
Figure 5-12: 1 Hz Bandwidth XZ-Axis Excitation Strain Response.... 92
Figure 5-13: 1 Hz Bandwidth X-Axis Excitation Acceleration Response 93

Figure 5-14: 1 Hz Bandwidth XZ-Axis Excitation Acceleration Response 93
Figure 5-15: 1 Hz Bandwidth XZ-Axis Excitation Acceleration FFT Response 94
Figure 5-16: 1 Hz Bandwidth XZ-Axis Excitation Strain Gauge FFT Response..... 94
Figure 5-17: 1 Hz Bandwidth XZ-Axis Excitation Acceleration Normalized difference 95
Figure 5-18: 1 Hz Bandwidth XZ-Axis Excitation Strain Gauge Normalized difference 96
Figure 5-19: 1 Hz Bandwidth FEA FFT Acceleration Normalized difference peaks for Tested Samples 97
Figure 5-20: 1 Hz Bandwidth FEA FFT Strain Normalized difference peaks for Tested Samples 98
Figure 5-21: 1 Hz Bandwidth FEA FFT Acceleration Normalized difference peaks for Tested Samples 99
Figure 5-22: 1 Hz Bandwidth FEA FFT Strain Normalized difference peaks for Tested Samples 99
Figure G-1: Open File 125
Figure G-2: Setup Test 125
Figure G-3: Test Tab 126
Figure G-4: Outputs Tab 127
Figure G-5: Edit Configuration 127
Figure G-6: Inputs Tab 128
Figure G-7: Control Tab 129
Figure G-8: Profile Tab 130
Figure G-9: Profile Edit 130
Figure G-10: Measurement Tab 131

List of Symbols

Equation 1-1 through 1-2

$Output(In_1, In_2)$ –	General output function dependent on two inputs
In_i –	General input to a function
$f(In_1)$ –	General function dependent on one input
$g(In_2)$ –	General function dependent on one input
$w(In_1, In_2)$ –	General interaction function dependent on two inputs

Equation 3-1 through 3-5

$H(t)$–	Height of shaker table
H''(t)–	Second Spatial Derivative of the Height of shaker table
X–	Height Amplitude of shaker table
t–	Time
$a(t)$–	Acceleration of the shaker table

Equation 4-1 through 4-4

R_X–	1 Hz bandwidth random profile test response for an X-Axis excitation of the X-Axis natural frequency
R_Z–	1 Hz bandwidth random profile test response for a Z-Axis excitation of the Z-Axis natural frequency
R_{XZ}–	1 Hz bandwidth random profile biaxial test response for an X-Axis excitation of the X-Axis natural frequency and a Z-Axis excitation of the Z-Axis natural frequency
$R_{X(f_1)}$–	6 Hz bandwidth random profile test response for an X-Axis excitation of the X-Axis natural frequency
$R_{X(f_2)}$–	6 Hz bandwidth random profile test response for an X-Axis excitation of the Z-Axis natural frequency
$R_{X(f_1,f_2)}$–	6 Hz bandwidth random profile test response for an X-Axis excitation of both the X-Axis and Z-Axis natural frequencies

$R_{Z(f_1)}-$	6 Hz bandwidth random profile test response for a Z-Axis excitation of the X-Axis natural frequency
$R_{Z(f_2)}-$	6 Hz bandwidth random profile test response for a Z-Axis excitation of the Z-Axis natural frequency
$R_{Z(f_1,f_2)}-$	6 Hz bandwidth random profile test response for a Z-Axis excitation of both the X-Axis and Z-Axis natural frequencies
$R_{XZ(f_1)}-$	6 Hz bandwidth random profile test response for an X-Axis and Z-Axis excitation of the X-Axis natural frequency
$R_{XZ(f_2)}-$	6 Hz bandwidth random profile test response for an X-Axis and Z-Axis excitation of the Z-Axis natural frequency
$R_{XZ(f_1,f_2)}-$	6 Hz bandwidth random profile test response for an X-Axis and Z-Axis excitation of both the X-Axis and Z-Axis natural frequencies
f_1-	Transverse natural frequency of sample in the X-Axis
f_2-	Axial natural frequency of sample in the Z-Axis

Equation 5-1

$C-$	Damping Matrix
$M-$	Mass Matrix
$K-$	Stiffness Matrix
$\alpha-$	First Rayleigh Damping Coefficient
$\beta-$	Second Rayleigh Damping Coefficient

List of Abbreviations

CALCE –	Center of Advanced Life Cycling Engineering
ED –	Electrodynamic
FEA –	Finite Element Analysis
MDOF–	Multiple Degrees of Freedoms
PCB –	Printed Circuit Board
PCA –	Printed Circuit Assembly
QFP –	Quad Flat Packages
lbf –	Pound force
in –	Inch
s –	Second
SDOF–	Single Degree of Freedom
SSDOF–	Sequential Single Degree of Freedom
t –	Time
psi –	Pound per square inch

Chapter 1: Introduction

Section 1.1: Introduction to Multiaxial Vibration

The research in this paper is driven by what is the driving force for much of research: failure. Failure is defined as a product no longer having the ability to perform the function for which it is intended. When researching failure, the goal is to develop and understand the failure mechanism, the process by which the product fails. The more that is understood about the mechanism by which products fail, the better that failure can be controlled in the future. What is being described here is the physics of failure approach to reliability.

The research in this paper focuses on the failure mechanism caused by the mechanical process of vibration. Specifically, the failures cause by multiaxial vibration. As a force is applied, an object will experience a deformation. As an object continues to deform, it will reach a point where it cannot deform anymore and will fail. This failure can be reached by overstress, a single force that is beyond the yield limit for the object, or by fatigue, a cyclic force that wears the object down over time. Vibration is a cyclic motion of an object and can cause fatigue failure under a variety of conditions. In this paper, the interest is in multiaxial vibration and how it causes failure.

Since vibration is a cyclic motion, an important parameter is the frequency at which the test is run. When researching the fatigue under vibration, the frequency that will cause the most deformation is important to know. In other words, it is important to understand the natural modal frequencies of the testing setup. Using the simplest

example, imagine a string or a wire constrained on its two ends. As this setup is vibrated at any frequency, the string will deform slightly. As the frequency of vibration is increased, the string will deform more, coming to a point where the entire string moves together at a single frequency, a standing wave. This is the first natural frequency mode of the string, and has a specific mode shape. In this case, the mode shape is half a sinusoidal wave. In a similar way, if the frequency is increased even more, there will be additional natural frequency modes of vibration with unique mode shapes. This is illustrated in Figure 1-1. These natural modes of vibration occur in everything in nature and depend on the deformation geometry of the setup, the material of the object, and the boundary conditions of the setup. In this research, the modal frequencies will be defined and used in testing in multiple directions.

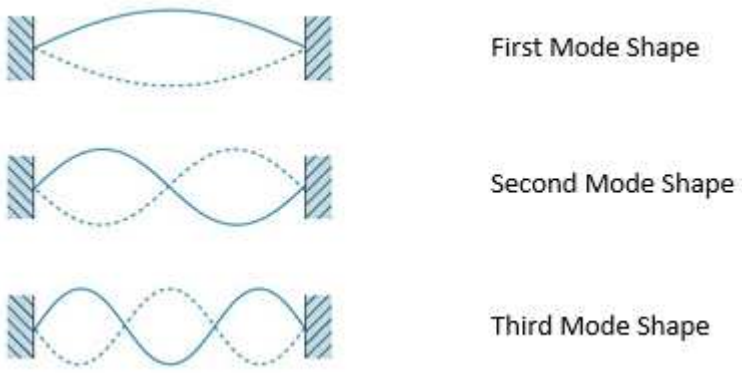

Figure 1-1: Frequency Mode Shapes of Simple String

Multiaxial vibration is when an object experiences vibration in multiple degrees of freedom. As shown in Figure 1-2, an object has six possible degrees of freedom. Three translational degrees of freedom as shown on any three dimensional graph. An object can move in plane with where it is located. For example, a phone on a desk can be slid in from side to side or forwards and backwards while remaining on

the two dimensional plane of the desk. This is two of the three translational degrees of freedom. The other translational degree of freedom is out of plane motion. For example, lifting the phone straight off of the desk. The phone has not moved from the two dimensional plane of the desk, but is translating out of the plane. The other three degrees of freedom are rotational. One rotational degree of freedom is in plane with the motion of the object. This can be illustrated by spinning the phone on the desk without it being removed from the desk. The last two rotational degrees of freedom are out of plane motion. This can be seen by rotating the phone to be standing on one of its edges. There are two degrees of freedom, because the phone can be rotated to a side or forwards or backwards to be put on its edge. In each case, the phone must be lifted out of the two dimensional plane of the desk. What is important to understand at this point is that each of these six degrees of freedom are independent of each other.

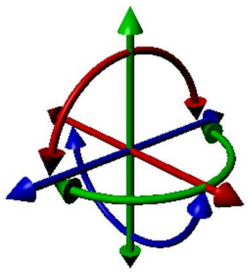

Figure 1-2: Six Degrees of Motion

A translation in plane is not dependent on a rotation out of plane. This independence means that an object can be tested independently in each of the six degrees of freedom. In the research in this paper, it can be seen that each degree of freedom is thought about, constrained if needed, and controlled wherever possible.

Section 1.2: Introduction to Linearity and Literature Review

Under a multiaxial vibration, it can be concluded that the object will then deform and fatigue in multiple degrees of freedom. The problem lies when this deformation is modelled. Is it reasonable to say that the object's deformations in each direction will be independent of all other degrees of freedom? The question posed here is a question of linearity. In a linear system, the output is a superposition of the different independent inputs. In a nonlinear system the output also involves an interaction factor of the inputs to the system. This would mean that the six independent degrees of freedom that the object can be vibrated would cause an output with some type of interaction or effect on each other. If a system behaves linearly or nonlinearly is affected by the conditions put on it. In one set of conditions, it may behave linearly, and under a second set of conditions it may behave nonlinearly.

This discussion of the conditions of linearity is exactly the focus of this paper when it comes to the subject of multiaxial vibration. There are multiple inputs into the object, and the conditions surrounding the input will then make the entire system predictable in either a linear or nonlinear model. If modelled linear, then the equation would have an output with a linear combination of the inputs.

$$Output(In_1, In_2) = f(In_1) + g(In_2) \qquad \text{Equation 1-1}$$

Conversely, the nonlinear equation would have an output that would depend on the interaction of the inputs.

$$Output(In_1, In_2) = f(In_1) + g(In_2) + w(In_1, In_2) \qquad \text{Equation 1-2}$$

This is extremely important, because if linearity of vibrational fatigue can be better understood, then failures can be more accurately predicted. There are several

agencies that have guidelines for how components should be tested to be sure of its survival under multiaxial vibration. The leader in vibration testing has been the US Military, using the guidelines in MIL-STD-810G [16]. MIL-STD-810G Method 514.6 give guidelines for sequential uniaxial vibration excitation. This means that the test includes three tests that will vibrate the component in each of the three translational degrees of freedom. These tests are run sequentially on the same component to assure that the component will withstand multiaxial excitation. While MIL-STD-810G Method 514.6 shows the current standard of vibration testing to endure multiaxial excitation, MIL-STD-810G Method 527 introduces an initial guidelines for testing under multiaxial excitation. This method has the tester develop the actual multiaxial environment that the component will experience when testing. Method 514.6 shows a linear approach to understanding multiaxial excitation. However, this method will underestimate the effect of multiaxial excitation with nonlinear responses. MIL-STD-810 understands that Method 527 will need to be updated to be able to have an effective standard for multiaxial excitation testing, but is limited by insufficient knowledge at this time. Many research publications as well as current research have started to address this limited information to understand multiaxial excitation.

When it comes to multiaxial excitation testing, there are two commonly used equipment setups that can test a component in six degrees of freedom. Habtour et al [10] outline these two equipment setups: electrodynamic/hydraulic shaker tables and repetitive shock shaker tables. Choi et al [4] demonstrates the difference between these two equipment setups. The electrodynamic shaker tables are more expensive

than repetitive shock tables, but is able to independently control each of the six degrees of freedom. The electrodynamic shaker tables are able to achieve complete controllability with at least six shakers connected to the table by a bearing system. Repetitive shock shaker tables, on the other hand, use pneumatic impactors, which are not able to completely control each degree of freedom independently.

Using these multiaxial excitation equipment setups, many research publications have focused on showing the differences between sequential single degree of freedom tests, such as MIL-STD-810G Method 514.6, with multiple degree of freedom tests. Himelbrau et al [12] conducted experimental response test and fatigue analysis under sequential uniaxial and combined multiaxial excitation. This test was done as focus on the response to spacecraft hardware. This study concluded that triaxial excitation would be two time more damaging than sequential uniaxial excitation. Whiteman and Burman [21] also conducted a test of both sequential single degree of freedom and multiple degree of freedom procedures. Their study involved running a fatigue life test under both sequential uniaxial and combined triaxial broadband random excitation on a notched cantilever beam, seen in Figure 1-3. The results of this study were that the sequential single degree of freedom tests had significantly larger time to failure then the triaxial excitation test. They also concluded that the sequence of the sequential single degree of freedom test did effect the time to failure of the beam. French et al [7] conducted a similar experiment to Whiteman and Burman. Instead of a single notched beam, the sample used by French was a double notched beam. Also, instead of broadband random excitation, French used sequential and then combined sinusoidal sweep profiles in the beams two

transverse directions. The results of this test showed that sequential single degree of freedom was more damaging than multiple degree of freedom testing under this condition. Ernst [6] also aimed to show the difference between sequential single degree of freedom and multiple degree of freedom testing. The test specimen used was a circuit card with large inductors. Ernst used broadband random excitation in the transverse direction in-plane with the circuit card, and in the axial direction out-of-plane to the circuit card. The circuit card was tested under sequential single degree of freedom, coherent multiple degree of freedom, and incoherent multiple degree of freedom random excitation. Coherence is the phase relation between the axes of excitation. The average time to failure of the inductor leads was concluded to be much larger in the sequential single degree of freedom then the other two conditions.

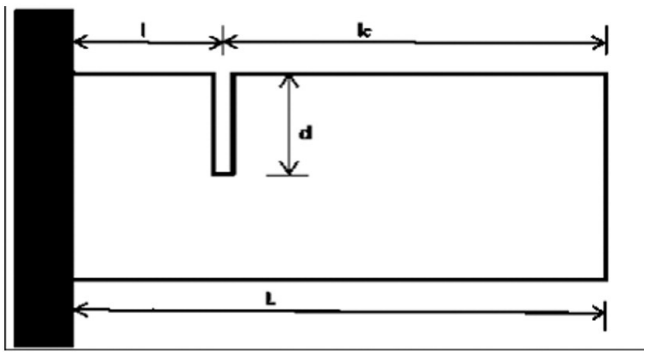

Figure 1-3: Notched Beam

These past studies have examined the differences in sequential and combined vibration testing procedures. There are also many publications that examine the difference of multiaxial and uniaxial excitation on an object. Ayen and Çelik [1] conducted a modeled study that compared the stresses seen on a helicopter component. Under uniaxial and multiaxial random excitation, Ayen and Çelik concluded the damage accumulation measured was significantly underestimated by

the uniaxial excitation. Gregory et al [9] conducted an experimental and modeled simulation of a mass at the end of a cantilever beam, as seen in Figure 1-3. Using an electrodynamic shaker, Gregory concluded that resulting strain, stress and tip acceleration are significantly different under multiaxial excitation than in uniaxial excitation. These two studies emphasize the need for multiaxial excitation testing, but do not aim to address the conditions that cause the differences in behavior between multiaxial and uniaxial testing.

In past research, the conditions under which multiaxial vibration causes nonlinear amplification has been extensively researched. This research has developed two main features that provide the highest nonlinear amplification. The first feature is through the excitation of the specimen. Given a specimen as seen in Figure 1-4, it is possible to intuitively understand this feature. If the beam is at its maximum transverse deformation, an out of plane vertical motion could reasonably add or subtract to the overall deformation of the beam. This is dependent on two factors of the excitation. The first is the frequency ratio between the out of plane axial excitation and the in plane transverse excitation. Kumar et al [14] derived equations of motion for a cantilever beam with simultaneous axial and transverse excitation, and then validated the equations experimentally. In Kumar's study, a beam was mounted at an angle on a single axis shaker. Kumar noted in the study that there was considerable nonlinear interaction when the excitations applied two sinusoids at the frequency ratio of two with the transverse frequency at the modal frequency of beam. This frequency ratio was confirmed by Ernst [6] by modeling

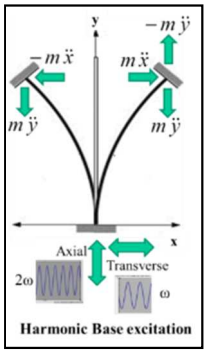

Figure 1-4: Beam with Tip Mass

biaxial excitation of a beam in the transverse and axial direction. The result, shown in Figure 1-5, found that a frequency ratio of 2N would lead to the highest nonlinear amplification, while frequency ratios of 2N-1 would have the lowest nonlinear amplification. Notice that this nonlinear amplification is either constructive, where the combined multiaxial excitation leads to higher deformation than that of linear superposition, or destructive, where the combined multiaxial excitation leads to lower deformation.

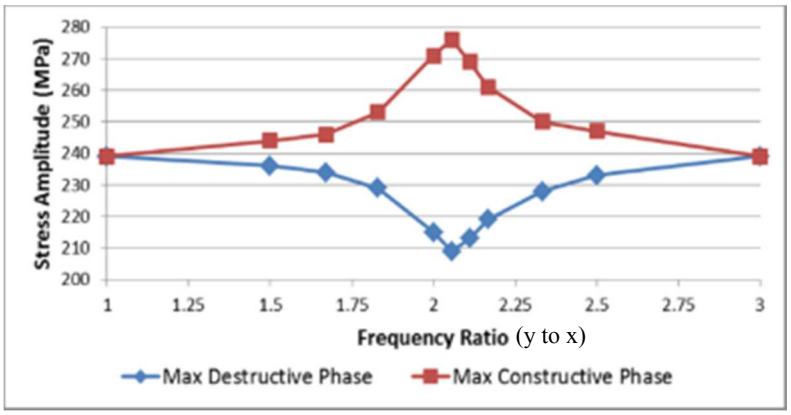

Figure 1-5: Frequency Ratio of Component excited Sinusoidally in two axes

This difference is based on the second factor of excitation that leads to nonlinear amplification: phase. Intuitively, if the example in Figure 1-4 is reexamined, the phase of the out of plane axial excitation at the maximum transverse deflection could either add or subtract to the deflection of the beam. Both Kumar and Ernst noted in their study that the deflection did change depending on the phase angle of the excitations. In his paper, Sridharan [18] quantified this by experimentally testing the effect of the phase between the transverse and axial excitation. The result of this study is shown in Figure 1-6. In red is the deflection under transverse excitation alone, and in blue is the combined biaxial excitation at different phase

angles. As shown in Figure 1-5, depending on the phase of the two excitations, there can be a constructive, destructive, or no nonlinear amplification.

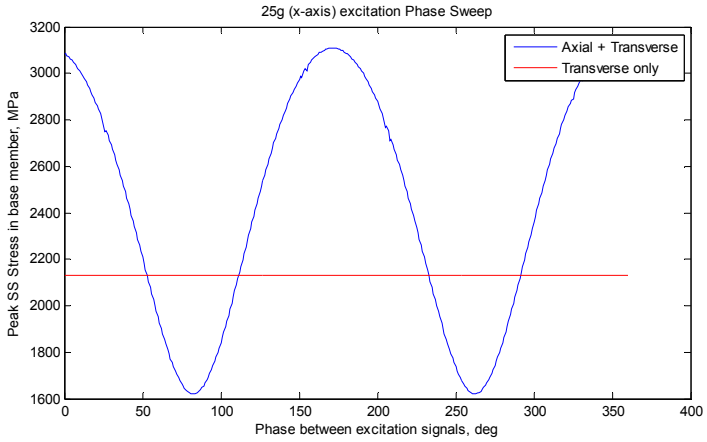

Figure 1-6: Amplitude under Different Excitation Phases of Component excited Sinusoidally in two axes with Frequency Ratio of two

While excitation has conditions that can amplify the nonlinear interaction under multiaxial excitation, the second feature is based upon the component architecture itself. The component architecture can also be design to amplify the nonlinear interaction through its modal frequency ratio. Ernst [6] noted in his study that the circuit card used in his study had a first bending mode at twice the frequency of the first bending mode of the components. Ernst noted that this characteristic perhaps increased the damage accumulation rates in the multiaxial excitation test cases. In addition to the modal frequency ratio, the component mass and height may amplify the nonlinear interaction. Sridharan [18] used the worst-case scenario of the phase and excitation frequency ratio seen in Figures 1-4 and 1-5, and modeling the amplification factor as the mass and height of the components varied. The discovery from this modeling as shown in Figure 1-7 below, is that a tall heavy component led

to higher amplification of the nonlinear effects, while smaller components had a significantly lower amplification. Sridharan was able to show the relation between mass and height of the component. There is still a gap in this literature to experimentally verify the result of the model in Figure 1-7. This study aims to fill in this gap.

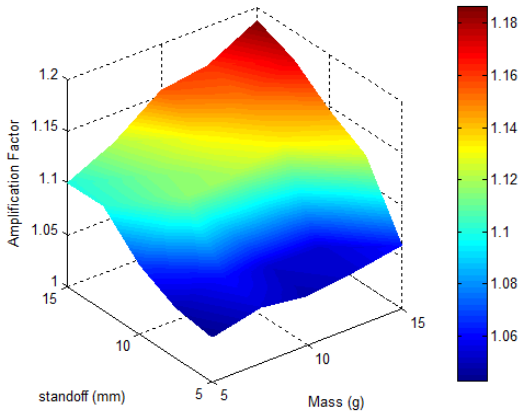

Figure 1-7: Amplification Factor changes with mass and standoff under worst case scenario of phase and frequency ratio

Section 1.3: Introduction of Electronic Packaging

A model is the solution to humanity trying to understand the world around us. For this reason, a model needs to be repeatable and reliable. A model should be repeatable by other researchers and needs to be reliable in how it predicts real outcomes. If the model is not both repeatable and reliable it fails to demonstrate the actual behavior. Looking at these two characteristics brings about the strategy of modeling in this paper. The strategy in this paper is to model the scenario in question theoretically, and then verify and refine the model experimentally. In building up the model theoretically, the steps must be repeatable to yield the same result and be

reliable to be accurate when testing the scenario experimentally. Specifically, the research will start with the design modeling of the system, where the system is modelled theoretically to fit the understanding of the "real world" scenario. This is followed by experimentation of the system by manufacturing real prototypes that simulate the "real world" scenario to help understand if the model does fit the real output of the system. Finally, the research is concluding with remodeling of the system to refine the model so that it is more reliable when predicting real life behavior.

For whose benefit is this research serving, and what scenario has been chosen to model? In the Center of Advance Life Cycling Engineering (CALCE) at the University of Maryland, the focus is on the reliability of electronic packages. Electronic packages are susceptible to a variety of failures including mechanical and thermal fatigue, electromigration and electrochemical migration, and many others. The goal of the CALCE lab is to use the physics of failure approach to understand these failure mechanisms when it comes to the practical application of electronic packaging. In this paper, the focus is on the multiaxial vibrational fatigue of electronic boards. Moreover, this paper aims to find the conditions under which multiaxial vibrational fatigue of electronic boards can be seen as linear or nonlinear.

Why is it important to examine the failure mechanisms of electronic packaging? Electronics are a growing field and are integrated into more and more of our everyday objects. In addition, electronics are relied on to be functional for much of societies need, whether it is staying warm in a building during winter or keeping our troops overseas safe. As electronics are relied on more, their functionality

becomes even more critical, because failures in electronics will have growing consequences. As discussed in the previous section, there are multiple ways to amplify the nonlinear interaction based on multiaxial interaction. This amplification has an exaggerated effect on the life of the electronic component. In fact, a constructive nonlinear interaction will result in a factor of five on its effect on the lifetime of the component. Understanding nonlinear interactions and how electronics fail from them will help to better design electronics in the future and control the failures that occur.

On an electronic package, there are two main parts of interest. The first is the printed circuit board, PCB. A PCB is the core to an electronic package that integrates all electronic components together to serve the purpose needed of it. The second is the electronic component itself. There are many different types of electronic components that incorporate many technologies depending on the development of the manufacturer, and the functional demand of the component. These electrical components have connection points that are connected to the PCB. These connection points can be either leaded or unleaded. A leaded connection originates from a lead frame, a conductive connection between the connection ends and the electrical component center, and usually protrudes off from the end of the electrical component.

These connection points of the electrical components are integrated to the PCB by two major ways. The first is by mounting the electronic component to the surface of the PCB. This is a matured technology, has been around long enough to develop methods to avoid major issues from initial development. This integration also has multiple subcategories that have been used in many practical application. These

subcategories include through-hole mounting, leaded surface mounting, and solder bump surface mounting. As its name suggests, a through-hole connection is where the leads of an electronic component are mounted to a hole in the PCB. Leaded surface mounting connection the leads of an electronic component directly to conductive pads on the surface of the PCB. Bump solder mounting connections the unleaded ends of an electronic component to conductive pads on the surface of the PCB. The second major way electronic components can be integrated is through embedded components. Embedded components integrate the electronic component inside of the PCB as opposed to having the component protruding from the surface. This is a newer technology, which is not incorporated into as many designs as mounting technology. It is a technology that may be important in the future, but is not the center of this research.

When it comes to vibrational reliability of electronic packages, the objects of vibration are the electronic components mounted on the PCB as well as the PCBs themselves. In this research, the focus will be on designing a simplified model of a mounted component on a PCB to understand the vibrational behavior of electronic packages.

Section 1.4: Research Goals

The research begins with the design of a mechanical system whose vibration response is intended to serve as a proxy for the dynamic response of electronic printed wiring assemblies (PWAs), when subjected to multiaxial vibration. As discussed in detail later, the specimen will consist of two orthogonal nonlinear beams,

where beam 1 will represent the deformation of the PWB and beam 2 will represent the deformation of the component. The design of this mechanical system will be guided by finite element dynamic simulations. The modal deformation shapes and natural frequencies of the system will be determined, based on the geometry of the specimen, the material of the specimen, and the boundary conditions of the setup. The specimen design will be systematically varied as discussed below, to generate multiple configurations. These configurations are intended for a parametric experimental study, to explore systematic variation of the amplification of nonlinear deformation of the two beams under multiaxial vibration.

These desired design features include the ability to be excited along two orthogonal axes at a frequency ratio of two. As discussed in detail later, this is accomplished by assuring that each configuration has the modal frequency ratio of two between the axial and transverse deformation modes of beam 2. These samples will be fabricated and subjected to biaxial vibration. The response of the specimen to biaxial vibration will be investigated. The nonlinearity of the response of each sample will be assessed by testing the samples using a variety of excitation profiles and conclusions will be drawn about the effects of PWA architecture on the nonlinear effects in electronic PWAs subjected to multiaxial vibration. This information will then help assess how to best design electrical components to withstand vibration in order to increase the overall life of the electronic assembly.

Chapter 2: Modeling of Electronic Packaging

Section 2.1: Design for Modeling

When a model is made to simulate vibration of electronic packaging, it must realistically model the vibration of both the PCB and the electronic component. There are a variety of components, assemblies, and packages mounted to PCBs. In his paper, Habtour [11] demonstrated nonlinear effects in electronic packages, as shown in Figure 2-1. The red curve shows the superposition of the in plane and out of plane response, while the green curve shows the experimental result of biaxial excitation. It is clear that the biaxial excitation led to a much higher excitation of the specimen. The driving factor of that research was that tall, heavy components will exhibit nonlinear effects. Since component mass and height are obvious determinants of the degree of nonlinearity, those driving factors will be parametrically examined to confirm and quantify their effect. In other words, this research will be examining specimens that represent components with a variety of heights and masses, to quantify the severity of nonlinear effects for each condition. In this way, the conditions under which nonlinearity can be minimized will be known.

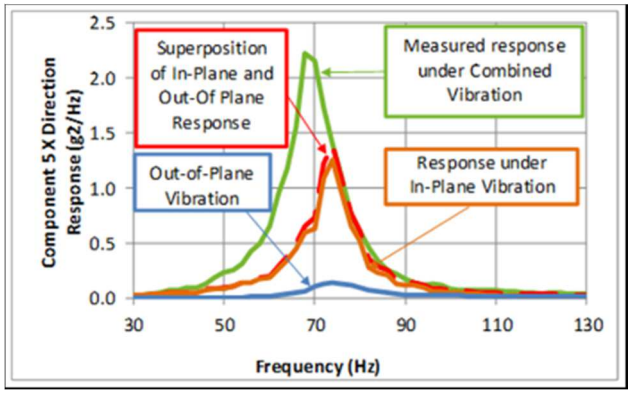

Figure 2-1: Broadband Random Excitation Response

The factors of importance are the mass of the electrical component and the height of the component from the PCB, and therefore those are the factors of consideration when determining the manner of modeling the system. Experimentally, this will be modelled in a simplified mechanical way. This mechanical model is shown in Figure 2-1. The failure mechanism that is of interest is mechanical and not electrical functionality. Since the failure mechanism is mechanical, it is purely the mechanical behavior of the system that is being researched. If a printed circuit assembly, PCA, is imagined with an array of components this can be simplified to just the in plane deformation. From this plane it can be further simplified to a single component on a PCB. Therefore, the mass and height can be varied easily and the behavior of the mechanical system can be seen for each condition. For the model to be accurate it must resemble an electronic component on a PCB. In this mechanical setup the system is modeled as a double beam. The first beam is to represent the PCB and the second beam is to represent the component mounted on the PCB. On the top of the second beam will be a varying point mass. This model is a purely mechanical way to relate to an electronic board with important emphasis on the mass and height of the component.

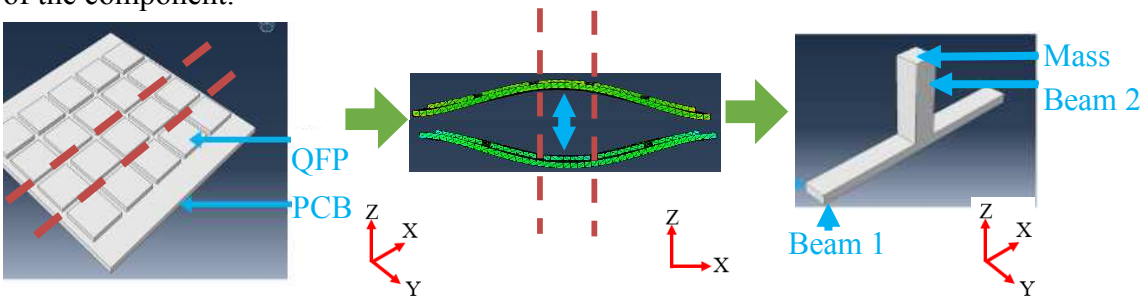

Figure 2-2: Double Beam Mechanical Setup

As discussed in Section 1.3, the surface mounted electronic components on PCBs are mounted in one of two subcategories. These subcategories are leaded

component connections and solder bumped connection. As shown on the left of Figure 2-2, a leaded component has a metal connection, called a lead frame, which is integrated into the assembly of the component. The solder bumps serve the same purpose as the leads to connect the electrically functioning component to the PCB. The difference is that the solder bumps are not integrated into the assembly of the component, but act as conductive glue between the component and the PCB. For this reason, a leaded component relates more to the double beam setup, since it is more of a uniform part.

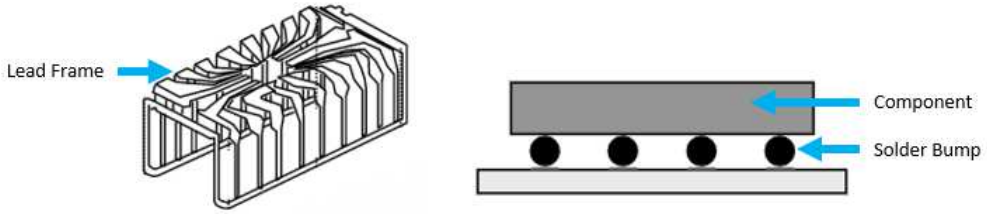

Figure 2-3: Lead Frame Connection (Left) Comparison to Solder Bump Connection (Right)

The goal of the double beam model is to be a simplified model to observe mechanical behavior of electronic components. The limitations of this research are based around what practical application the simplest mechanical model of a double beam setup can relate to. The benefit of this research is that with a modified model to fit the practical application, the same steps can be taken to observe and design electronic components resilient to harmful nonlinear effects.

Since the double beam is simplified, it is important to understand what practical applications it best relates to and how the model might be modified to fit other practical applications. The double beam is a uniform part. In this way, an

electrical component that is near uniform will fit the model better. At a component level, a leaded component relates better to the uniform double beam setup, because solder bumps have different mechanical behavior then a lead frame. This is seen from the material and geometric differences between the electronic component and the solder bumps, which lead to differences in overall behavior including coefficient of thermal expansion (CTE) mismatch. A model that may be worth pursuing in the future is a stacked double beam that includes a softer metal such as aluminum on the bottom layer, and a stainless steel layer above it. This would relate better to a solder bumped part. On a connection level, the mechanical model will be made as a uniform part without any glue connection between the two beams. In the same way the practical application will relate better to a fully integrated electronic component and PCB. A through-hole component is integrated into a PCB more than a surface mounted part. A model to relate to a surface mounted part that may be worth pursuing in the future is a surface mounted second beam.

Similar to how the double beam is simplified on a connection and integration level, the double beam model is also simplified in overall geometry. A beam is not the exact shape of an electronic part, but is a crude estimate of an electronic part. For further research a better mechanical model of an electric component, may be considered. One way to do this is to use a pi-shaped structure, shown in Figure 2-3. Discussing the dimensions of the pi shape, there are two upright beams and one horizontal beam. The two upright beams simulate the leads from the electronic component, and the horizontal beam represents the epoxy and die structure of the electronic component. The two upright beams, representing the same part of the

electronic component, should have the same dimensions. The rest of the dimensions are variable depending on what the goal of the research is. In this paper, this model was decided against for two reasons. The first is manufacturability. The manufacturing of this part is a lot more difficult than a single beam. The second reason is the goal of the research. As will be discussed later, the goal of this research is to design a mechanical layout that will complement the nonlinear behavior so that it will be easier to observe. When trying to fit the pi structure to our design criteria to complement the nonlinear behavior, it did not fit a parametric study as clear as the single beam.

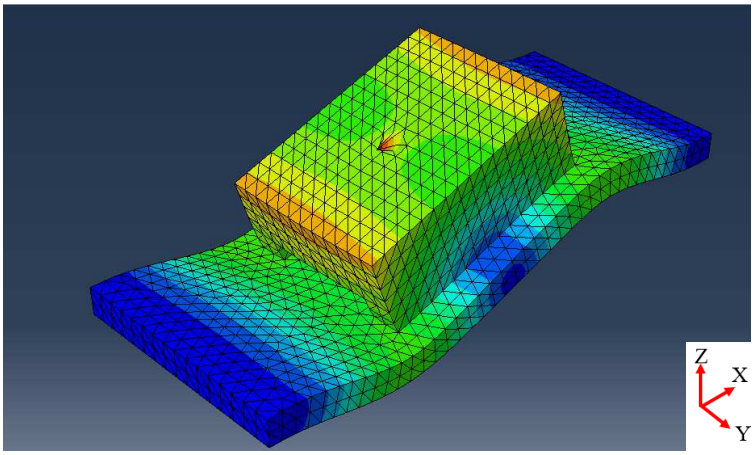

Figure 2-4: Pi-Shaped Structure

In summary, this research is focused on the mass and height of electronic components on PCBs and how they affect the nonlinearity of multiaxial vibrational response and resulting fatigue damage. This will be examined by observing mechanical behavior of a double beam model that is intended to be a dynamic proxy for electronic PCAs. The double beam model fits the application of a through-hole leaded component, but can be modified in geometry, connection, or material for

future research to better understand other PCA configurations. The double beam model for this paper will first be modelled using finite element method to predict the experimental behavior and understand the overall result. Then, the models will be fabricated and tested. From this process, the effect of mass and height on the nonlinearity of multiaxial vibrational response (and fatigue) will be concluded.

Section 2.2: Modeling of Mechanical Test Specimen

As discussed in Section 2.1, the test specimen for this study is a purely mechanical setup. When designing the parameters for the double beam setup, the conditions of the real life scenario as well as the geometric constraints of the testing setup can help provide constraints for the different design parameters.

The manufactured samples will be mounted on a multiaxial degree of freedom shaker table. This table has holes 2.5 inches and 5 inches apart. For the sample to fit on the fixture for the shaker table, the fixture should be designed to have holes 5 inches apart. Since the length of the first beam is very important to the vibrational response, this dimension will be a variable that is changed over the parametric study. For this to be possible, the fixture must have slot holes 5 inches apart to allow for variable beam lengths. The width of the beam also needs to be considered. If the beam is wide enough, it will start to act as a plate rather than as a beam. Since this study needs to eliminate plate vibration modes, the width needs to be small enough to be suitable for this research, but large enough to fit the second beam.

The width of both Beams 1 and 2 in Figure 2-2 are equal and are kept constant for all samples, to prevent this from affecting the differences in vibrational response. The first beam (horizontal Beam 1 in Fig 2-2) should resemble a slice segment of a

PCB so it should have a thickness that is approximately comparable to that of a PCB. PCBs have a variety of thicknesses depending on the core thicknesses and number of pre-impregnated layers. The range of the thickness of a PCB is usually between .0079 inch and .125 inch.

The second beam (vertical Beam 2 in Figure 2.2) is intended to serve as a mechanical proxy for an electronic component. Therefore, when designing Beam 2 of the model, it is important to focus on the factor that is being studied. In this case, the factor of interest is the height and mass of the electronic part. The length of Beam 2 is therefore systematically varied in the samples that are made. There are many sizes of electronic parts, but many have a relatively square shape. To making the mechanical model comparable with these electrical components, the second beam is designed to have a square cross-section and the height of the second beam is allowed to systematically vary across the test samples to be fabricated for the experimentation. The last parameter to be discussed is the magnitude of the point mass at the tip of the second beam. The point mass for the experiments reported here consist of the mass of the accelerometers used. This will be discussed in more detail later in Chapter 3. The dimensions being varied for the experimental parametric study are the height of the second beam and length of the first beam, and their values are guided by parametric simulation.

When designing the double beam setup, a parametric studies is needed. The parametric study first discovered the modes of vibration as well as how the geometry affects the modal frequencies and corresponding mode shapes. The parametric study then is used to determine the actual geometry of the samples manufactured for

experimenting. When running the modal analysis the boundary conditions of the test need to be determined. Simulating an electronic component on a PCB, the first beam will be constrained, while the second beam will be free. Since the initial goal parametric study is to understand behavior of mode frequencies and mode shapes it can have more general boundary conditions of constraining the ends of beam 1 as shown on the left in Figure 2-5. However, the boundary conditions of the actual experimental setup needs to be replicated when selecting accurate design parameters by clamping the two ends of beam 1 as shown on the right in Figure 2-5. The amount of clamping given on each side of the beam by the fixture used for experimenting is an inch, so the modal analysis when selecting design parameters also shared the same parameter.

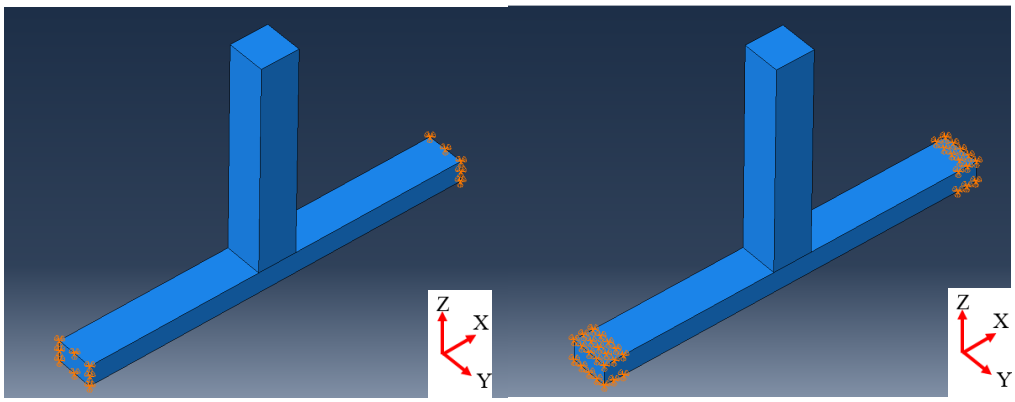

Figure 2-5: Simple Conditions (Left) Comparison to Clamping Condition (Right)

The finite element analysis, FEA, was done on the Abaqus platform. The material being modeled is Aluminum 6061, which was used to manufacture the samples in the experiments. The material properties used in the FEA modeling of Aluminum 6061 are showed in Table 2-1 below. The units used were pound force (lbf) and inches (in). Therefore, the mass density was given in pound force seconds

squared per inch to the fourth power, mass is given in pound force seconds squared per inch, and the elastic modulus was given in pound force per inches squared (psi). The mesh elements were hexahedrons with an element size of one 32nd of an inch. The point mass was placed at the center node of the top of the second beam. The specimen was constrained on the top and bottom surface of the first beam over the length of one inch, or over 32 nodes. This gives a total of 1,024 nodes constrained in all axes for each sample.

Parameter	Units	Value
Mass Density	lbf	0.0002536
Young's Modulus	s^2/in^4	10,000,000
Poisson's Ratio	psi	0.3

Table 2-1: Modeling Material Parameters

The results of the parametric study showed interesting behavior when it came to both the mode shapes as well as modal frequencies. As the geometry changed on the double beam setup or the pi-shaped stucture was used instead, there were three distinct mode shapes. The fourth mode in all seventy iterations of design had a shape with a mode frequency an order of magnitude larger than that of the third mode frequency. Since the frequency for modes beyond the third mode are so high, the higher modes are not important to this study. This is because they not only do not offer as much useful information on the nonlinear behavior of the setup, but also these modes are not sufficiently excited during the experimentation.

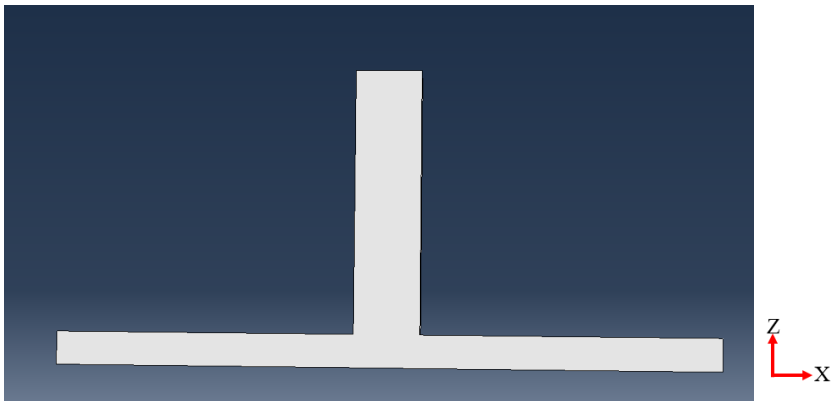

Figure 2-6: Mechanical Setup Plane of Interest

The modal frequencies of the first three modes change with the geometry of the double beam, but the mode shapes themselves are relatively constant and unchanging. As discussed in the introduction, this study focuses on motion in the xz plane as shown in Figure 2-6. Any motion in the y direction is considered out of plane. The first mode shape of the mechanical specimen discussed here is out of plane vibration of the second beam. The second mode shape of the mechanical setup is in-plane vibration of the second beam. The third mode shape of the mechanical setup is in-plane vibration of the first beam. All three of these modes are illustrated below in Figure 2-7.

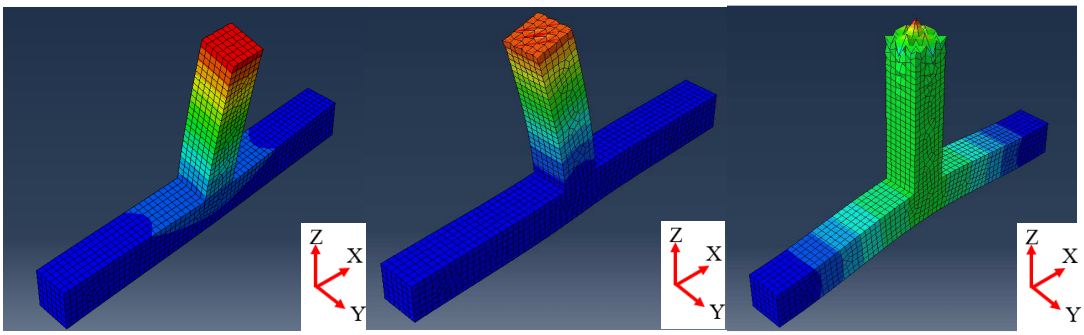

Mode 1 Mode 2 Mode 3

Figure 2-7: Frequency Mode Shapes of Mechanical Setup

As the height of the second beam and length of the first beam are varied over the course of the first parametric study, the frequencies of the three main mode drastically change. This is illustrated in the graphs in Figures 8 and 9. Figure 8 shows how the three modes change with the height of the second beam. As seen, frequencies of Modes 1 and 2 are significantly more sensitive than that of Mode 3, to the height of the second beam. Figure 9 shows how the three modal frequencies change with the length of the first beam. In contrast with Figure 8, modal frequencies for Modes 1 and 2 are significantly less sensitive than that of Mode 3 to the length of Beam 2 These two behaviors can be utilized to fit all of the design criteria.

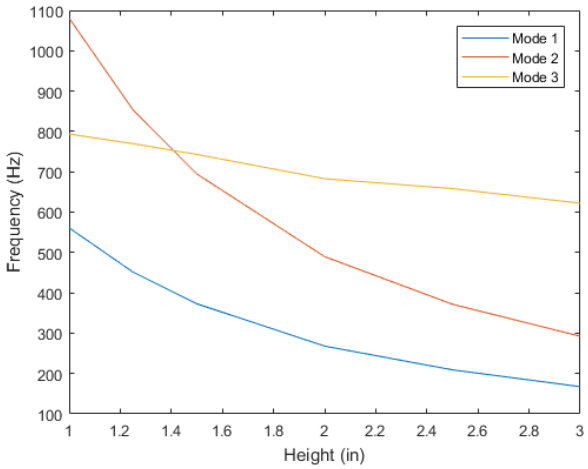

Figure 2-8: Change of Modal Frequency with changes in height of Beam 2

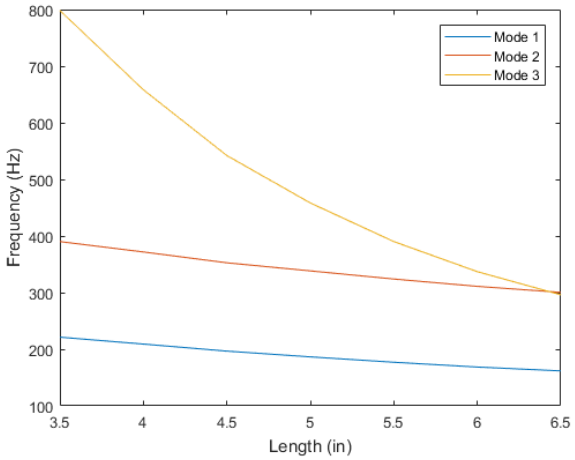

Figure 2-9: Change of Modal Frequency with changes in length of Beam 1

When it comes to the nonlinear behavior of the tip of the second beam, the in plane vibrational mode shapes are the modes of interest. The in plane vibration mode of the second beam allows the tip to experience mostly translational vibration with relatively small rotational vibration. The in plane vibration mode of the first beam allows the tip to experience pure translational vibration in a different degree of freedom. The out of plane vibration mode of the second beam acts similar to the in plane vibration mode of the second beam in that it also allows the tip to experience translational and rotational vibration in a different degree of freedom. In this research, the focus is to combine two of the vibrational modes without the influence of the third mode of vibration. This is the first constraint that the model analysis has on the design of the double beam. There are two ways to avoid the influence of the unwanted first mode of vibration (out-of-plane mode). The design goal should be to either decrease the frequency of the unwanted out-of-plane mode to a value far lower than that of the first two in-pane modes, or increase the frequency of the unwanted out-of-plane mode well beyond the other first two in-pane modes.

This first constraint was the most difficult to satisfy. When changing the geometry of the double beam it was fairly simple to have the out of plane mode be lower than the in plane modes. The problem came when the design needs to be changed to increase the out of plane mode to higher than the in plane modes. The reason why this was important is because theoretically a lower frequency mode is more likely to influence the results than a higher frequency mode. The best design for a double beam increased the out of plane mode to the same frequency of in plane mode of the first beam. This is not preferable to having a lower frequency because it

will be sure to influence results if it is the same frequency of the modes of interest. This is where the overall geometry of the second beam is called into question. The other geometries, as shown in Figure 2-8, explored were the pi structure, plate, and a dual-trapezoid, but neither solved the problem of the out of plane vibrational mode. This, therefore, shows another limitation to this research. In subsequent research, a geometry should be found that both matches the characteristics of the electronic part as well as avoids the influence of unwanted out-of-plane mode of vibration.

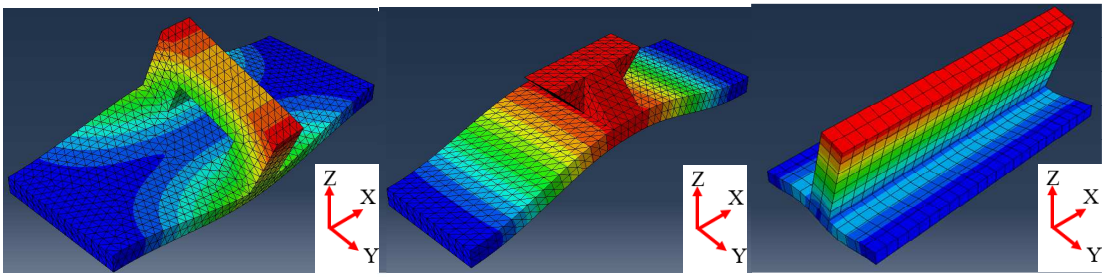

Pi-Shaped Dual Trapezoid Plate

Figure 2-10: Mechanical Component Geometry Variations

The other consideration to the design for nonlinear behavior is based on how the mode shapes compliment nonlinear behavior. The in plane vibrational modes cause the displacement in two different degrees of freedom. The combination of these modes could either cause linear or nonlinear behavior depending on the deformation of one mode becoming dependent on the other mode. If the behavior is linear, then the combination of the two mode shapes will yield a displacement of the tip as a linear combination of the two directions. In other words, the combination of the two modes will have the tip move in a single translational degree of freedom in a different coordinate system. If the behavior is nonlinear, then the displacement of the first beam will either increase or decrease the displacement of the second beam. The

frequency of the two modes are what will effect this behavior change. If the frequencies are close to each other, then it is more likely that the combination will be linear. Therefore, the second constraint to the design for nonlinear behavior was chosen to set the mode frequency of the in plane vibration mode of the first beam as twice the frequency of the in plane vibration mode of the second beam.

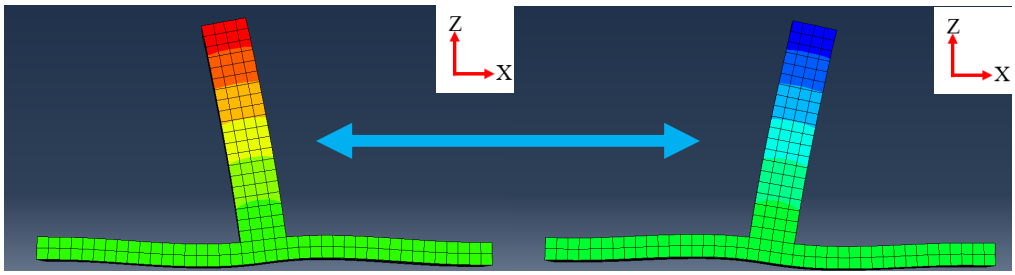

Figure 2-11: Mechanical Setup Mode 2 Deformation Direction

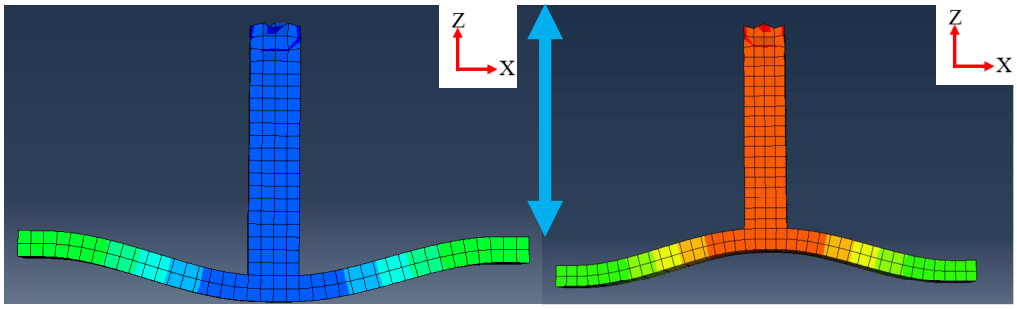

Figure 2-12: Mechanical Setup Mode 3 Deformation Direction

After understanding the behavior as well as the design constraints for the double beam setup, the specific setups for experimenting can be made. A set of five beam widths were chosen for the first beam, and the heights were determined. The parameters for each setup is listed in Tables 1, 2, and 3 below. The length of the first beam is varied from 4.25 inches to 8 inches, and the height of the second beam is varied from 1.5 inches to 4.5 inches. Based on these parameters the predicted modal frequencies ranges from 82 to 1777 Hertz (Hz). This fits the design criteria to be an

observable frequency that can be excited on the multiaxial degree of freedom shaker (which has a frequency ranges from 10 to 2000 Hz).

Beam 1	Sample 5	Sample 4	Sample 3	Sample 2	Sample 1
width (in)	0.25	0.25	0.25	0.25	0.25
height (in)	0.125	0.125	0.125	0.125	0.125
length (in)	8	7	6	5	4.25

Table 2-2: Beam 1 Parameters for Mechanical Setup

Beam 2	Sample 5	Sample 4	Sample 3	Sample 2	Sample 1
Width (in)	0.25	0.25	0.25	0.25	0.25
Height (in)	4.5	3.625	2.875	2.125	1.5
Length (in)	0.25	0.25	0.25	0.25	0.25

Table 2-3:Beam 2 Parameters for Mechanical Setup

Predicted Modes	Sample 5	Sample 4	Sample 3	Sample 2	Sample 1
Mode 1 (Hz)	82.515	118.69	176.06	292.04	499.39
Mode 2 (Hz)	143.89	207.71	308.67	513.02	884.07
Mode 3 (Hz)	283.93	408.78	623.82	1075.5	1777.3

Table 2-4: Predicted Modes for Mechanical Setup

The design from Abaqus, can be seen in Figures 13. The individual sample mode shapes are seen in Appendix A. This parametric experimental design has a broad range of height of components, lengths of beam, and frequencies of vibration. The coherence of the design is seen as all setups have the same three mode shapes, which are designed to a value where Mode 3 is twice the frequency of Mode 2. This truly allows fine tuning of the conditions under which nonlinear behavior exist.

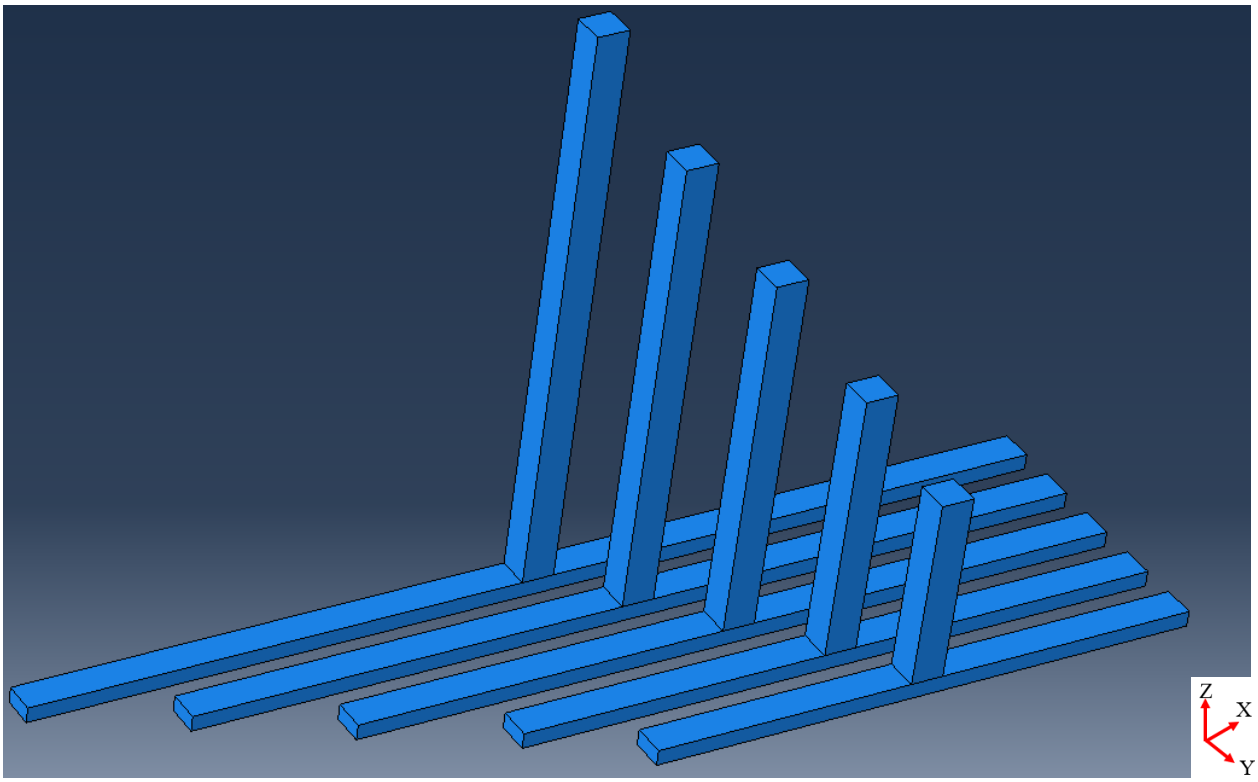

Figure 2-13: Parametric Study Samples

Chapter 3: Experimental Design

Section 3.1 Experimental Setup

In the sections above, the focus has been on modeling conducted for design of the test samples. In this chapter, the setup of the experiment will be described. In this way, a reader will understand and be able to repeat both the design and experiment. The main layout of the hardware of this experiment has three physical components. Each of these components helps to put the specimen under the experimental condition that can be parametrically changed based on the specimen, and place the samples under multiaxial vibration needed to demonstrate relevant results.

The first physical component is the six degree of freedom shaker. The TEAM TE6-900 six degree of freedom shaker, as seen in Figure 3-1, is used to control the vibration input to the samples for this experiment. The multiaxial shaker includes twelve electrodynamic (ED) actuators to control each degree of freedom independently relative to the center of gravity of the table, and four triaxial accelerometers to observe the motion of the table. There are four ED actuators in each direction, providing a force of 50 lbf each. These actuators are equidistant from the center of gravity of the table. All ED actuators push on the table by way of a hydrostatic pad bearing. In this way, the only direction the table will move from the force of the ED actuators is in the direction these actuators are mounted. A triaxial accelerometers sits on each of the shaker table's corners. This allows an accurate measurement of the motion of the center of gravity of the table to give an accurate transfer matrix to control the table. In this closed loop system, the actuators will attempt to match the output vibration of the table to that of the input vibration profile

provided by the user, and adjust the output based on the measurements from the table accelerometers. With this control setup of the test, the TEAM TE6-900 is observable and controllable in six degrees of freedom with an accurate feedback loop from the four triaxial accelerometers.

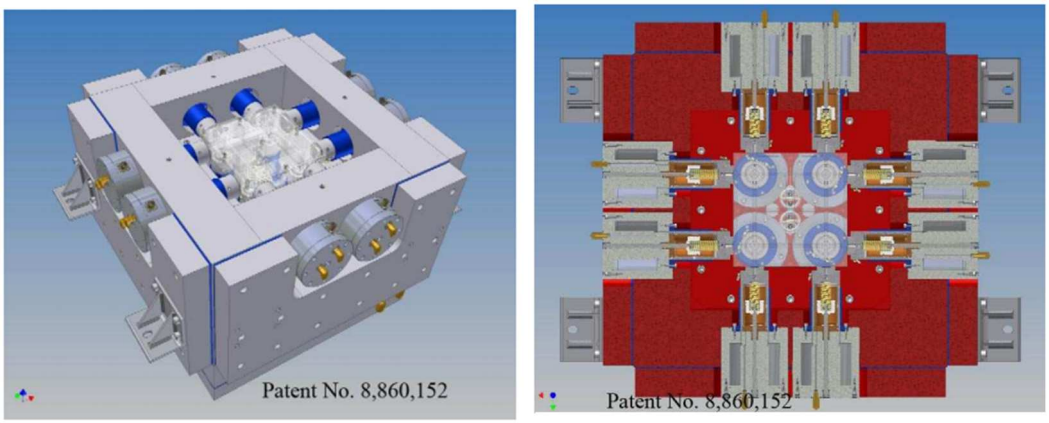

Figure 3-1: TE6-900 Shaker

The second physical component is the fixture. Fixture design is very important to the integrity of the experiment, because it sets the boundary conditions of the samples. Each of the samples need to be constrained on both ends but still be vibrated at those ends. With only screw holes in the shaker table, for this boundary condition to be met a fixture is needed. The fixtures acts as an adapter plate between the shaker table and all of the test samples and has a design goal of transmitting the shaker excitation to the test specimen without distorting the excitation signal. When designing the fixture, it must (i) be able to constrain the samples on their edges; (ii) have sufficiently adjustable geometry to fit all the samples; (iii) not have vibration modes of its own within the range of excitation frequencies.

Figure 3-2: Experiment Fixture

As seen in Figure 3-2, the designed fixture satisfies all of the features needed to be successful in this experiment. The finite element analysis, FEA, for the samples allows for one inch of clamping. Since the samples need to be constrained on both ends, two clamps with a thickness of 1 inch are used, which clamp down on the sample with the screws on either end. The designed specimens come in a variety of lengths from 4.25 to 8 inches. The fixture is designed in two halves with a slot hole so that the fixture can be mounted on the shaker table at an adjustable separation between the two halves. The TE6-900 shaker table has holes 2.5 inches and 5 inches apart. The fixture has holes 5 inches apart to allow it to be fully constraint to the shaker table with a symmetry across the centerline of the shaker table.

The final physical component, as discussed in the Chapter 2, is the designed samples. The samples are designed for manufacturability, as well as dynamic similarity to printed wiring assemblies (PWAs). An important design feature is that the double beam is to be a single part instead of using an epoxy to connect two separate beams. This is done by first using aluminum, provided by McMaster-Carr, with the exact length and thickness of the first beam. The mill is used to cut an H-shape first and then cutting the top of the H-shape of at the specific height of the beam. The one limitation of milling the samples is the existence of a fillet at the

junction between beams. The fillets are kept at a consistent eighth of an inch radius across all samples.

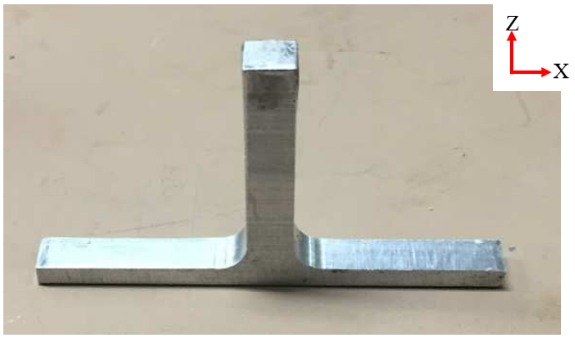

Figure 3-3: Manufactured Sample

In summary, the experimental setup starts with the vibrational control of the TE6-900 six degree of freedom shaker. The shaker has a table where the two halves of the test fixture are mounted at a varying degrees of separation, depending on the geometry of the specimen being tested. The specimen itself is then clamped to the shaker table by way of the experimental fixture. In this way, the experiment matches an FEA model of a sample clamped and shaken at its edges.

Section 3.2 Test Excitation

Section 3.2.1 Introduction of Vibration Control

While Section 3.2 discussed the hardware of the experiment, the software setup of the experiment still needs to be discussed. In this section, the vibration input into the TE6-900 by the Signal Star software will be discussed in an effort to form a multiaxial vibration test matrix for this experiment. The first thing to understand is that two type of vibration profiles can be input into the TE6-900.

The first type is a sinusoidal profile. With a sinusoidal profile, the shaker table is shaken at a single frequency. For example, if an input of 100 Hz is used at an amplitude of 1 g in the Z-Axis, the four Z-Axis actuators will fire to lift the table to a specific peak height and then retract to a specific trough height 100 times per second. The maximum vibration amplitude that the actuators can achieve is dependent on the frequency input as well as the acceleration input. Illustrating this, the example given would have a height the follows the following equation:

$$H(t) = X\,Sin(100t) \qquad \text{Equation 3-1}$$

Differentiating this equation twice will yield the acceleration of the table, given in the following equation:

$$H''(\mathrm{t}) = -X\,100^2\,Sin(100t) \qquad \text{Equation 3-2}$$

Equation 3-2 is set equal to the input acceleration into the Signal Star software, shown in Equation 3-3 below:

$$a(t) = (1\ g)\,Sin(100t) \qquad \text{Equation 3-3}$$

In this way, the specific peak and trough height of the shaker table for a sinusoidal profile is given by:

$$X = \frac{Acceleration\ Input}{(frequency\ input)^2} \qquad \text{Equation 3-4}$$

In summary, the sinusoidal profile uses an acceleration and frequency input to shake the table at the specified frequency.

The second type of vibration input profile is a random profile. Under a sinusoidal profile, the shaker will shake the table at a single frequency. Under random vibration, each frequency value the shaker can vibrate at is placed in a frequency bin. The user will then select a range of frequency bins that will all be used to vibrate the

table. As an example, imagine if the user wanted to vibrate the table at a range of 100 to 200 Hz in the Z-Axis at an amplitude of a constant 1 g. The software would split the 100 Hz range into a series of frequency bins. So the sake of this illustration, let's assume for this case there are 4 bins of 25 Hz each. The motion amplitude of the Z-Axis accelerometers will then be given by the following equation:

$$H(t) = X_1 Sin(100t) + X_2 Sin(125t) + X_3 Sin(150t) + X_4 Sin(175t) + X_5 Sin(200t) \quad \text{Equation 3-5}$$

Instead of a single sinusoid as seen in Equation 3-1, the height incorporates a series of sinusoids based on the amount of frequency bins. The coefficients are determined based on the amplitude input by the user. The result is a seemingly random excitation profile that incorporates a range of frequencies specified by the user. A profile incorporating a wide range of frequencies is considered a broadband random excitation profile, while a profile with few frequency bins is considered a narrow bandwidth random excitation profile.

This paper incorporates three multiaxial vibration strategies. The first is a broadband random excitation profile. The second is a narrow bandwidth random excitation profile. The third is a new vibration testing strategy for the 6 DOF shaker, where the random excitation profile is manipulated to simplify the table displacement equation from Equation 3-5 to the sinusoidal height equation in Equation 3-1. This can be done by first selecting a bin number that separates the range of frequencies every 1 Hz. Then, the profile created needs to have a bandwidth of 1 Hz. By this manipulation, this narrow bandwidth random excitation profile will simulate a sinusoidal profile. More importantly, this can be done at different frequencies when

incorporating multiaxial vibration. This excitation strategy is something that is new for any multiaxial vibration testing method. Prior attempts at generating vibration at different sinusoidal frequencies along different axes used multiple controllers. The narrow-band random control method proposed here achieves the same effect with a single controller.

Section 3.2.2 Excitation Profile Design

As discussed in Section 1.2, an important feature of designing the excitation profile is the frequency ratio of two between the transverse in plane excitation, and axial out of plane excitation. This frequency ratio can be achieved by two different strategies in the design of this experiment. The first is through the design of the dynamic features of the specimens themselves, which have been designed so that the modal frequencies of the axial and transverse modes of vibration have the frequency ratio of two. The second strategy is to provide sinusoidal excitation in the axial direction at twice the frequency of s the transverse excitation. In the second strategy, the sample will respond at a frequency ratio of two, independent of the designed modal natural frequencies of the test specimens.

Since the modal frequency ratio of two is designed in the samples themselves in the present study, this means that a broadband random excitation profile will lead to a response at only the designed modal frequencies (at a ratio of 2). As discussed in Section 3.3.1, the first excitation profile used on the samples is a broadband excitation profile for this reason. The range of frequencies used, in this case, is a range that includes only the axial and transverse in-plane modal frequencies. The amplitude is

set to be as high as the shaker can safely reach. The largest sample tested is set first and then kept consistent across all samples. Using Equation 3-4, it can be seen that the lower the excitation frequency, the higher the peak height to reach the same desired acceleration. Therefore, it can be assumed that the largest sample being shaken at the lowest frequencies will have the highest limitation on peak controlled acceleration.

Since the method of using narrow-band random vibration to generate pseudo-sinusoidal excitation is being developed in this study, an intermediate step has been used where the bandwidth is not as narrow. This intermediate step began by limiting the frequencies bins by using a narrow bandwidth random excitation profile. The resulting bandwidth for this intermediate step is 6 Hz (which included a few frequency bins). There are two main discoveries from using this narrow bandwidth which lead to the need for a better solution. The first is that the different frequency bins, being close together, interact with each other to develop beat frequencies in the response. As seen in Figure 3-4, on the left shows that although the excitation frequency is at the modal frequency, there is an envelope beating frequency. The value of this envelope frequency is equal to the bandwidth of 6 Hz. On the right, there is a Fast Fourier Transform, FFT, of the strain data results. An FFT shows the frequency information of the signal. In this case, the signal is responding significantly signal frequency. The width of this response in the FFT is equal to the bandwidth of the input vibration as well as the beat frequency of the response. The second discovery is a limitation of the controller itself. When attempting to run a biaxial 6 Hz bandwidth random profile, it is discovered that the controller is only able to control to

a single profile. A single profile is therefore created with a 6 Hz bandwidth at both the in plane and out of plane modal frequencies. There are three cases for excitation frequency: the in plane modal frequency, out of plane modal frequency, and combination of both frequencies. Similarly there are three cases for excitation direction: uniaxial in the in plane direction, uniaxial in the out of plane direction, and combination of both directions. This combination of two parameters at 3 levels each, leads to test matrix of 9 total tests.

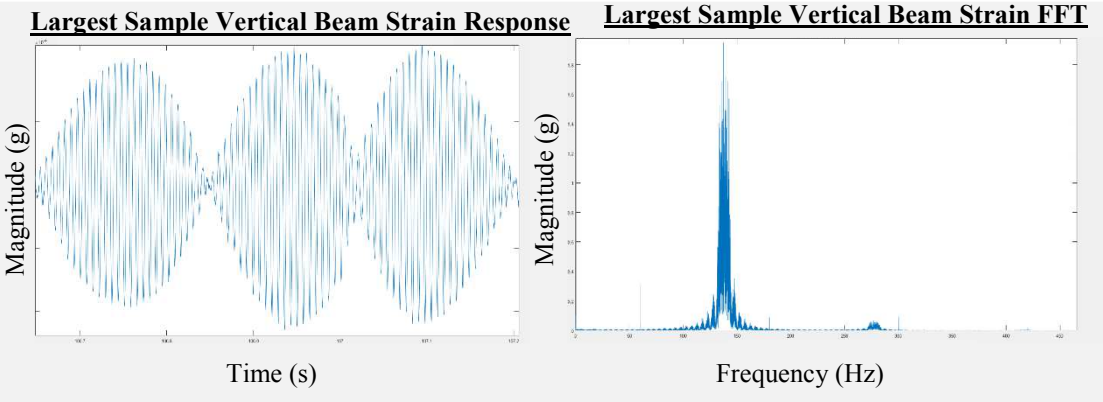

Figure 3-4: Beating from 6 Hz Bandwidth Random Excitation

[Time Response (Left), FFT (Right)]

After considerable testing, it is determined testing the sample with the 6 Hz bandwidth random excitation profile causes a considerable amount of complexity because of the beating. Therefore, the limits of the shaker are explored to establish the narrowest possible excitation bandwidth. What is discovered is, as discussed in Section 3.3.1, the control software can be manipulated to only have a single frequency bin within the random excitation profile. As seen in Figure 3-5, the FFT on the right looks qualitatively similar to that of the 6 Hz bandwidth, but has much narrower bandwidth of 1 Hz. In addition, on the left, the response shows no signs of a sinusoidal beating frequency. As discussed, this new development was instrumental

in allowing us to control the multiaxial vibration of a sample at different sinusoidal frequencies along different directions, with a single controller.

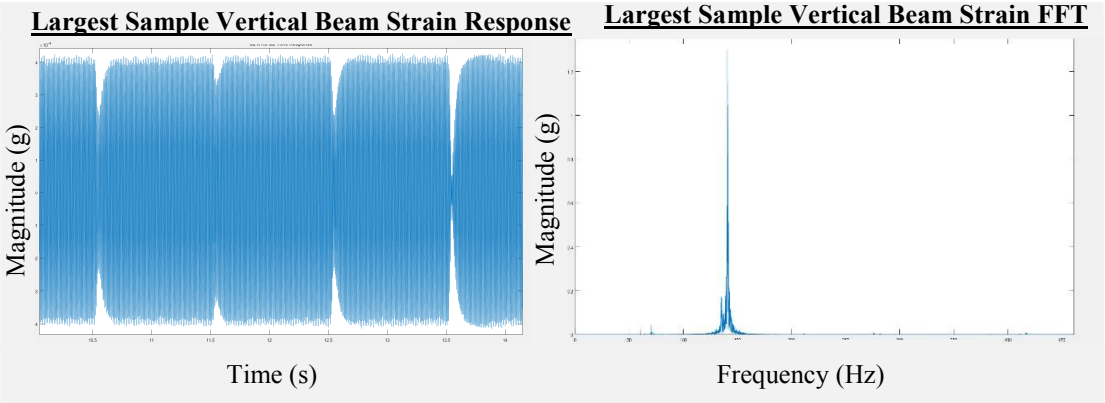

Figure 3-5: Lack of Beating from 1 Hz Bandwidth Random Excitation

[Time Response (Left), FFT (Right)]

There are some additional limitations of the controller that lead to differences in the result to a pure sinusoid. For the Signal Star software, the random excitation uses a square wave excitation in the background excitation for the random profile. As seen in the figure above, this causes a sudden beat in the data every one second and can be seen in the FFT of both the response as well as the response. This effect is clearly different from the beating response seen in Figure 3-4. A square wave will normally have Fourier frequencies at a value of F(2N-1), with an initial frequency, F, and integer, N. As N increases, the amplitude of the sinusoid decreases. This is illustrated in Figure 3-6, where on the bottom left the response becomes closer to a square wave with the addition of sinusoids, and the bottom right showing the frequencies and amplitudes that influence the creation of the square wave. In this case, the square function has an F value of 60, making the Fourier frequencies at 60, 180, 300, and 420 Hz. This is seen in the top right of Figure 3-6, which has both the

response at the modal frequencies of the sample as well as the response to the Fourier frequencies from the square wave. It is important to realize that this square function exists in all random excitation testing, not just the 1 Hz bandwidth profile. The reason that the affect from it is so evident in this case is because the random excitation profile being used eliminates the introduction of interference from all other frequencies, leaving the excitation frequency and the square function.

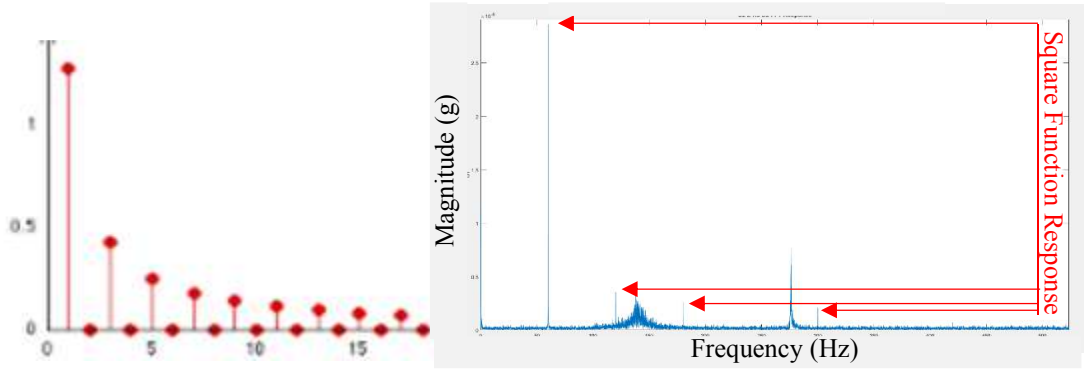

Figure 3-6: Square Function FFT

[Actual Square Wave FFT (Left), Experimental FFT (Right)]

Summarizing this section, there are three testing methods tested on the specimens that are fabricated. The first is a broadband random excitation test that verifies that the specimen responds at the design frequencies, as well as averages out all phases of excitation to give an average nonlinear amplification of the sample. The second is a narrow random excitation profile with a bandwidth of 6 Hz, which limits the amount of frequency bins in the excitation. This testing will single out the excitation to the frequency ratio wanted, but will not average the phases of the excitation. Finally, the final test is a sinusoidal excitation using random excitation profiles. The bandwidth of this profile is 1 Hz and includes a single frequency bin.

This testing method eliminates the limitations from the narrow bandwidth random excitation profile. The software process for the 1 Hz bandwidth test is explained in Appendix G.

Section 3.3 Instrumentation

In the previous sections, the experimental setup, and how it would be controlled is discussed. The next thing to understand is what should be observed from this testing. Reiterating from the earlier sections, the goal of this experiment is to observe the linear and nonlinear responses based on multiaxial vibration. For this to be possible, the double beam needs to be instrumented properly to gather data on its response to vibration.

This instrumentation will use two different technologies. The first is accelerometers, which will give the information on the motion of the sample under vibration. There will be three accelerometers used: one triaxial accelerometer, and two uniaxial accelerometers. The purpose of using three accelerometers is to ensure that the data being collected has not been corrupted by false readings. In addition, the accelerometers will be used as the point mass of the double beam setup. The triaxial accelerometer is a weight of 2.5 gram and the uniaxial accelerometers are .6 grams each. This adds to a total of 3.7 grams which is used for the design modeling of the samples and is used in the post-processed model of the system. These accelerometers are sampled directly from the post-processing of the Signal Star software. There are two types of measurements made from Signal Star for the accelerometers. The first is time history data which is exported during the test and is taken at sampling frequency of 1024 Hz. The software dumps data as it takes additional data, so only 1024

measurements are given per data export. This time history of the acceleration from the table accelerometers and response will be used in the post-processed model of the system. The limitations on the sampling frequency limit the effectiveness of the post-processed model. The second type of measurements is the FFT of the acceleration data. Signal Star uses its own averaging and windowing, which will be discussed further in the analysis. The best resolution of the FFT can be measured by taking samples of the accelerometer FFT from Signal Star, since it includes significantly more data than can be retrieved from time history collection. The FFTs will be used during the analysis of the system in Chapter 4.

The second technology used is the strain gauges. Strain gauges measure the actual deformation of the setup. In this circumstance, the deformation of interest is the second beam representing the component. The data from the strain gauges is taken on a separate data acquisition system. This data acquisition system samples the deformation from the strain gauge at a sampling frequency of 5000 Hz. The data collected from each test is the complete time history of the measurements, unlike the accelerometers which only allows for a snapshot of the time history to be extracted. The data collected from the strain gauges will be post-processed to analyze the system and confirm the conclusions drawn from the accelerometer data.

In summary, three accelerometers and one strain gauge is mounted on each sample. The accelerometers' time history snapshot and FFT will be sampled directly from the Signal Star software, while the strain gauges' complete time history will be taken from a separate data acquisition system.

Section 3.4 Test Matrix

The question this section aims to answer is what experiment plan should be use for the experiment setup created. As discussed in Section 3.2, there are three testing methods being used in this experiment. A broadband random excitation with a range including both of the modal frequencies, a narrow bandwidth random excitation profile that include modal frequencies in its bandwidth, and a sinusoidal excitation using random excitation profiles at the modal frequencies. In all of these testing methods, the actual experimental modal frequencies are needed. As discussed in the design modeling, there is an expected three modes of vibration within the range of the multiaxial shaker. For an accurate measurement of these modes, the first test to be run will be a sinusoidal sweep in each translational degree of freedom of interest. In other words, the shaker table will vibrate in a sinusoidal profile in a specific direction at a frequency that will increase over time. When the profile reaches the natural frequency of the double beam setup, the response of the triaxial accelerometer should hit a peak. This sweep test will be done in the X and Z-Axis, respectively, to determine each of the two modes of vibration frequency that will be used in the rest of the tests. The reason for this is that shaking in the direction of the specific mode shape will provide the highest response.

	Sine Sweep Test	
	X-Axis	**Z-Axis**
X-Axis Test	X	
Z-Axis Test		X

Table 3-1: Sine Sweep Test Matrix

With each of the three excitation testing method comes different test matrices. The broadband random excitation will have a single profile being run, which is a single amplitude being excited at all frequencies in a range of frequencies that include both the modal frequencies of the in plane transverse deformation as well as the axial out of plane deformation. This single profile will be run in the X-Axis, Z-Axis, and then a combined X and Z-Axis.

	Broadband	
	X-Axis	**Z-Axis**
X-Axis Test	X	
Z-Axis Test		X
Biaxial Test	X	X

Table 3-2: Broadband Test Matrix

As discussed in the Section 3.2.2, the 6 Hz bandwidth random excitation is discussed to have the problem of being the most complex test matrix. The reason for this is that the controller will not allow a two separate 6 Hz bandwidth profiles in different directions. For this reason, this excitation testing method requires three different profiles. The first will have the 6 Hz bandwidth at the in plane transverse modal frequency. The second will have a 6 Hz bandwidth at the out of plane axial modal frequency. The third will be a bimodal profile with a 6 Hz bandwidth at both of the modal frequencies of interest. Each of the three profiles will need to be testing in the X-Axis, Z-Axis, and a combination of both the X and Z-Axis. This give a total of 9 test for the excitation strategy of the 6 Hz bandwidth.

	6 Hz Bandwidth	
	X-Axis	**Z-Axis**
X-Axis Test 1	Mode 2	
X-Axis Test 2	Mode 3	
X-Axis Test 3	Mode 2 and 3	

Z-Axis Test 1		Mode 2
Z-Axis Test 2		Mode 3
Z-Axis Test 3		Mode 2 and 3
Biaxial Test 1	Mode 2	Mode 2
Biaxial Test 2	Mode 3	Mode 3
Biaxial Test 3	Mode 2 and 3	Mode 2 and 3

Table 3-3: 6 Hz Bandwidth Test Matrix

The last testing method is the sinusoidal excitation based on a 1 Hz bandwidth random profile. This testing method will have a simplified testing strategy to that of the 6 Hz bandwidth. This testing method is simplified, because the controller allows two separate 1 Hz bandwidth random profiles in different directions. The excitation strategy requires a total of two profiles; a 1 Hz bandwidth profile at the respective modal frequencies. This requires a total of 3 tests. A test of the excitation profile at the transverse modal frequency in the transverse direction, a test of the excitation profile at the axial modal frequency in the axial direction, and then a combination of the two profile in their respective directions.

	1 Hz Bandwidth	
	X-Axis	**Z-Axis**
X-Axis Test	Mode 2	
Z-Axis Test		Mode 3
Biaxial Test	Mode 2	Mode 3

Table 3-4: 1 Hz Bandwidth Test Matrix

In summary, the experiment setup will include three levels of vibration. This experimental setup will be tested through a Sine Sweep to discover the modal frequencies. Next, these frequencies will be used in three different test matrices based on the three test methods to take measurements from the instrumentation on the samples.

Chapter 4: Experiment

Section 4.1 Introduction

This chapter will first deliver the results from the experimental parametric study for the three multiaxial testing methods. The order of the results presented will be in the order of the test matrix described in Section 3.4, starting with the Sweep Test, and then proceeding to the multiaxial testing under broadband random excitation profiles, narrow bandwidth random excitation profiles, and sinusoidal excitation by random excitation profiles.

Then, this chapter will analyze the results and relate the results to one another to form a meaningful conclusion about the effect of size and mass on linearity. The FFTs of each testing method will be compared to each other by a global normalized difference. These normalized differences will be compared across the different samples to develop trends.

Section 4.2 Sweep Test

As discussed in the previous section, the first set of tests that are done are the sinusoidal sweep test to discover the actual frequencies for the experimental specimens. In this test, the shaker will vibrate the table at a sinusoidal frequency that increases over time. The data shown from the sweep testing is taken directly from the Signal Star software. Signal Star takes an FFT of the time history at each frequency step based on the sweep rate of the test. Each measurement is made at the frequency of excitation and fit to the curves seen in the Figure 4-1. The peaks of these figures are selected as the modal frequencies of the sample. Table 4-1 shows the result of

each of the peak measurements made and how they compare to the design modeling modal frequencies. The frequencies match closely to the predicted frequencies with an increasing error as the sample becomes smaller. This error is most likely the caused by any additional mass introduced to the system, because as there is less mass in the system, the error is greater. This mass could be a result of the wire mass of the sensors used and from the epoxy used to constrain the sensors.

	Setup 1		Setup 2		Setup 3	
	Model	Experimental	Model	Experimental	Model	Experimental
Mode 2	143.9	141	207.7	195	308.7	280
Mode 3	283.9	282	408.8	383	623.8	543
Ratio	1.973	2	1.968	1.964	2.021	1.939

	Setup 4		Setup 5	
	Model	Experimental	Model	Experimental
Mode 2	513	478	884.1	955
Mode 3	1075.5	929	1777.3	1914
Ratio	2.096	1.944	2.01	2.004

Table 4-1: Sweep Test Result

The figure below shows the result from the Sine Sweep test of Sample 1. Figure 4-1 illustrates the two main results seen from the Sine Sweep Test. The first is the specific modal frequencies of the sample at 141 and 282 Hz respectively. Since these modal frequencies shown by the peaks in Figure 4-1 have a frequency ratio of 2 as shown in Table 4-1, the frequencies can be used for the excitation profiles in the subsequent tests. The second result from the Sine Sweep test is that given the same excitation, the out of plane modal frequency of the axial motion of Beam 1, shown on the right in Figure 4-1, has an amplitude that is higher than the transverse modal frequency by a factor of two. This is consistent across all samples tested by the Sine

Sweep test. The rest on the resulting graphs for the other samples from the Sine Sweep test are included in Appendix B.

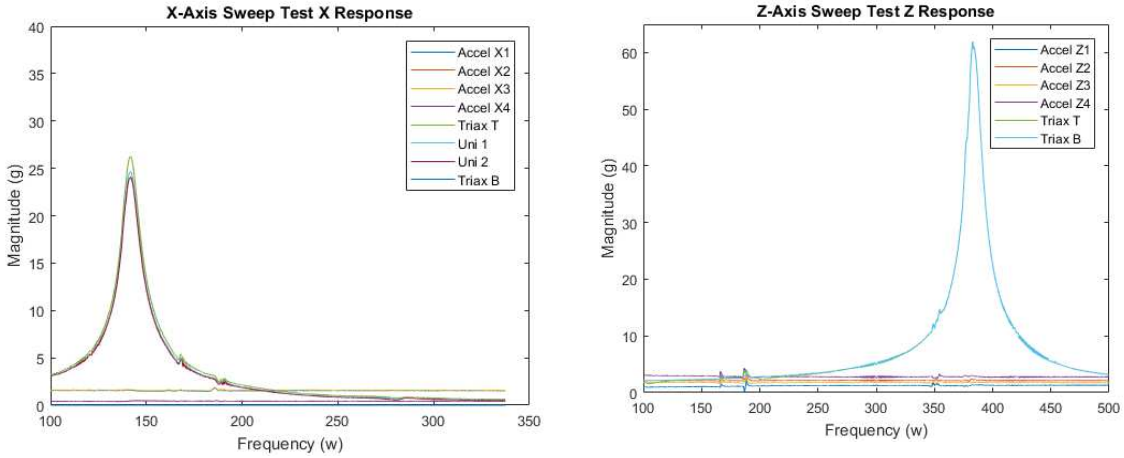

Figure 4-1: Sweep Test FFT Result

Section 4.3 Broadband Testing

Section 4.3.1 Broadband Experimental Result

After the specific modal frequencies have been identified, the testing method began for the samples. The first testing method is to use a broadband random profile to test the samples. This testing method, as discussed in Chapter 3, includes a broadband random excitation profile that vibrates the table at a range of frequencies that include the two modal frequencies found in Section 4.1. The resulting table acceleration from this type of excitation profile is shown by the time history in Figure 4-2 below. There are some sudden changes, but overall the profile is shaken at a variable frequency and phase. Since the profile varies in this way, the response will

be independent of the phase of the modal frequencies. The response can be thought of as an average of a phases excited by the random profile.

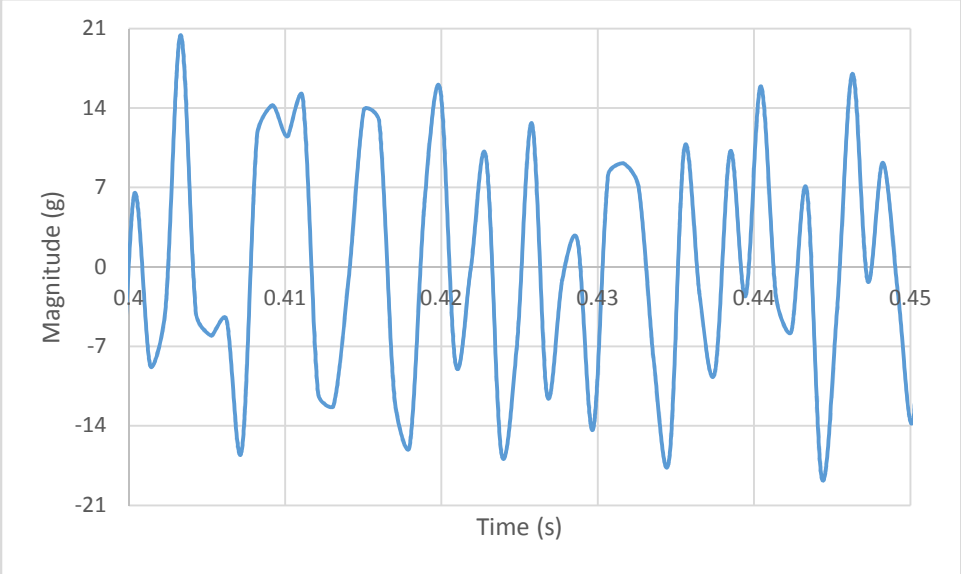

Figure 4-2: Random Excitation Time History

As discussed in Chapter 2, the goal is for these results to be repeatable, and reliable. The broadband random excitation testing matrix is performed on samples 4, and 5. Each testing case seen in the test matrix is ran with three replicates. The acceleration FFT data is taken directly from the Signal Star software from these replicates and averaged together to form a signal acceleration averaged result for each testing case. The FFT on the Signal Star software takes averages of data to smooth the FFT and give it an FFT resolution of 1 Hz. The following figures show the data from this averaging of data of each testing case. The data from the original three replicates are shown in the Appendix C.

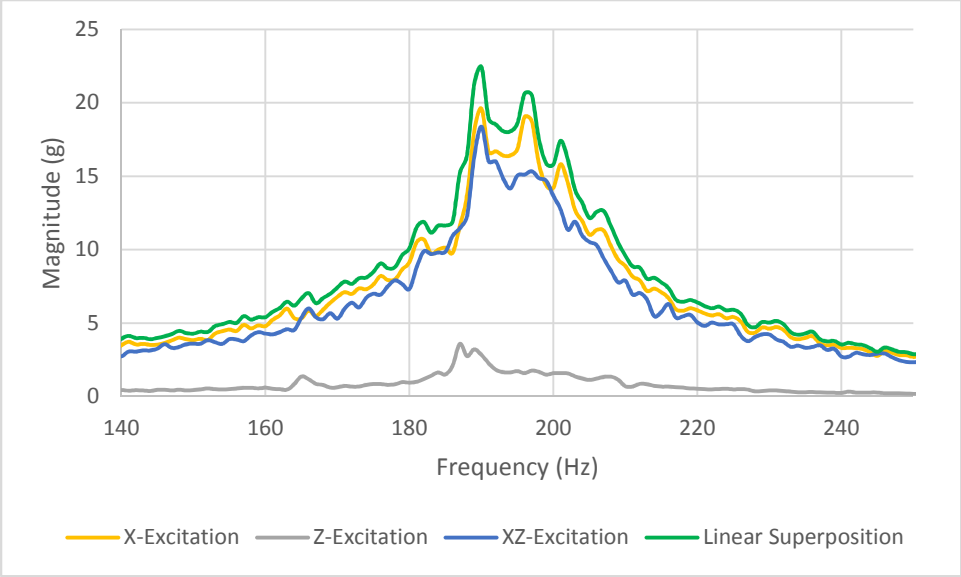

Figure 4-3: Sample 4 Broadband Excitation Averaged Acceleration Result

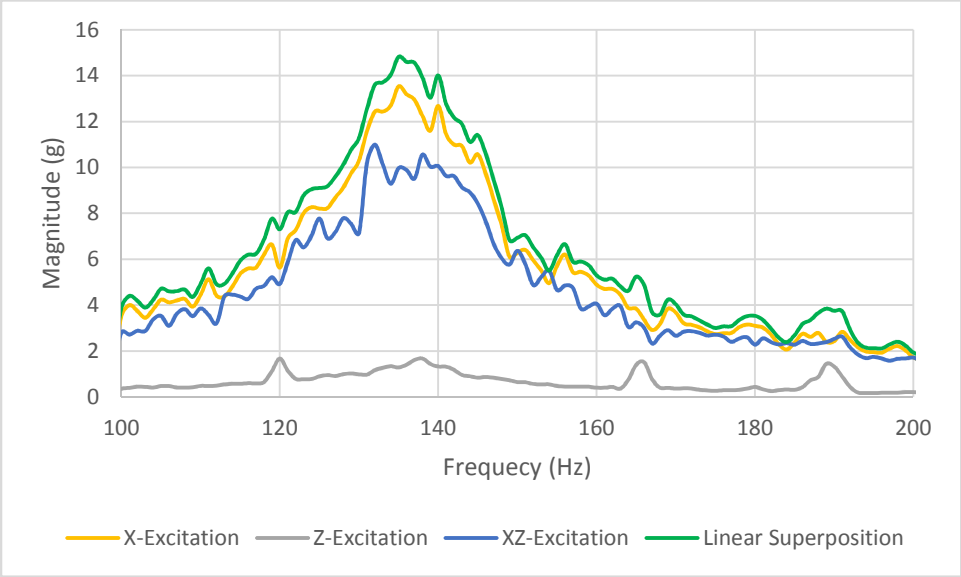

Figure 4-4: Sample 5 Broadband Excitation Averaged Acceleration Result

The figures above include the testing from Samples 4, and 5. As labelled in the titles, there graphs show the results as measured from the X-Axis of the triaxial tip accelerometer. There are four lines in each graph. The yellow line shows the results from the broadband excitation in the X-Axis. The gray line shows the results from the broadband excitation in the Z-Axis. The green line shows the addition of the yellow

and gray line. The blue line shows the actual result from a broadband excitation in the X-Axis and the Z-Axis.

The second type of data collected is strain gauge data. The strain gauges measure the deflection of the beams. Unlike the Signal Star data that is averaged over a certain amount of time of each run, the data collected is the raw deflection over the course of a 20 to 30 second test at a sampling frequency of 5000 Hz. With around 150,000 data points per replicate, the data is first trimmed from the beginning ramp up and the back end ramp down at the end of the test. This leaves around 90,000 data points per replicate, where the sample is directly responding to the broadband random excitation profile. The first thing that is done is to first take an average of the three trimmed replicates, and then take an FFT of the trimmed average data. Similar to the post-processed Signal Star FFT, the strain gauge FFT data is sent through a Hanning Windowing Function to smooth the results. This FFT, seen below, has a resolution of .1 Hz. Since the FFT still needed a significant amount of smoothing to see the underlying curve, three other resolutions are used. The original 90,000 data points is split into different sized chunks of data, and these chunks are average them into a single signal per replicate. These data chunks overlapped each other with around 50% for robustness of averaging. These averaged replicates are then averaged together into a single signal per test. The three resolutions are .25 Hz with ten data chunks of 20,000 data points, .5 Hz with sixteen data chunks of 10,000 data points, and 1 Hz with 34 data chunks of 5,000 data points. The results of this method are shown for Sample 4 and 5 below. In addition, Matlab code excerpts are included and explained in Appendix F.

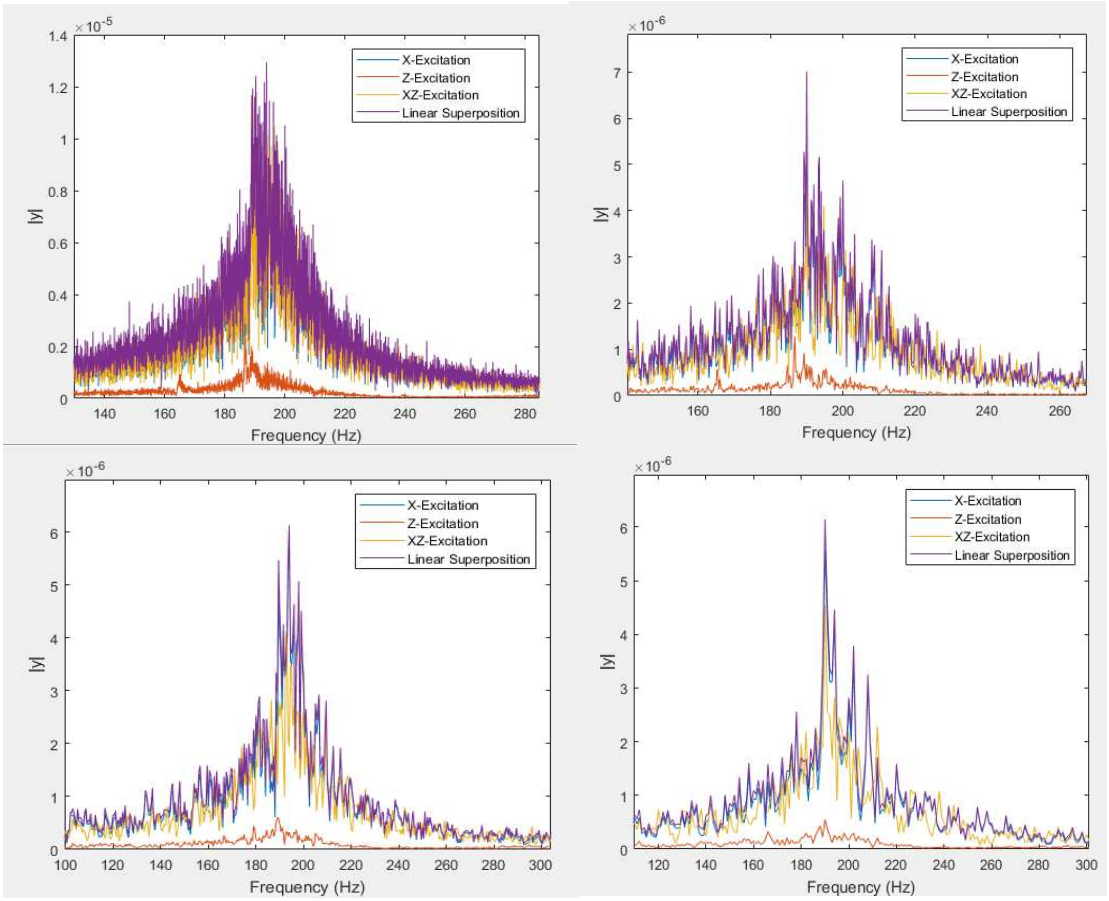

Figure 4-5: Sample 4 Strain Gauge FFT

(Top Left .1 Hz Resolution, Top Right .25 Hz Resolution. Bottom Left .5 Hz Resolution, Bottom Right 1 Hz Resolution)

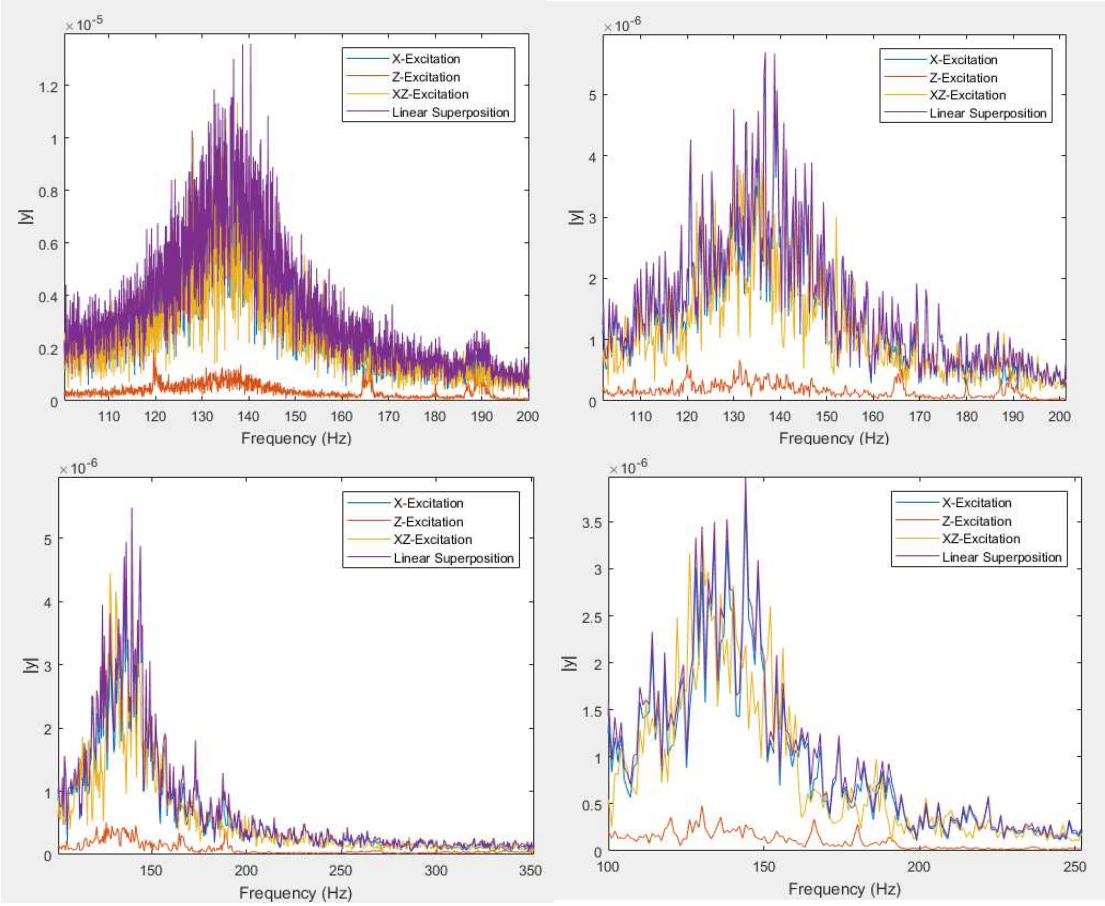

Figure 4-6: Sample 5 Strain Gauge FFT

(Top Left .1 Hz Resolution, Top Right .25 Hz Resolution. Bottom Left .5 Hz Resolution, Bottom Right 1 Hz Resolution)

Section 4.3.2: Broadband Experimental Analysis

The testing matrix included a broadband random excitation in the X-Axis, a broadband random excitation in the Z-Axis, and a combined biaxial broadband excitation in both the X and Z-Axis. In the resulting graphs in Section 4.2.1, the linear superposition of the uniaxial excitation in the X-Axis and the Z-Axis. The Normalized difference for the broadband random excitation profile, as shown in Equation 4-1, is the normalized difference between the linear superposition with the actual biaxial response with respect to the peak value of the linear superposition.

$$Normalized\ Difference = \frac{R_{XZ} - (R_X + R_Z)}{Max((R_X + R_Z))} \qquad \text{Equation 4-1}$$

Equation 4-1 is used to form a global Normalized difference of the resulting graphs of both the accelerometers and strain gauges shown in the figures of Section 4.2.1. Beginning the analysis with the accelerometer data, the figures below show the global normalized difference of the accelerometer FFTs from Figures 4-3, and Figure 4-4.

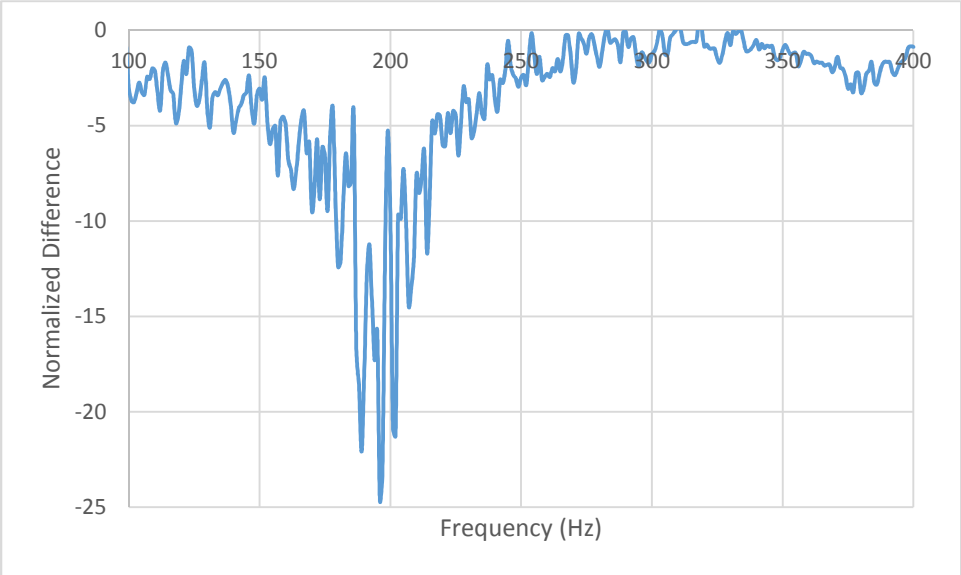

Figure 4-7: Sample 4 Broadband Acceleration FFT Normalized difference

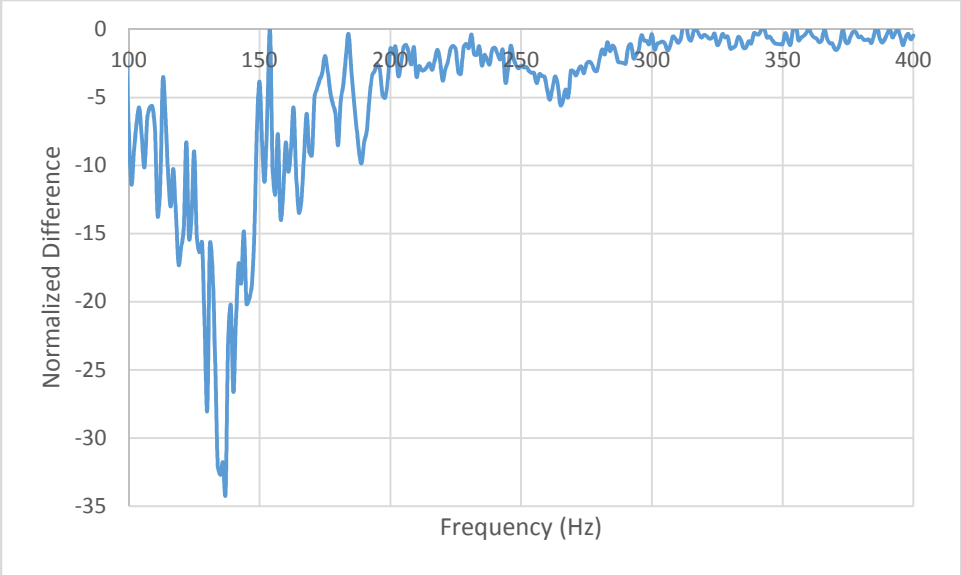

Figure 4-8: Sample 5 Broadband Acceleration FFT Normalized Difference

The shape of both of the figures above are the same with a single negative peak. This negative peak is illustrating the nonlinear amplification caused by multiaxial vibration. There are two noticeable differences between these two figures. The first is that the peaks are at different frequencies. This is to be expected, as Sample 4 responds to a modal frequency of 195 Hz, while Sampe 5 responds to a modal frequency of 140 Hz. The second difference is a the clear decrease in amplitude for the accelerometer amplitude from the smaller Sample 4 to the large Sample 5. Sample 5 has an amplitude of -34%, while Sample 4 has an amplitude of -24.6%. This decrease in amplitude is the first relation between paremetric differences in height and mass. Sinece Sample 5 is the tallest, heaviest sample, this is the first evidence that a decrease in height and mass will decrease the amplification factor of nonlinear effects.

The second type of data collected is strain gauge data. As discussed in section 4.2, the strain gauge data is windowed with a Hanning Function, and a FFT is taken at several resolutions. One main thing to notice about the different resolutions is that the frequency information of the FFTs did not change, while the amplitude information did changed significantly. This is plotted in the Figure 4-9 below. The figure shows that for both samples, the amplitudes decrease as the FFT has a coarser resolution. The question comes to mind is which amplitude is the most accurate representation of the data set. This question becomes completely subjective, which is not something a clear conclusion can be built on. Therefore, similar to the accelerometer data, it is important to use the entire data set when calculating the nonlinear effect each sample experiences.

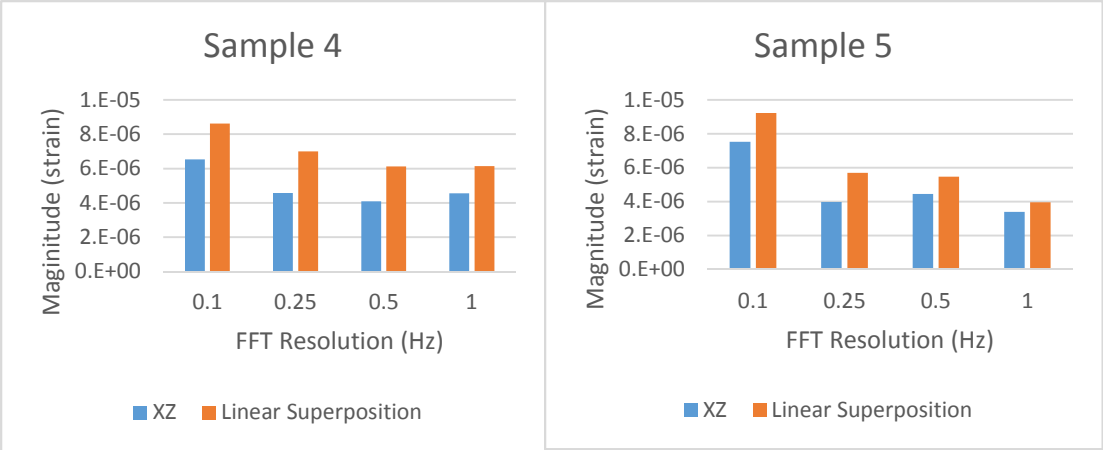

Figure 4-9: Broadband Random Excitation Strain Gauge Peaks based on FFT Resolution

Below shows a side by side view of the global normalized difference as calculated from the strain gauge FFT for Sample 4 and 5 for the respective FFT resolution. The first thing to realize is that the loss of information discussed in Figure

4-9 becomes more clear in these figures, as both the smoothness of the enveloped shape as well as the amplitudes change drastically as the FFT resolution becomes looser. This does not mean that clear conclussions can still be drawn from the global normalized difference graphs. This is because although the amplitude information changes, there are trends between the samples that are consistent across all resolutions. The first is that there is both a positive and negative amplitude at the modal frequency. It is clear that the peaks are at the modal frequencies, because at a fine resolution the two peaks are within .5 Hz from one another. A possible reason for both of these peaks comes from the broadband random excitation profile itself. The broadband random excitation profile changes the phase of the frequency being excited. From Figure 1-5, it is shown that phase is one of the main contributors to nonlinear effects, and that depending on the phase, the sample can either be in the constructive or deconstructive region. In this case, the broadband excitation shows the full range of the response to a certain excitation frequency.

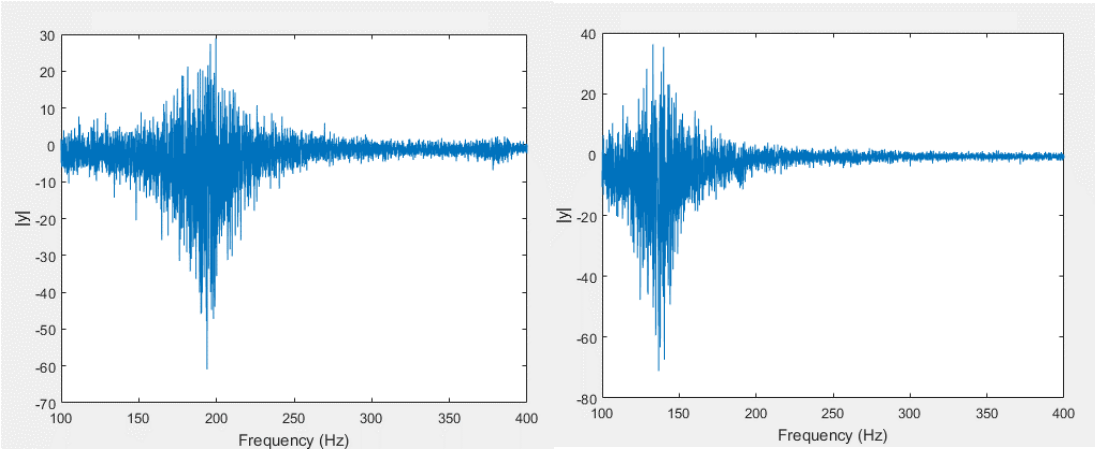

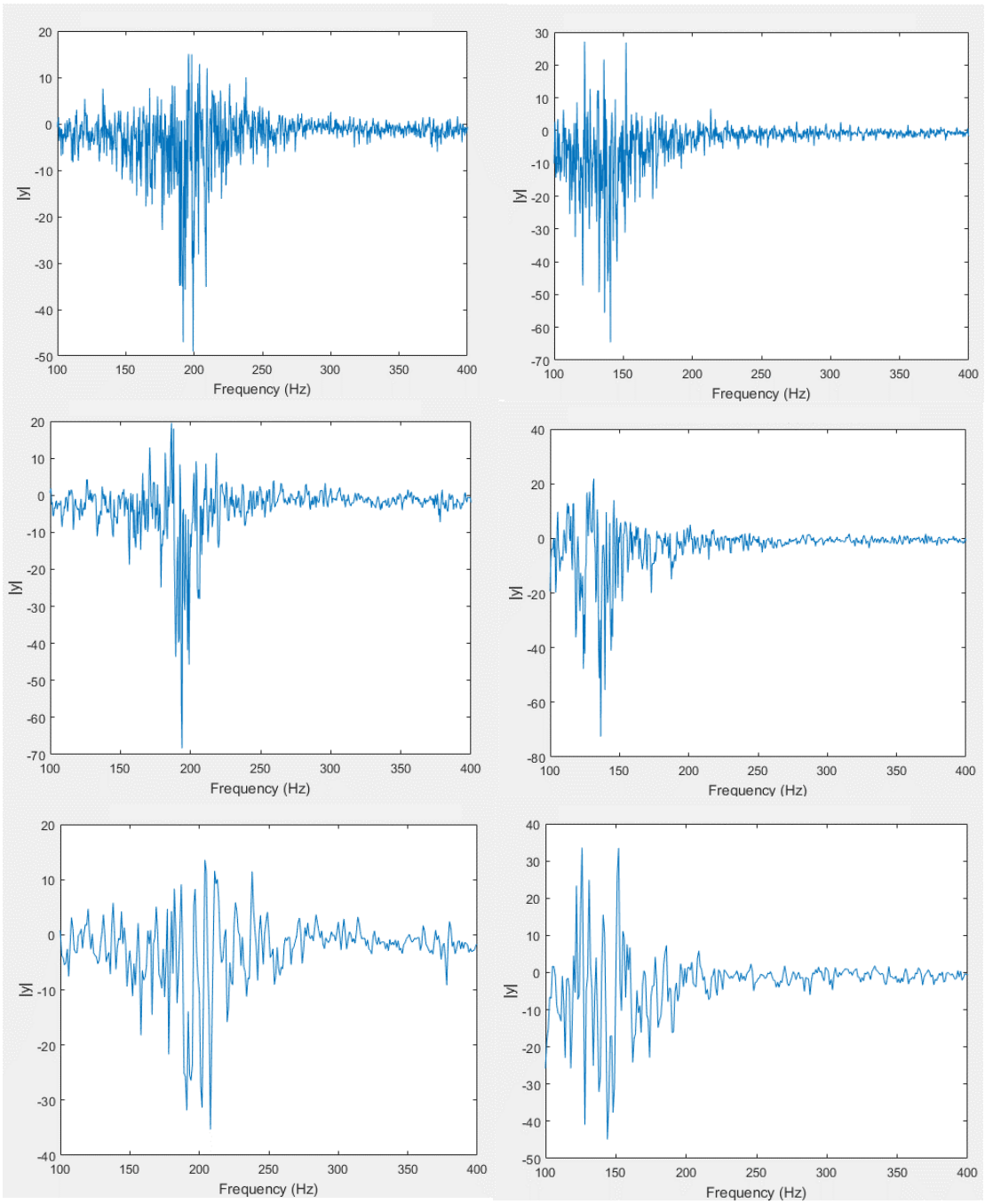

Figure 4-10: Strain Gauge Peaks Normalized difference based on FFT Resolution

[Sample 5 (Left Column), Sample 4 (Right Column)]

[.1 Hz Resolution (1st Row), .25 Hz Resolution (2nd Row), .5 Hz Resolution (3rd Row), 1 Hz Resolution (4th Row)]

The second conclusion that can be drawn from the strain gauge data is the same conclussion that the accelerometer data gives evidence for. No matter which resolution of the global normalized difference, the positive and negative peak values decrease from Sample 5 to sample 4. This is illustrated below in Figure 4-11. Each line from the figure below projects a convergence to fitting a linear model as the sample becomes smaller. This conclussion matches the conclussion drawn from the acceleration data that leads projects that a decrease in mass and height will decrease the nonlinear amplification factor.

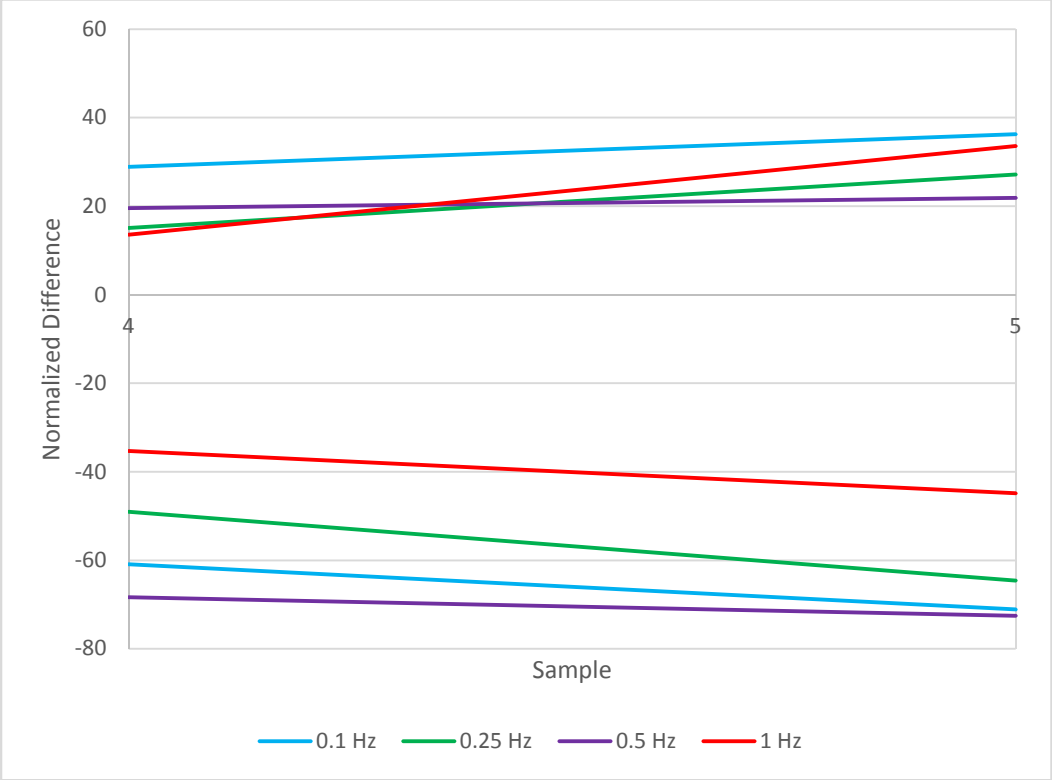

Figure 4-11: Broadband Strain FFT Normalized difference peaks for Tested Samples

Section 4.4 6 Hz Narrow Bandwidth Testing

Section 4.4.1 6 Hz Bandwidth Experimental Results

As discussed in Chapter 3, the test matrix for the 6 Hz narrow bandwidth has the most profiles and testing. Unlike the broadband testing from the previous section, the 6 Hz narrow bandwidth limits the amount of frequency bins that are excited in the random excitation profile. In this case, the profile will ramp up from 6 to 3 Hz more or less than the modal frequencies discovered in Section 4.1. Then from 3 Hz to 0 Hz more or less than the modal frequencies, there will be a constant amount of energy given. This profile allows for a near sinusoidal excitation with beat frequencies from interference from the other close frequencies within the narrow bandwidth. Unlike the broadband excitation, the narrow bandwidth can be effected by the phase of the Sinusoidal excitation. Since the phase cannot be controlled, the settings allowed the test to change the phase over time. This should give a similar result to the broadband excitation.

Similar to the broadband excitation, there acceleration data taken with three replicates for each of the nine tests in the test matrix. The tests include a uniaxial test of all three profiles in the X-Axis, Z-Axis, and then in both axis. The three profiles include a 6 Hz bandwidth at the axial modal frequency, the transverse modal frequency, and then a bimodal profile at both frequencies. With these nine tests, the linear superposition of the biaxial excitation at both frequencies can be estimated in three ways. The first is by adding all the four uniaxial tests at a single modal frequency. The second is by adding the two uniaxial test at the bimodal profile. The third is by adding the two biaxial test at a single modal frequency.

$$R_{XZ(f_1,f_2)} = R_{X(f_1)} + R_{Z(f_1)} + R_{X(f_2)} + R_{Z(f_2)} \quad \text{Equation 4-2}$$

$$R_{XZ(f_1,f_2)} = R_{X(f_1,f_2)} + R_{Z(f_1,f_2)} \quad \text{Equation 4-3}$$

$$R_{XZ(f_1,f_2)} = R_{XZ(f_1)} + R_{XZ(f_2)} \quad \text{Equation 4-4}$$

Summarizing once more with the equations above, the first estimation adds the response to X-Excitation at the transverse modal frequency, f_1, Z-Excitation at f_1, X-Excitation at the axial modal frequency, f_2, and Z-Excitation at f_2. The second method adds the response of X-Excitation at f_1 and f_2 to Z-Excitation at f_1 and f_2. The third method adds the response of XZ-Excitation at f_1 to XZ-Excitation at f_2.

Similar to the broadband excitation, there are three replicates for each of the nine testing conditions in the test matrix. These replicates were averaged together to form a single signal. The results from the averaging are shown below in Figure 4-12 for Sample 2. The results from the other samples can be seen in Appendix D.

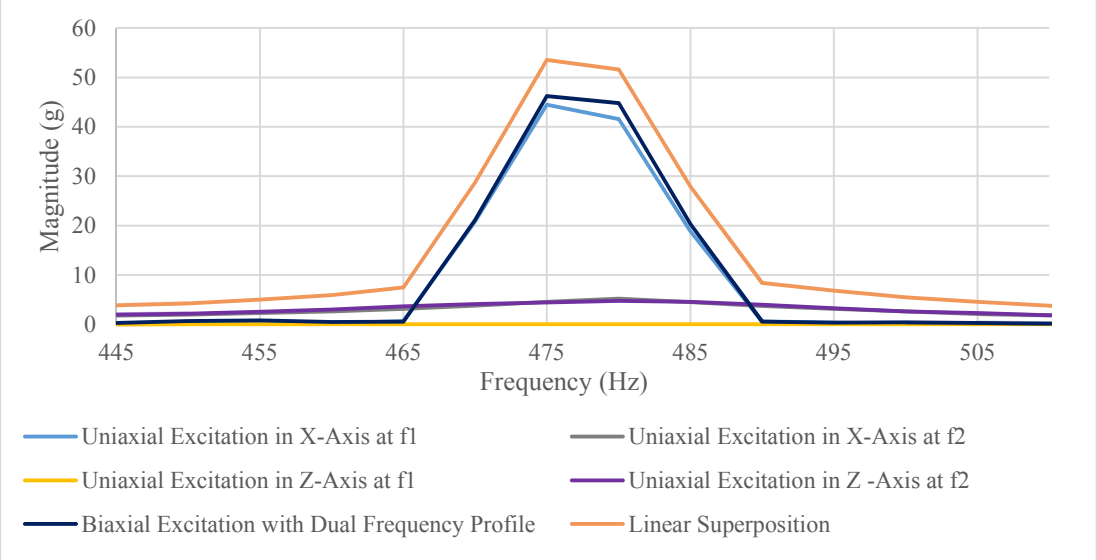

Figure 4-12: Sample 2 6 Hz Bandwidth Acceleration Response Linear Superposition Estimation 1

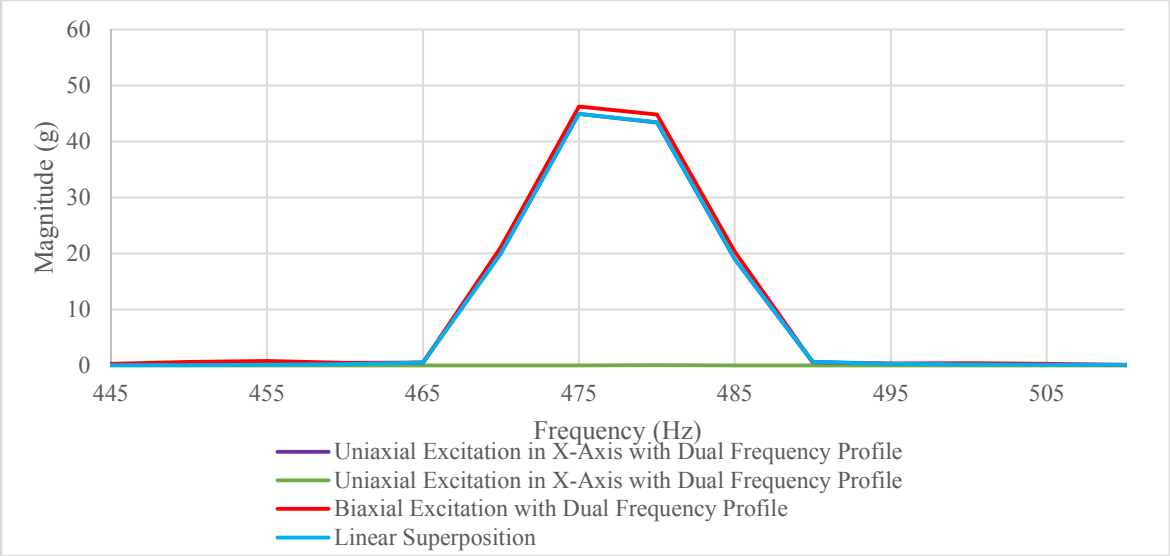

Figure 4-13: Sample 2 6 Hz Bandwidth Acceleration Response Linear Superposition Estimation 2

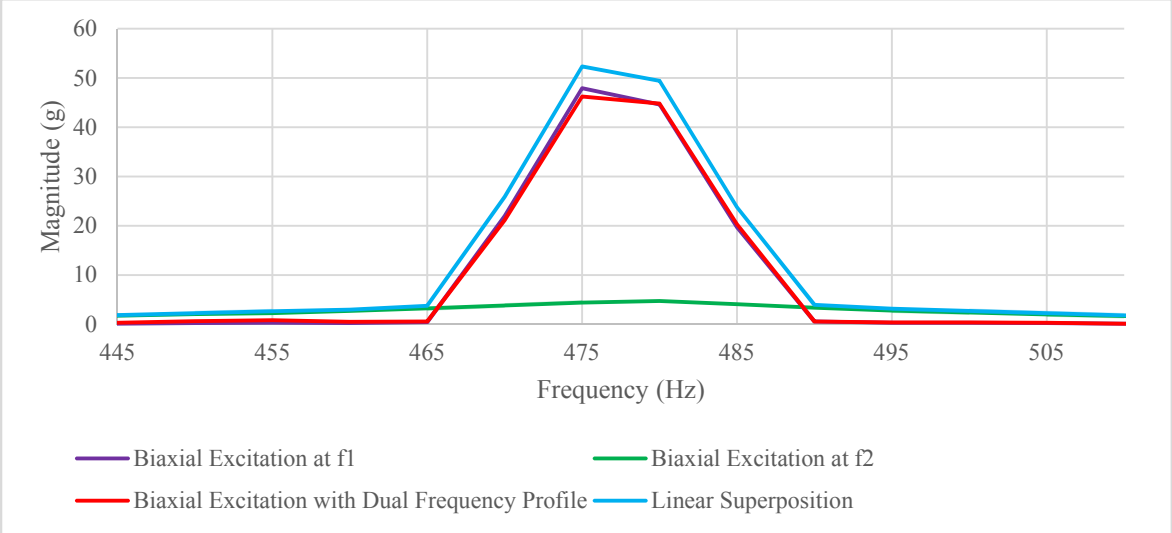

Figure 4-14: Sample 2 6 Hz Bandwidth Acceleration Response Linear Superposition Estimation 3

There are three figures for each sample. Each of these figures show the results of the 6 Hz bandwidth random excitation acceleration results based on the three linear superposition estimation methods seen in Equations 4-2, 4-3, and 4-4. The first estimation method shows the superposition of all of the uniaxial tests in a single axis.

The second estimation with the superposition of all of the biaxial excitation testing. The third estimation with the superposition of all of the dual frequency profiles.

Section 4.4.2: 6 Hz Bandwidth Analysis

Similar to the broadband random excitation profile, the narrow bandwidth random excitation profile acceleration data will go through the same post-processing. First, all of the averaged FFTs are used to create three estimations of the global Normalized difference per sample. Figure 4-13 shows the result from the global Normalized difference of the graphs from Figure 12. The rest of the sample global Normalized differences are shown in Appendix E.

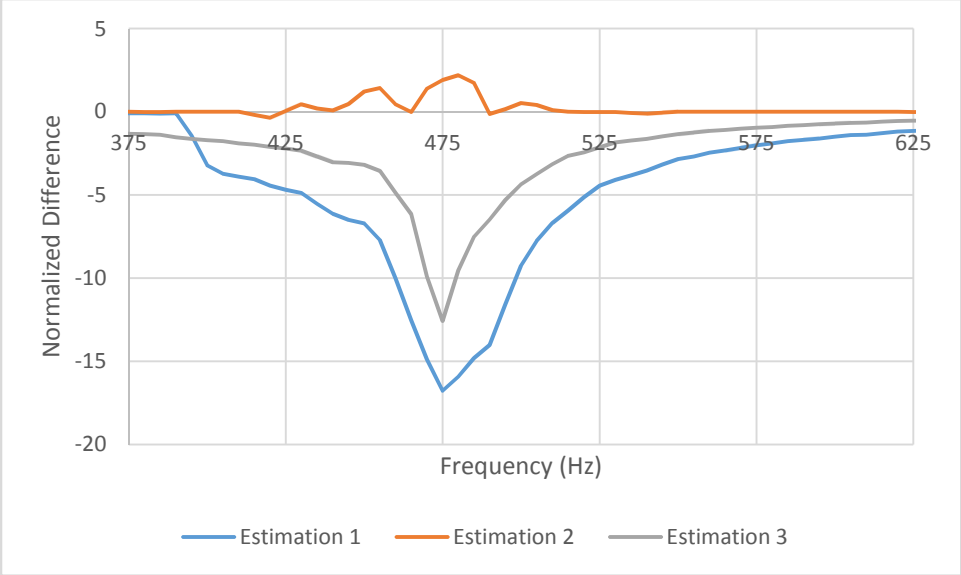

Figure 4-15: Sample 2 6 Hz Bandwidth Acceleration Global Normalized difference

As Figure 12 shows, depending on the estimation method, the resulting global Normalized difference graph. Although this is true, each estimation method has the exact same frequency where it reaches its peak. The information that changes drastically is the amplitude information. This is seen by estimation methods 1 and 3 only have a negative peak, while estimation 2 only has a positive peak. When the

peaks of each estimation method are taken for each sample, the result is Figure 4-13. Unlike the broadband trends between parametric data, the data in this figure does not lead to meaningful conclusions about the nonlinearity of parametrically changing mass and height. One reason for this result is the fact that this testing method is the most complex out of the three used, meaning that it is possible that underlying factors are effecting the result.

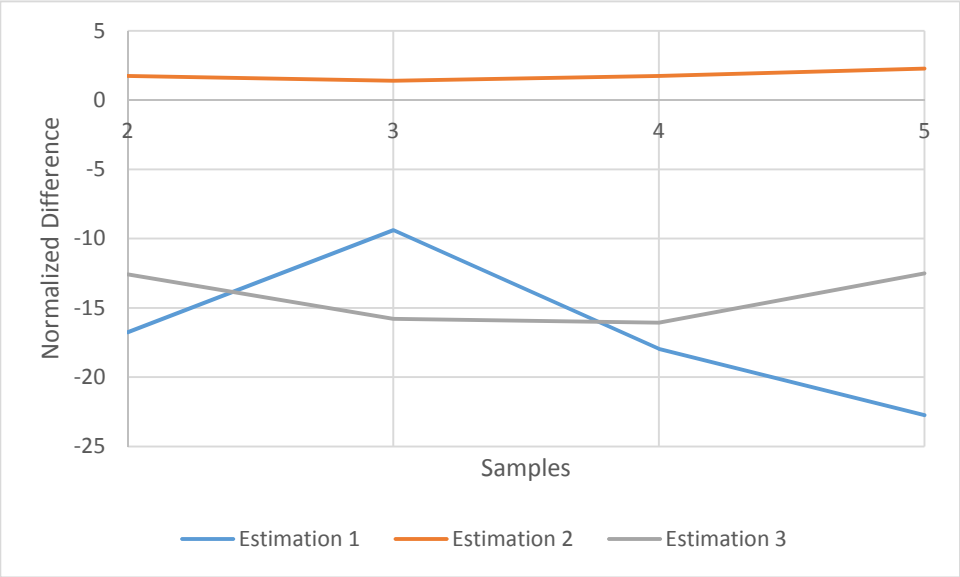

Figure 4-16: 6 Hz Bandwidth Strain FFT Normalized difference of Estimation Methods for Tested Samples

The other possible reason for the complexity in the result is the phase, as alluded to earlier. Unlike the broadband random excitation, the phase of the excitation profile is not changing as rapidly. Therefore, the result may show a response to any range large or small of phased excitations. If this assumption is made, then it can be assumed that the resulting estimation of the global Normalized difference will have a range of positive and negative peaks depending on the phase of the data measured. This is what is seen in all of the resulting global Normalized difference estimations,

with ranges of positive and negative peaks, depending on the estimation method. Therefore, one way to view the parametric end result is not the individual peaks of each estimation method, but the max positive and negative peaks from all three estimation methods. This is seen in Figure 4-14 below. The result is not perfect, but shows a more useful result that matches that of the broadband conclusion. If the assumptions presented here are true, then there is some uncertainty in Figure 4-14 for the phases that were not seen in the narrow bandwidth random excitation profile testing. Further testing and uncertainty aside, there is a reasonable amount of evidence to conclude that the narrow bandwidth random excitation profile testing shows a similar result to the broadband random excitation test.

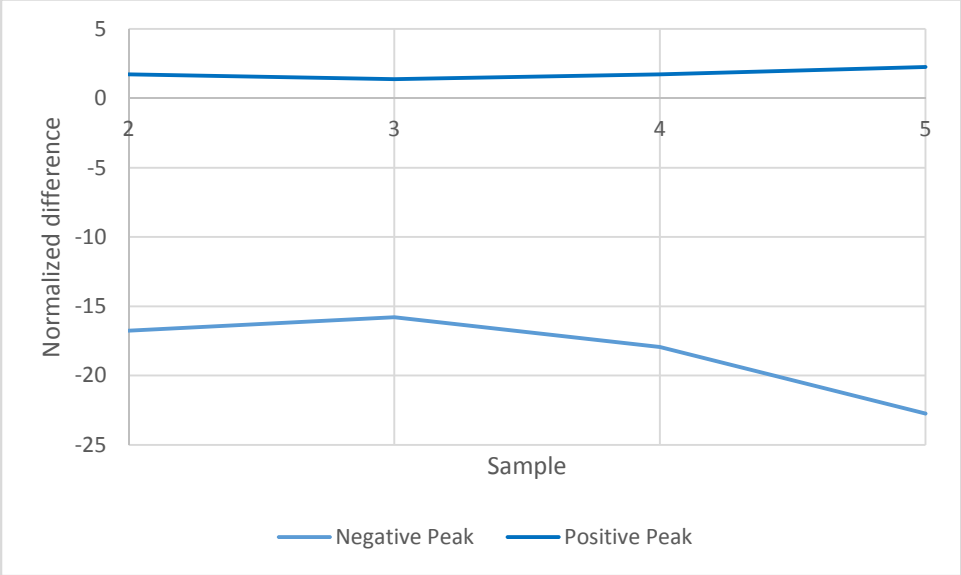

Figure 4-17: 6 Hz Bandwidth Strain FFT Normalized difference peaks for Tested Samples

Section 4.5: 1 Hz Narrow Bandwidth Testing

Section 4.5.1: 1 Hz Bandwidth Experimental Results

Similar to the broadband random excitation test, this section will present the accelerometer and strain gauge data from the experimenting. The test matrix used for this section is the 1 Hz bandwidth random excitation testing. As shown in Section 3.2.2, the excitation profile used in this section is a sinusoidal excitation using random excitation control. This simplifies the complexities from the narrow bandwidth random excitation profile.

The first set of data is from the tip accelerometer. For this test matrix, there are three total tests. The test with an X-Axis excitation at the transverse modal frequency from the sweep test, a Z-Axis excitation at the axial modal frequency, and a biaxial excitation of both profiles. Unlike the 6 Hz accelerometer data in the previous section, there is only one manure of estimating the linear super position of this test matrix. This is to add the response from the first two tests. Below shows the results from this testing on Samples 2, 4, and 5. Similar to the previous two testing methods, the accelerometer data is taken directly from the Signal Star. There are three replicates per testing condition, which are averaged together to a single signal. The following is the FFT averaged responses to the different testing condition from the testing matrix as well as the linear superposition of the first two uniaxial tests.

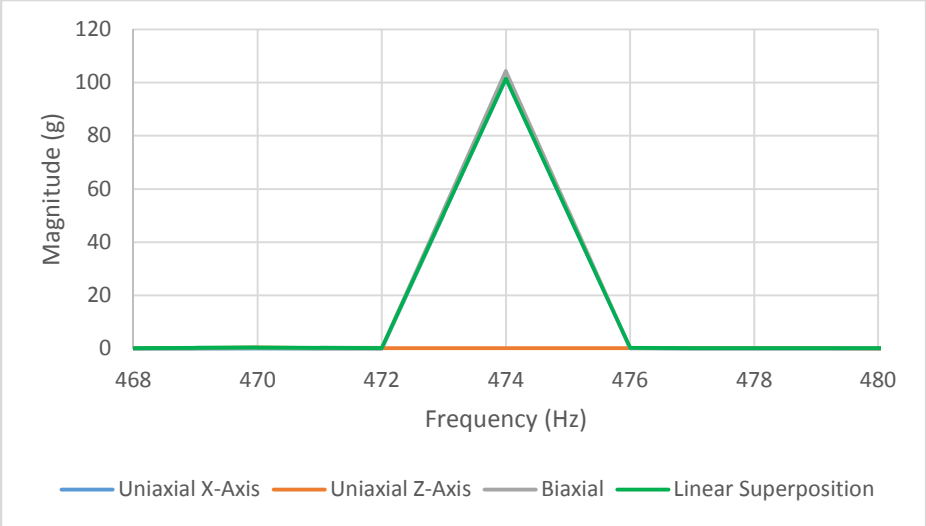

Figure 4-18: Sample 2 1 Hz Bandwidth Acceleration Response

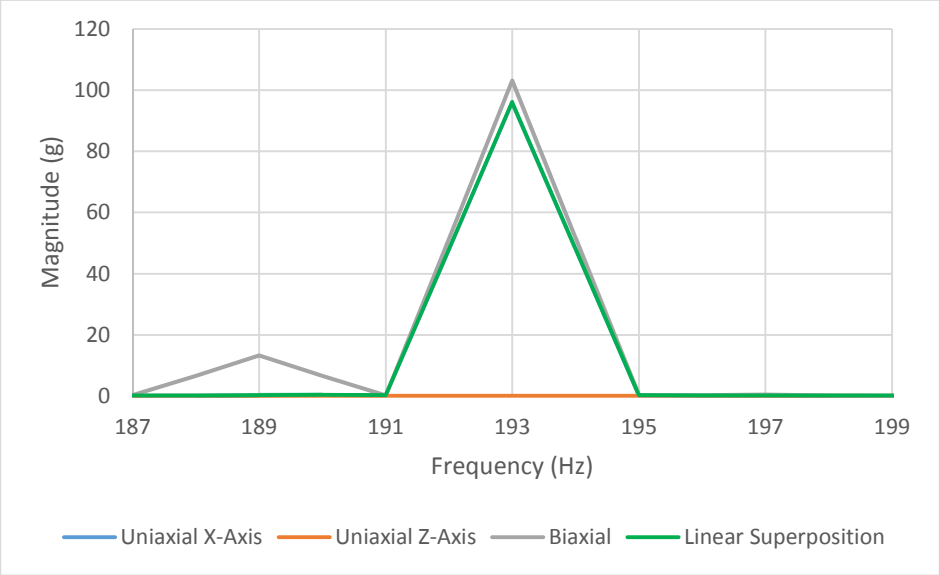

Figure 4-19: Sample 4 1 Hz Bandwidth Acceleration Response

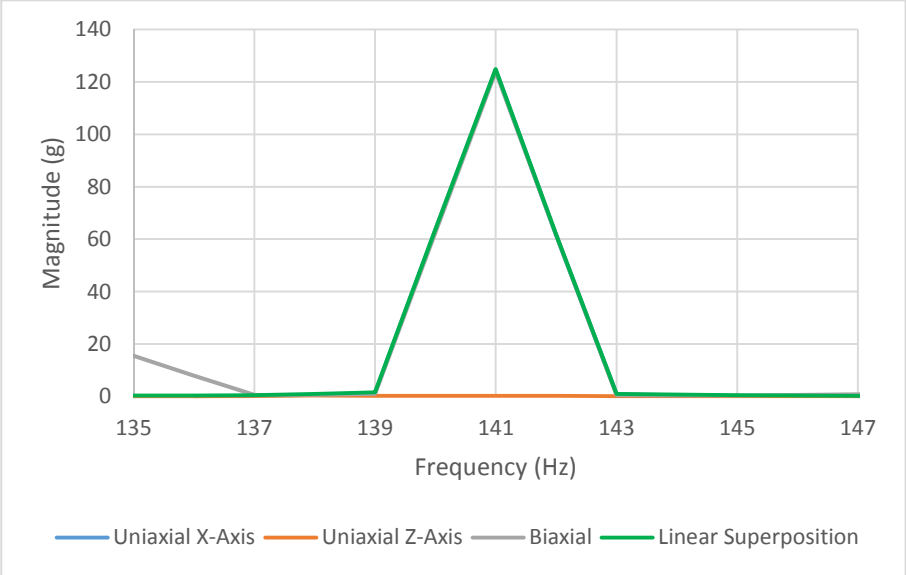

Figure 4-20: Sample 5 1 Hz Bandwidth Acceleration Response

Additionally, strain gauge data is collected for these three samples. The post processing procedure is the same as that of the strain gauge data from Section 4.2.1. The data is first trimmed to only include the response to the excitation profiles. The data is then split into different size data chunks with around 50% overlap for the specific FFT resolution. FFTs are taken of these data chunks, put through a Hanning windowing function, and averaged together to form a single signal per replicate. Then the three replicates per test from the test matrix are averaged together to form a single signal per test. The following figures are the results for each sample tested under each of the three resolutions.

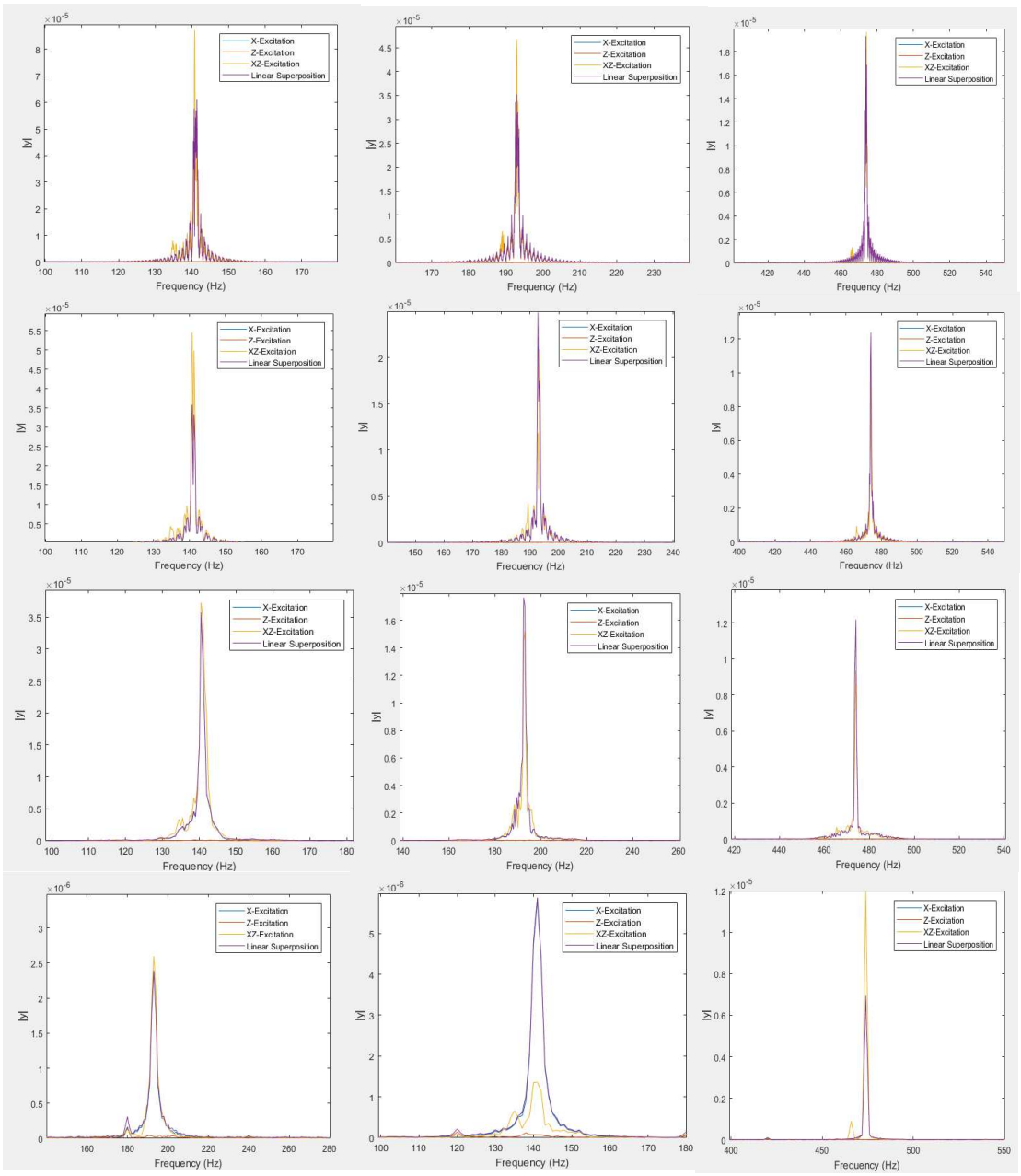

Figure 4-21: 1 Hz Bandwidth Strain FFT Response
[Sample 2 (Left Column), Sample 4 (Middle Column), Sample (Right Column)]
[.1 Hz Resolution (1st Row), .25 Hz Resolution (2nd Row), .5 Hz Resolution (3rd Row), 1 Hz Resolution (4th Row)]

Section 4.5.2: 1 Hz Bandwidth Analysis

Similar to the broadband random excitation profile testing, the 1 Hz bandwidth random excitation profile testing both strain gauge and accelerometer data. Keeping the post-processing the same, all of the data points from both the accelerometer FFT of 1 Hz resolution from the Signal Star software as well as the strain gauge FFT at multiple resolutions.

The figures below show the results of the accelerometer global Normalized difference for the tested samples for this test matrix. In this case, Samples 2, 4, and 5 are tested. A few things can be noted about these graphs. The first is that the Normalized difference peaks are drastically narrower to that of the 6 Hz bandwidth and the broadband FFTs. This makes sense, since the excitation profile is the narrowest out of the three testing strategies. The second is that there are a few higher order peaks. This can either be seen as noise or interference from higher order modes. The last notable difference in this result is that there is purely positive peaks rather than both positive and negative peaks. This is also to be expected, since the narrow bandwidth does not change the phase of excitation as much as the broadband.

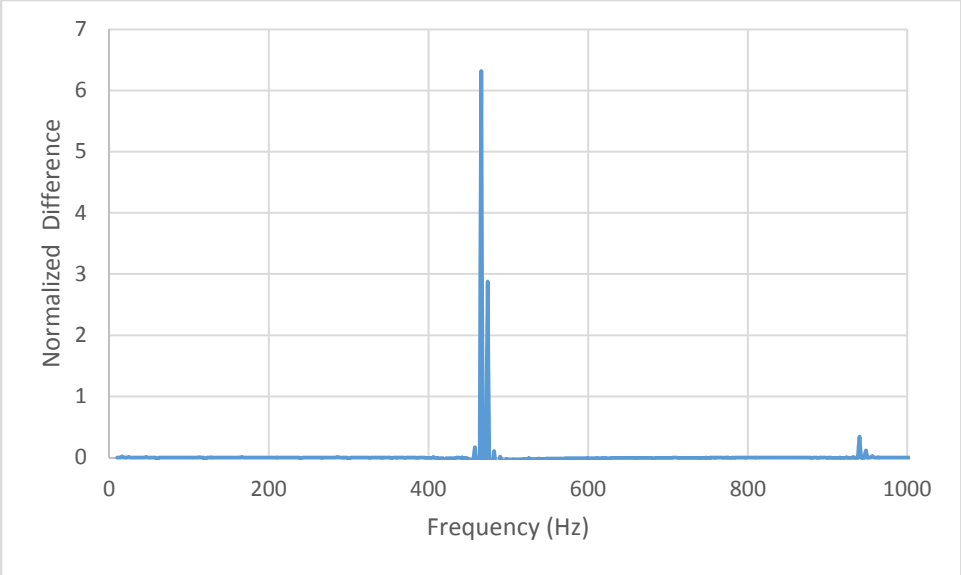

Figure 4-22: Sample 2 1 Hz Bandwidth Acceleration FFT Normalized Difference

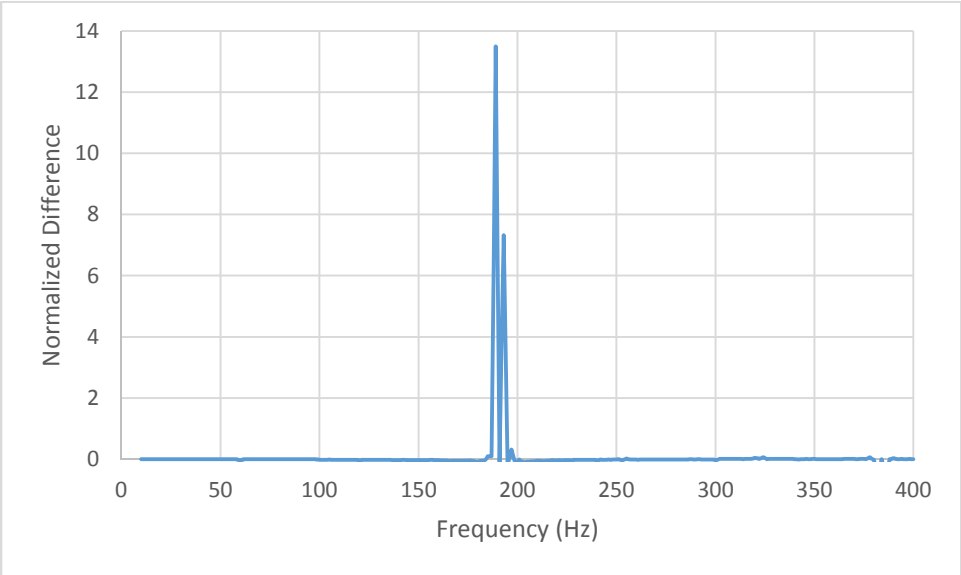

Figure 4-23: Sample 4 1 Hz Bandwidth Acceleration FFT Normalized Difference

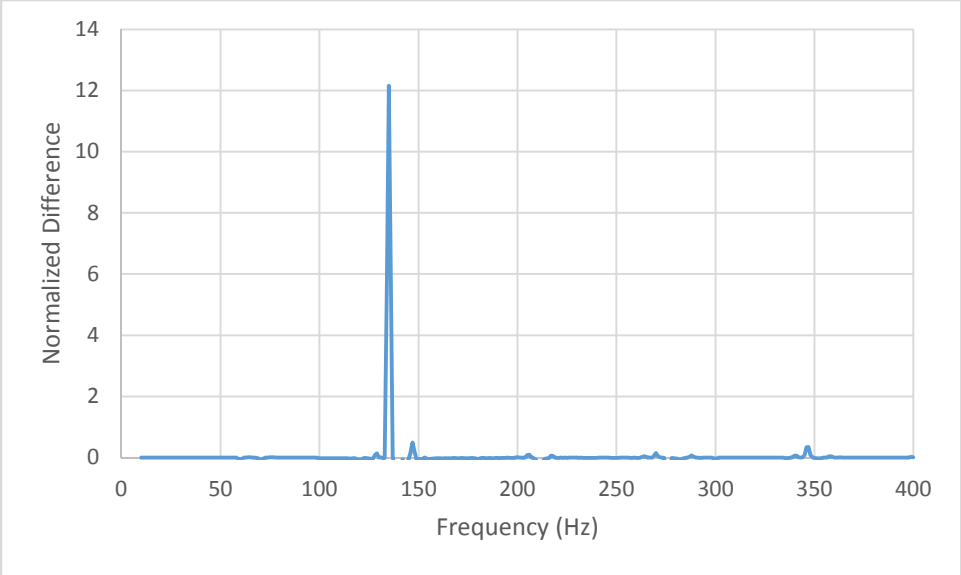

Figure 4-24: Sample 5 1 Hz Bandwidth Acceleration FFT Normalized difference

The next thing to compare is how the peaks of the Normalized difference match the trend of the other. Unlike the accelerometer graphs from the broadband section, this section will only show the positive peaks of the results. The graph below shows the positive peaks of the smallest Sample 2 to the largest Sample 5. The conclusion drawn from the figure below is based on the slope of the line. It is true that the smallest sample has a significantly smaller peak than the largest sample, but sample 4 has a slightly higher peak value to that of sample 5. The general trend of the data converges to linearity as the samples decrease in size, which adds to the evidence that has been gathered for this theory. The results from Sample 4 push the question further. Is the trend of linearity versus size more complex, or is there error in the testing strategy for the 1 Hz bandwidth random excitation.

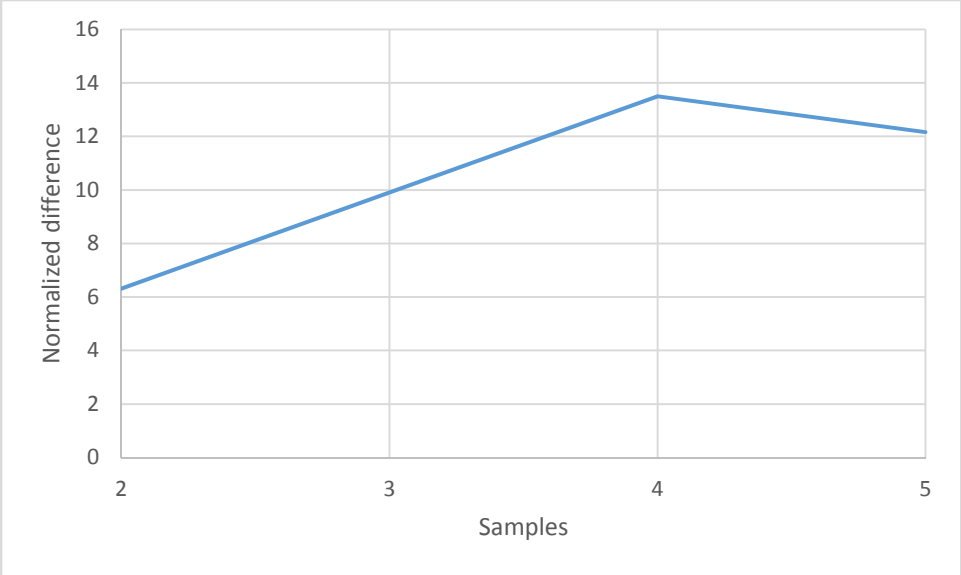

Figure 4-25: 1 Hz Bandwidth Acceleration FFT Normalized difference peaks for Tested Samples

There are a few errors that could add to the complexity of the figure above. The first error, as discussed with the narrow bandwidth random excitation results, is the uncertainty of the phase. As discussed earlier, the negative peak not being relatively present in the acceleration FFT is evidence that the phase is not changing significantly. This phase disparity my cause a difference in Normalized difference amplitude between phases to cause uncertainty in the exact trend. The general trend, however, would not be effected. The other potential error is the resolution of the test. As will be discussed later, since the positive and negative peaks are at the modal frequency, and the excitation profile is incredibly fine onto the frequency of the response, a very fine resolution is needed to see a correct result of the system.

The second type of data collected, the strain gauges, are sent through the same post processing as that of the broadband strain gauge data. The results from the linear superposition and the biaxial excitation are used to find a normalized difference. The results below show the results of each sample, with the smallest on the left and largest on the right, with different FFT resolution becoming coarse further down the page.

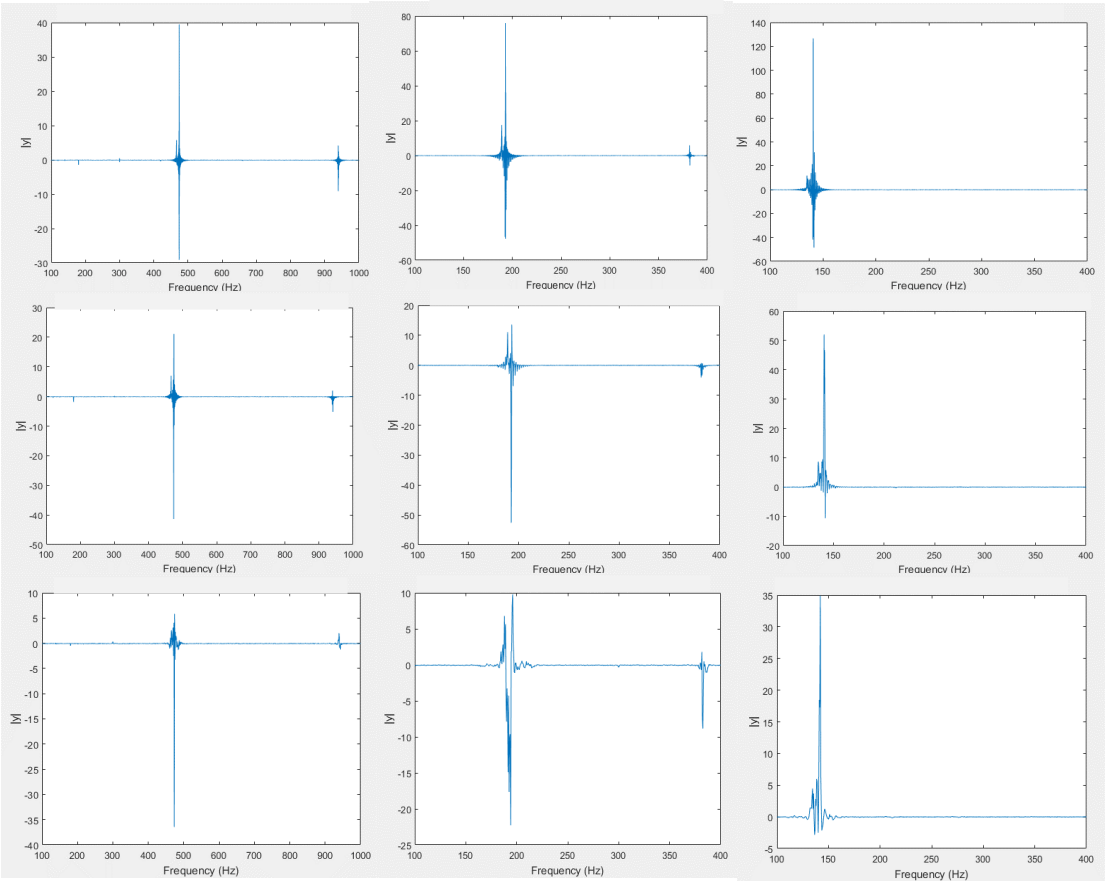

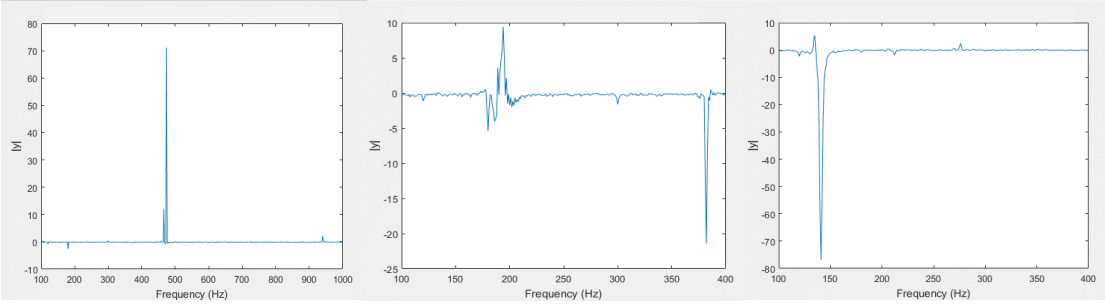

Figure 4-26: 1 Hz Bandwidth Strain FFT Normalized difference [Sample 2 (Left Column), Sample 4 (Middle Column), Sample (Right Column)] [.1 Hz Resolution (1st Row), .25 Hz Resolution (2nd Row), .5 Hz Resolution (3rd Row), 1 Hz Resolution (4th Row)]

There are a few conclussions that can be drawn from this data. Unlike the strain gauge results for the broadband random excitation, there is uncertainty about the existence of both a positive and negative peak as the resolution becomes coarser. This is a result of the narrow bandwidth of the excitation, and is the illustrates the main issue in the accelerometer result. The peaks of the Normalized difference are significantly more narrow than that of the broadband excitation profile. Therefore, a higher resolution is needed to properly understand the behavior and relate the parametric result. This, too, can be a reason to discount the acceleration data altogether, which is based on an averaging method of Signal Star with an FFT resolution of 1 Hz. The result of that coarse of an FFT on the strain gauge data gives relatively small usefulness in understanding the behavior as not only is there no evidence of both a positive and negative peak, but the amplitudes change rapidy from that of the .5 Hz resolution.

The data from the FFT global Normalized differences above in Figure 4-18 are related paremetrically the same way as the broadband strain gauge data. The result, shown in Figure 4-19, illustrates the main issue facing the data collection

uSineg this testing method. As the datas resolution becomes increaSinegly coarse, there is a significant amount of information lost in the amplitudes that could result in false analysis of the system. In this case, the finest resolution, shown in Figure 4-19 in green and again in Figure 4-20, fits the previous conclussions as the Normalized difference significantly decreases as the sample size becomes smaller. This trend becomes slightly distorted in the .25 and .5 Hz resolution, shown in green and purple, respectively. The amplidudes have been reduced, but the same underlying convergence to linearity is present. The result is then completely lost with a resolution of 1 Hz. This is a significant placement for loss of information, because it is the width of the excitation to begin with. Therefore, it is very likely that the correct behavior of the system can only be observed when the resolution of the post-procesSineg is significantly smaller to the bandwidth of the Sineusoidal response.

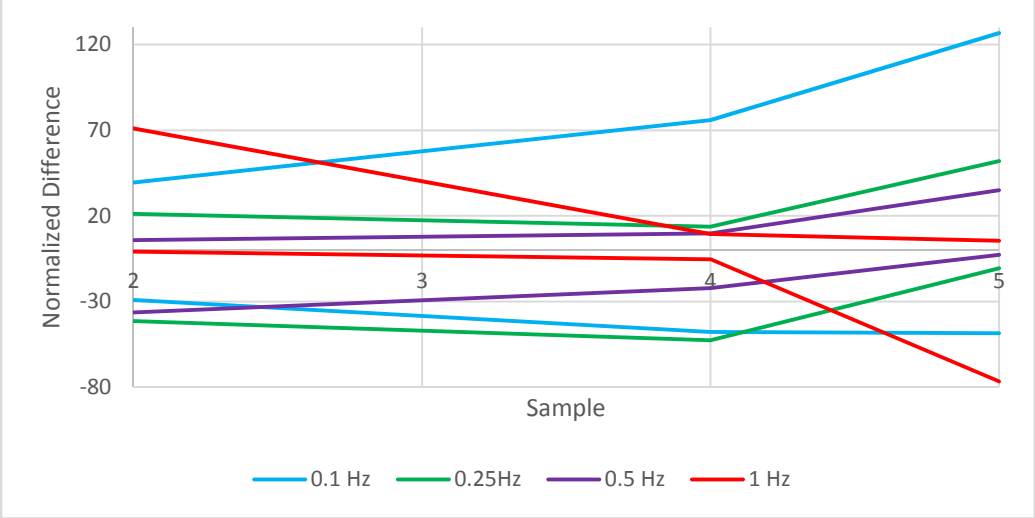

Figure 4-27: 1 Hz Bandwidth Strain FFT Normalized Difference peaks for Tested Samples

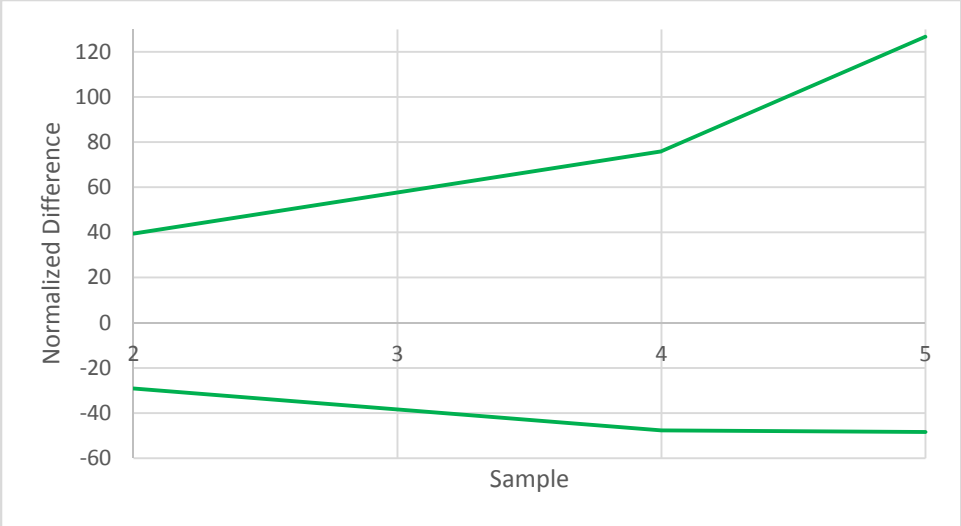

Figure 4-28: .1 Hz Bandwidth Strain FFT Normalized Difference peaks for Tested Samples

Illustrating this further, the difference between the negative and positive peaks are taken, and displayed in Figure 4-21. As the figure shows, a clear trend is present with the fine resolution of .1 Hz. This trend becomes significantly reduced and distorted using .25 and .5 Hz resolution. Then, a complete loss of information leads to a complex result from the 1 Hz resolution.

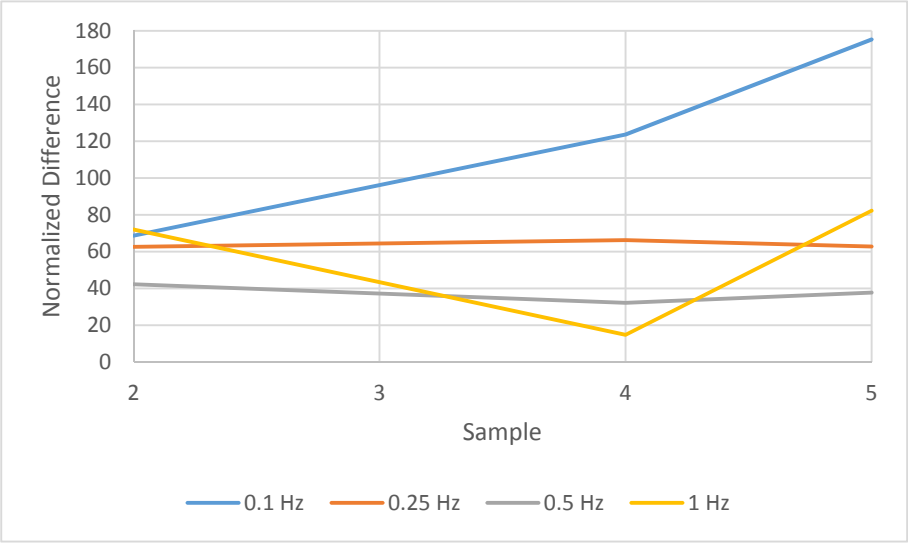

Figure 4-29: 1 Hz Bandwidth Strain FFT Normalized Difference peaks for Tested Samples

In summary, using a fine resolution on the 1 Hz bandwidth random excitation profile, the nonlinear amplification factor dramatically reduces as the sample reduces in size. In addition, the changing of the resolution of the FFT dramatically changed the resulting end conclusion, when the same could not be said when the resolution is changed under broadband random excitation. This leads to the conclusion that the resolution of the result needs to be significantly less then the bandwidth of the excitation.

Chapter 5: Finite Element Analysis of Experimental Result

Section 5.1: Introduction

The last step in the research strategy to confirm the conclusions discussed in Chapter 4 through Finite Element Analysis. The goal of this section is to create a model that closely resembles that of the experimental specimens, and test it under similar conditions to bring about results similar to that of those share in the previous chapter.

The FEA analysis done for this research is split into three sections. The first is the deformable geometry. When designing the sample geometry, 3D deformable objects are used with hexahedron elements. Since the analysis in this section is focused on the deformation of the underlying geometry, a simplified Timoshenko Beam is used for all FEA samples. The second section is the material properties. Since dynamic FEA is being done, the damping material parameters are needed in addition to the material parameters used for modal analysis in Chapter 2. The last section of the FEA analysis is the boundary conditions. Under modal analysis, the base needed to be completely constrained to understand the specific mode shapes. Under dynamic analysis, the base needs to be excited in a similar fashion to that of the experimenting conditions. Therefore, acceleration constraints are put on the base for this analysis.

Damping is a complex concept to understand, because the coefficients of damping change, depending on the geometry and material being used in the analysis. Based on this complexity, damping parameters need to be selected for each sample used in the FEA. In this analysis, Rayleigh Damping coefficient are selected.

Rayleigh Damping uses the stiffness and mass matrices to create the damping matrix using the following equation:

$$C = \alpha M + \beta K \qquad \text{Equation 5-1}$$

Since these coefficients change with the geometry of the sample as well as the material, the coefficients can be selected by calibrating the coefficients to a specific testing condition. What is meant by this is that the results of a single testing case will be used for each sample being analyzed to calibrate the Rayleigh Damping coefficients. Next, those Rayleigh Damping setting will be used under other testing conditions to develop a results that can be related to the experimental data.

When modeling the deformable geometry, the Timoshenko Beams are created to match the lengths of the sample. The cross section of the beams are selected based on the parameters of the design modeling of Table 2-1. These cross sections are changed near the meeting point of the two beams. As discussed in Section 3.1, the samples are manufactured with a mill. This process left a fillet of a radius of an eighth of an inch. With an accuracy of 1/32nd of an inch, the cross section recreated the manufactured fillet to fit the experimental setup as close as possible.

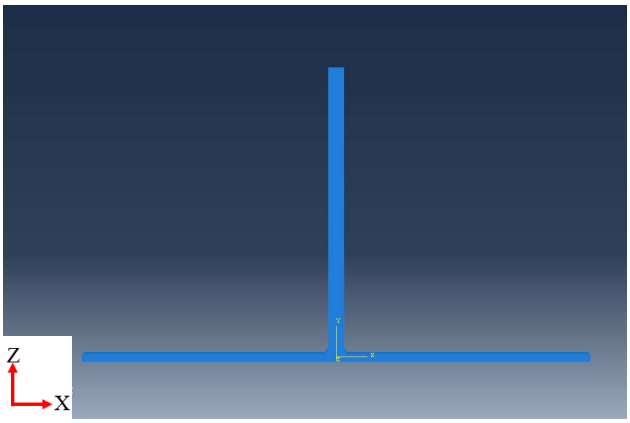

Figure 5-1: FEA Sample Model

Sinece the model needs to be calibrated to a specific testing condition, it is important to keep the accuracy where it is most needed and give up some accuracy when it is not critical so the execution time can be conserved. In other words, a design for FEA needs to be considered when modeling for dynamic analysis, Sinece a Sinegle simulation can take anywhere from a few seconds to a few hours depending on the setup. The main place where this consideration takes place is during the meshing of the model. There are two requirements that are critical to have a correct solution. The first is that the model needs to have a symmetric mesh. This is to ensure accuracy of frequency information as well as dynamic behavior. The second is that the mesh needs to be fine at important geometric locations as well as measurement sights. This is to ensure accuracy of dynamic behavior as well as the measurements made. USineg these two rules, the following mesh is made in the figure below. As seen, the mesh is symmetric and the mesh is fine near the strain gauge locations as well as the meeting location of the two beams.

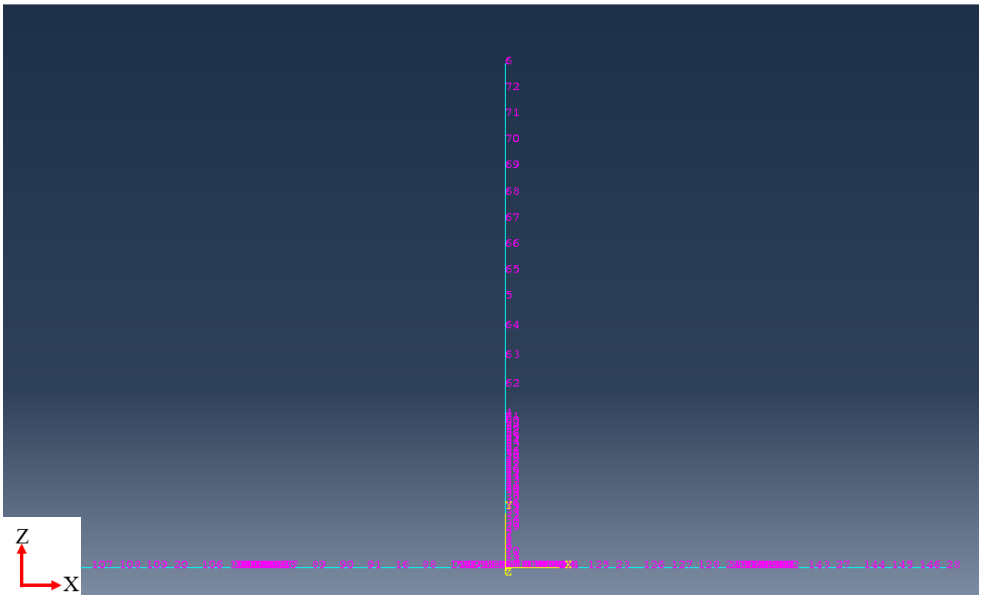

Figure 5-2: FEA Model Mesh

Section 5.2: Broadband Excitation

It has been discussed that base acceleration will be set for a dynamic analysis of the systems. The question still remains is what excitation will be applied to the base. In this section, the analysis being discussed is that of FEA simulation of broadband random excitation. Therefore, the acceleration being used for the base is the table acceleration measured while running the experiments for broadband random excitation. This comes with some caveats, and limitations that will need to be understood for this FEA model. The first is the resolution of the excitation. The resolution of the dynamic excitation of the model is limited to the resolution of the data that is given to it. In this case, the resolution of the table acceleration data. The caveat for this limitation is the further analysis of the FEA model and how well it will fit the experimental result. The FFT will have a limited FFT resolution based on the data input from the table accelerometer. As seen from the effect of a coarse resolution in Section 4.5.2, this limitation can be detrimental to the overall result. Luckily, a coarse excitation has not been seen to be effective on the broadband random excitation in the experimenting.

The model is run through an implicit dynamic analysis in Abaqus under multiple Rayleigh Coefficients to calibration the model to the testing response to broadband excitation in the X-Axis. The spectral FFT of the time history from the table accelerometer used in the acceleration constraints is made to find a baseline of what the post-processed FEA base acceleration FFT should look like. Next, an FFT of the experimental tip response from the same time history as the table accelerometer. This provides a value to match the model tip response to. After each simulation

iteration, the same analysis on the time histories is done on the FEA time histories. The table accelerometers FFTs matched from the FEA and experiment, but the tip response changed based on the damping conditions. If the FEA tip response FFT is too low relative to the experimental tip response FFT, the damping coefficients are lowered, and vice versa if the tip response is too high. Eventually, an iteration is reached that closely matched both the tip response and table excitation. The matched tables and the Rayleigh Damping Coefficients used are shown below.

	Sample 4		Sample 5	
	Experiment	Model	Experiment	Model
Table Acceleration	1.381	1.381	3.317	3.317
Tip Response	18.73	18.68	30.23	30.06

Table 5-1: Broadband Random Excitation Matching Table

Sample 4		Sample 5	
Alpha	Beta	Alpha	Beta
0.995	2.10E-05	0.995	6.00E-05

Table 5-2: Broadband Random Excitation Rayleigh Damping

Once the broadband FEA had been properly calibrated, the same Rayleigh Coefficients are used to for biaxial broadband random excitation. The data from the X-Axis Excitation and biaxial excitation are then post-processed the same way as described in the Chapter 4. An FFT is made from the tip acceleration response and Beam 2 Strain Gauge for both conditions, and the global normalized difference is taken at every point in the FFT graphs using Equation 4-1. Below shows both of the FFTs of both the tip accelerometer and the strain gauge for Sample 4 and 5. In each graph is a signal for the X-Axis broadband random excitation, shown in blue, and a biaxial broadband random excitation, shown in red.

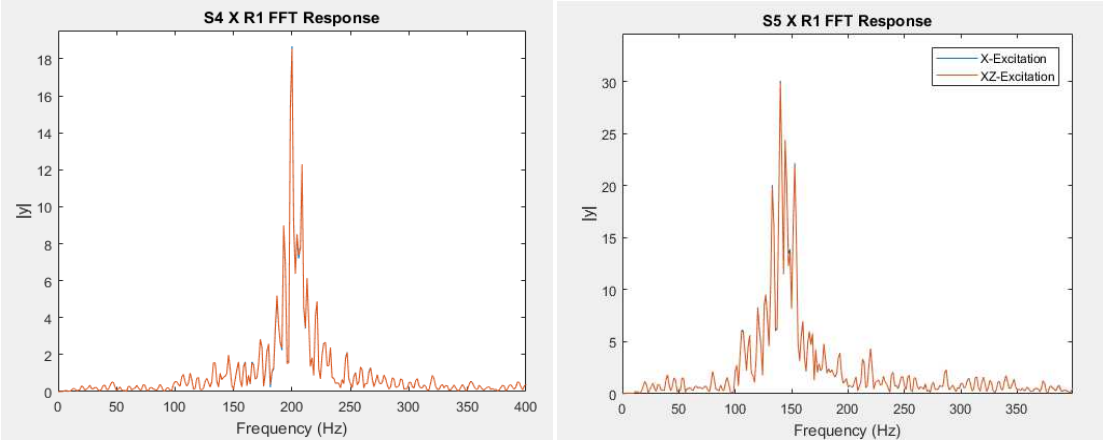

Figure 5-3: Broadband Random Excitation FEA Tip Acceleration Response FFT

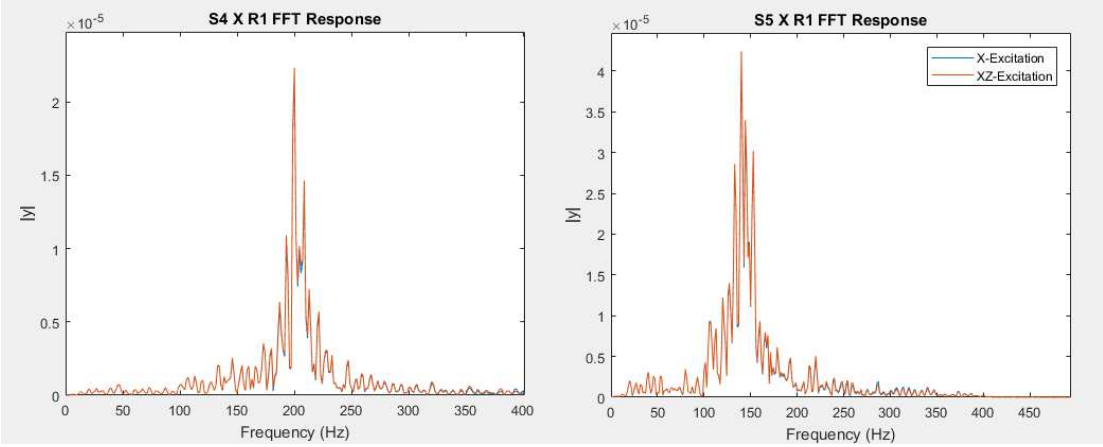

Figure 5-4: Broadband Random Excitation FEA Strain Gauge FFT Response

Sinece the response of the X-Axis excitation and biaxial excitation are closely related under the FEA conditions, the figure above does not accurately show both signals. The global Normalized difference below shows the difference between the two testing conditions. These figures have some significant similarities and differences between the experimental result of the broadband random excitation testing. Both the normalized difference from the FEA and experimental normalized

difference for the strain gauges have two peaks, one positive and one negative. In addition, the peaks are so close to each other that they can be thought of at the same frequency mode. Both the experiment and FEA Normalized difference share the same frequency information, which shows that the model is comparable with that of the actual structure. Conversely, the Normalized difference of the accelerometer in the FEA has two peaks while the experimental Normalized difference of the accelerometer only had a Sinegle peak. The cause of this may be the difference in post-procesSineg, Sinece the acceleration FFT data was collected directly from Signal Star while the FEA created the FFT from the time histories. Additionally, the FEA has peak values that are significantly lower than the result from the experiment. As seen from the difference in FFT resolutions in the experiment, the amplitudes did decrease, but the parametric trend remained the same.

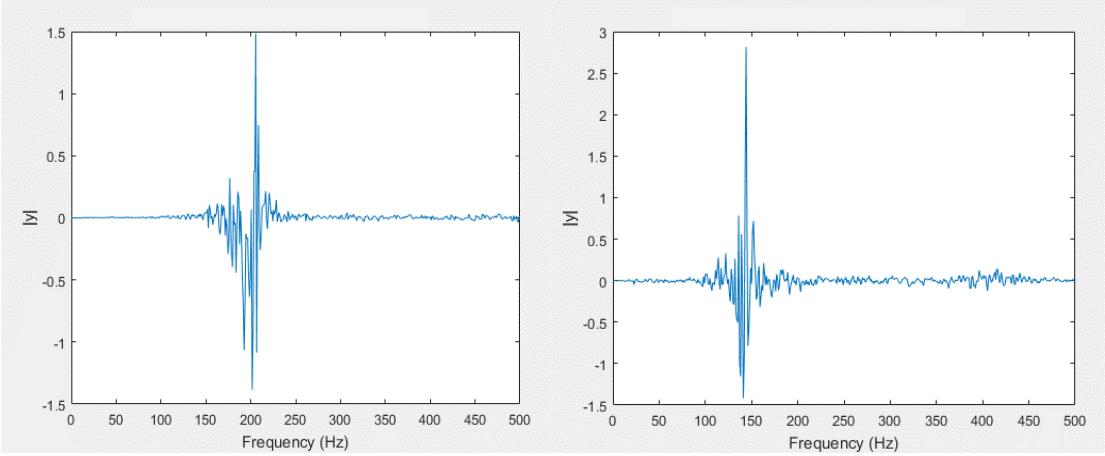

Figure 5-5: Broadband Random Excitation FEA Tip Acceleration Global Normalized Difference

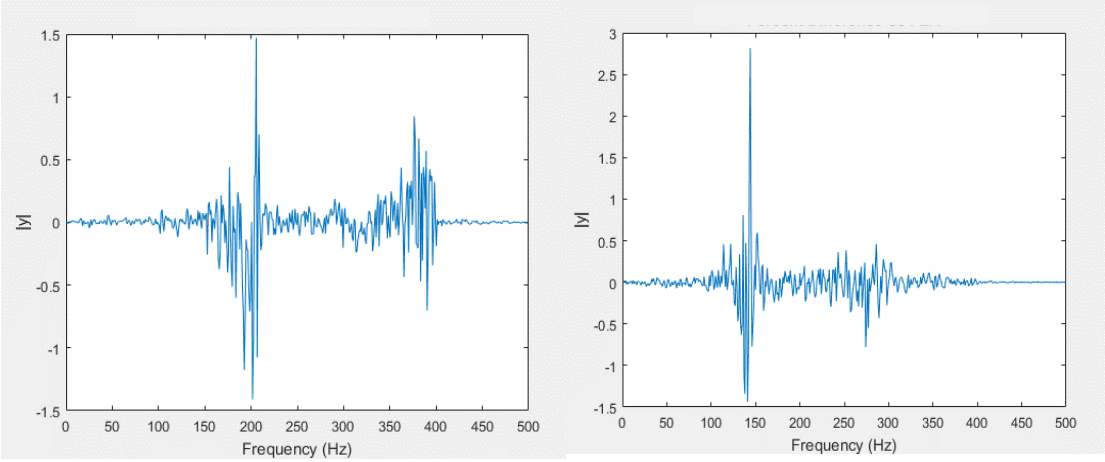

Figure 5-6: Broadband Random Excitation FEA Strain Gauge Global Normalized Difference

From these figures, the data between the samples can be related by the peaks. Below shows how the two peaks change from sample to sample. Similar to the trend from the experimental data, the smaller Sample 4 has a significant lower positive and negative peak value then the larger Sample 5. This result is consistent with the trend that is seen from the experimental data for broadband random excitation. This is strong evidence that the nonlinear amplification will reduce as the sample height and mass become smaller.

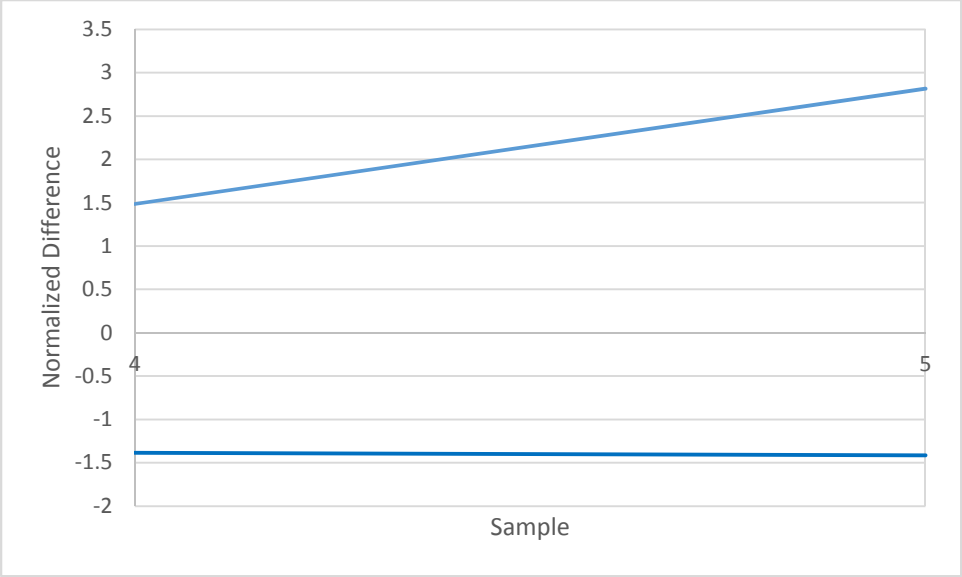

Figure 5-7: Broadband Random Excitation FEA Acceleration Normalized difference Peaks for Tested Samples

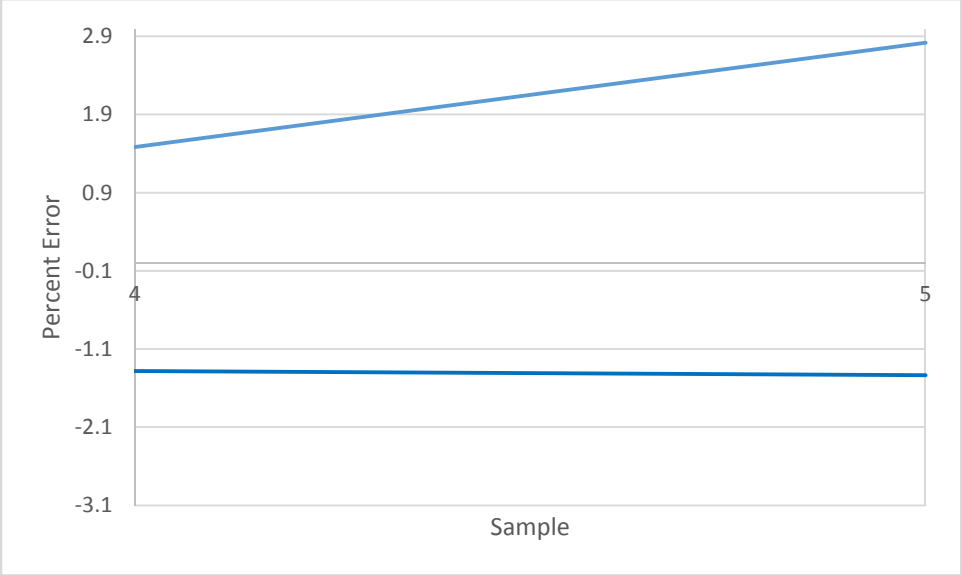

Figure 5-8: Broadband Random Excitation FEA Strain Normalized difference Peaks for Tested Samples

Finally, if these normalized difference graphs from the FEA on broadband random excitation compared with the results from the experimental normalized difference graphs between samples under broadband random excitation, the following

figures are made. In these figures, the end result for the FEA is shown in blue, while the experimental result is shown in red. The trend for both experimental and FEA data becomes closer to zero as the sample size decreases. The main difference between the experiment and the FEA is that there were significantly lower nonlinear amplification factors measured by FEA.

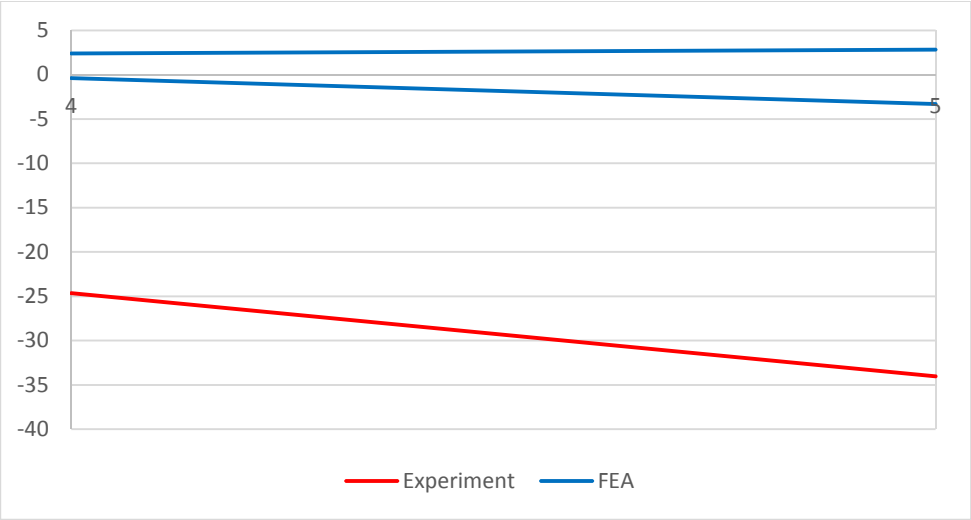

Figure 5-9: Broadband Random Excitation FEA vs Experiment Acceleration Normalized difference Peaks for Tested Samples

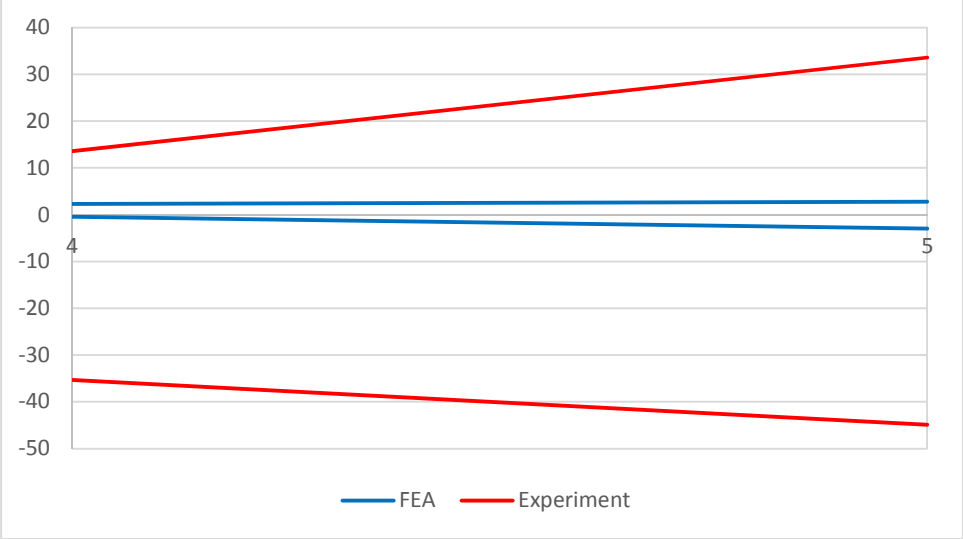

Figure 5-10: Broadband Random Excitation FEA vs Experiment Strain Normalized difference Peaks for Tested Samples

Section 5.3 1 Hz bandwidth FEA Results

Similar to the FEA for broadband random excitation, the 1 Hz narrow bandwidth random excitation uses the table accelerometer from the experimenting as acceleration constraints. Since a different excitation testing method is being used, the same procedure for calibrating the Rayleigh Damping coefficients is used. The table accelerometers are used as a baseline to calibrate to, and the Rayleigh Damping coefficients are changed until the model response fits the experimental response to the X-Excitation testing condition. This calibrated model is then used under biaxial excitation, and post-processed the same ways as Section 5.2. The resulting matching tables and Rayleigh Coefficients used for Sample 2 and 5 are shown below.

	Sample 2		Sample 5	
	Experiment	Model	Experiment	Model
Table Acceleration	6.988	6.988	7.707	7.707
Tip Response	96.04	95.77	115.5	115.9

Table 5-3: 1 Hz Bandwidth Random Excitation Matching Table

Sample 2		Sample 5	
Alpha	Beta	Alpha	Beta
0.995	3.00E-05	0.995	9.17E-05

Table 5-4: 1 Hz Bandwidth Random Excitation Rayleigh Damping

Once the calibration is finished, the time history of the dynamic analysis is collected for the acceleration at the tip, and the strain at the location of the Beam 2 strain gauge. The figures below show how the time histories from the FEA line up with the actual time histories of the experimental data.

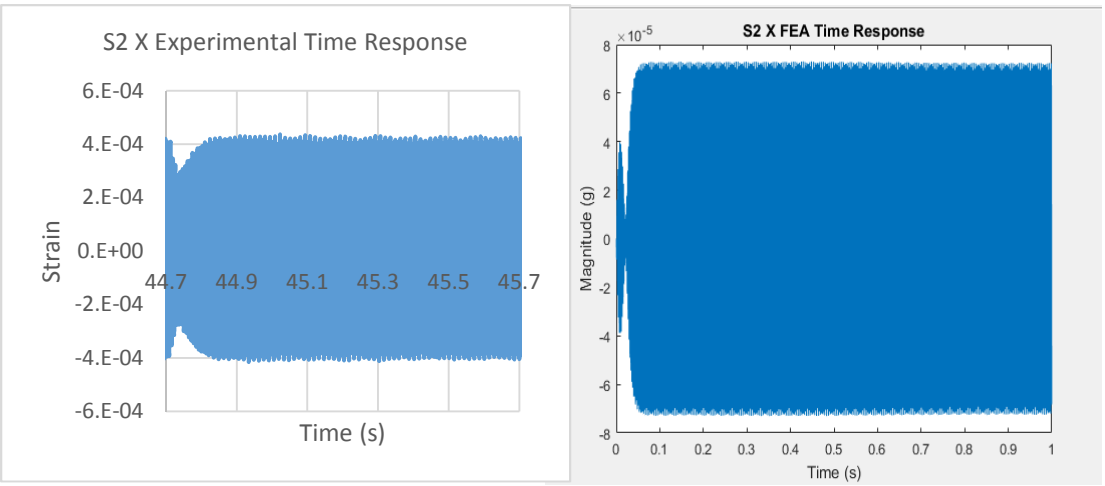

Figure 5-11: 1 Hz Bandwidth X-Axis Excitation Strain Response [Experiment (Left), FEA (Right)]

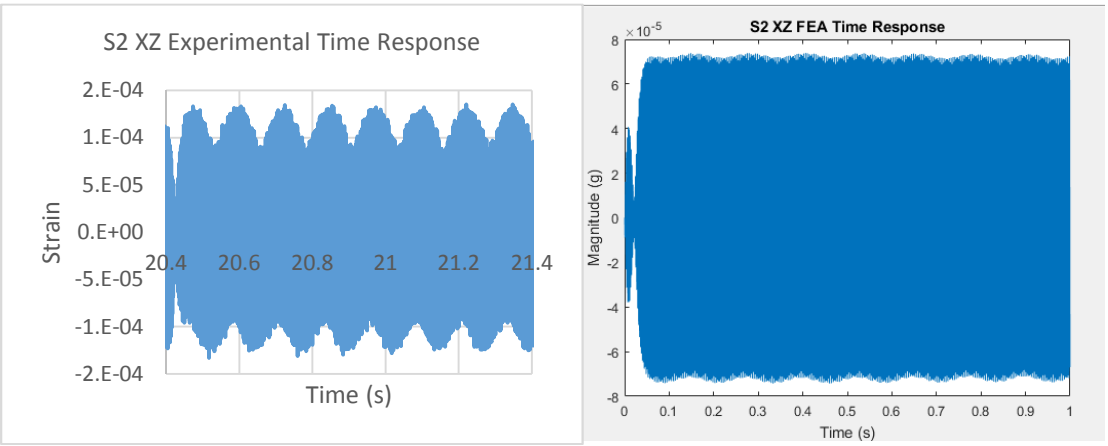

Figure 5-12: 1 Hz Bandwidth XZ-Axis Excitation Strain Response [Experiment (Left), FEA (Right)]

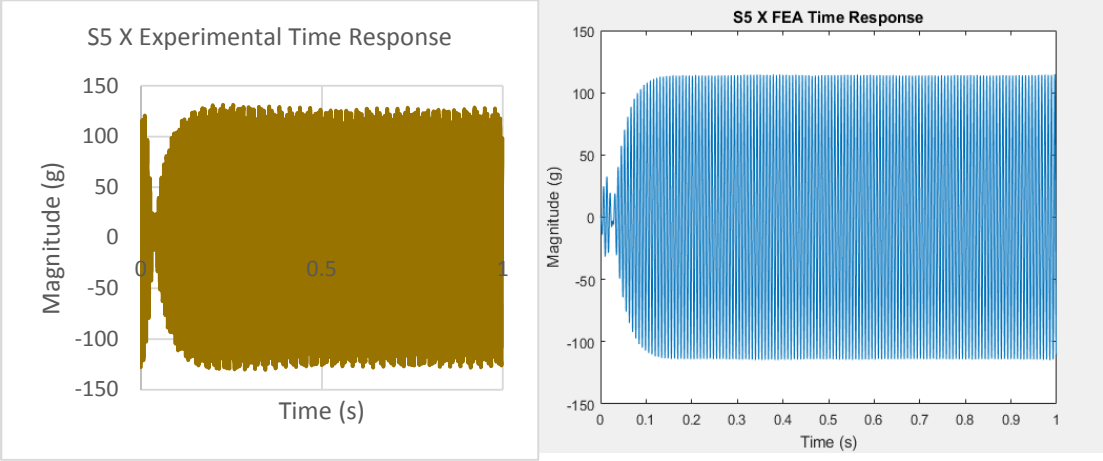

Figure 5-13: 1 Hz Bandwidth X-Axis Excitation Acceleration Response [Experiment (Left), FEA (Right)]

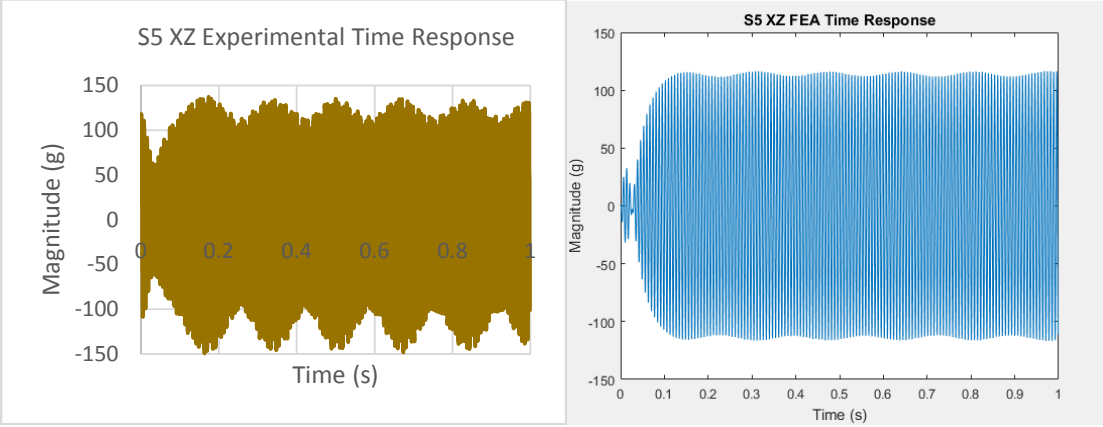

Figure 5-14: 1 Hz Bandwidth XZ-Axis Excitation Acceleration Response [Experiment (Left), FEA (Right)]

As the figures above show, the shape of the time response is nearly the same for both testing conditions. The X-Axis excitation test ramps up to its peak value and remains relatively steady, while the biaxial excitation ramps to a peak value and has a small oscillation on the top. The main difference between the model and the experiment is the strain peak values. As seen in Table 5-3, the calibration was done to match the acceleration tip response. The limitation of this calibration, both for the

narrow bandwidth and broadband random excitation, is that the strain gauge response is not match between the experiment and the model.

Next, the time histories from the figures above are post-processed through the same method as the broadband random excitation as well as the experimental data. An FFT is taken of the strain gauge and acceleration time history responses to yield the figures below.

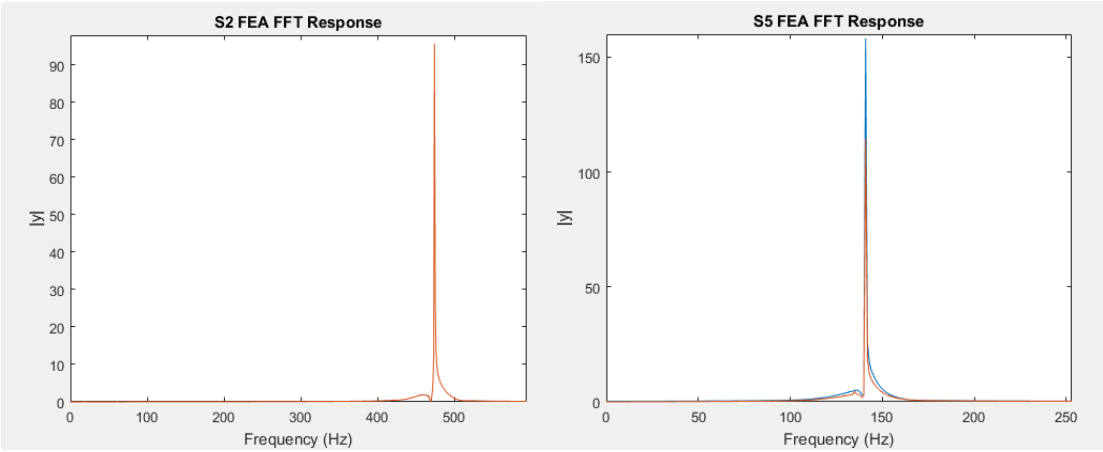

Figure 5-15: 1 Hz Bandwidth XZ-Axis Excitation Acceleration FFT Response [Sample 2 (Left), Sample 5 (Right)]

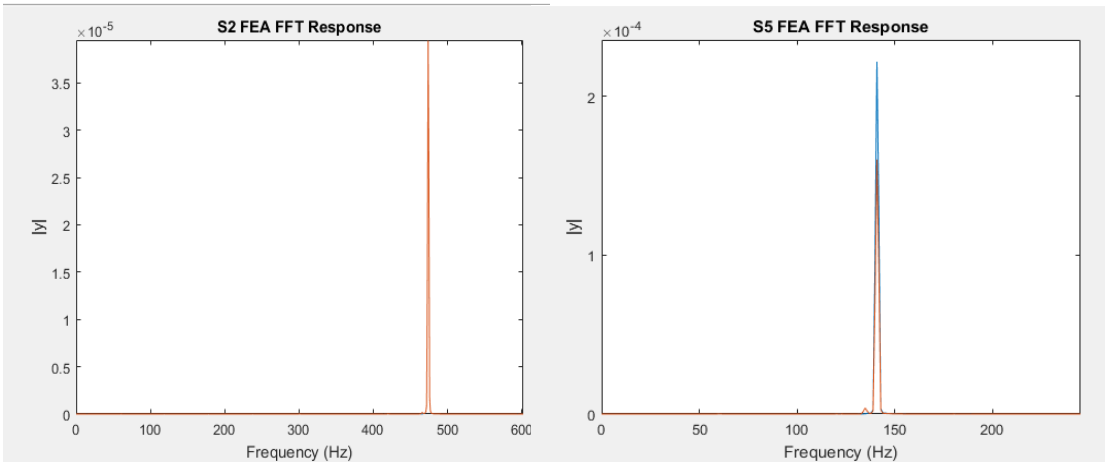

Figure 5-16: 1 Hz Bandwidth XZ-Axis Excitation Strain Gauge FFT Response [Sample 2 (Left), Sample 5 (Right)]

Similar to the FFTs in the experiment and broadband random excitation FEA, these FFTs are converted to normalized difference graphs by using Equation 4-1. The results of this are shown below.

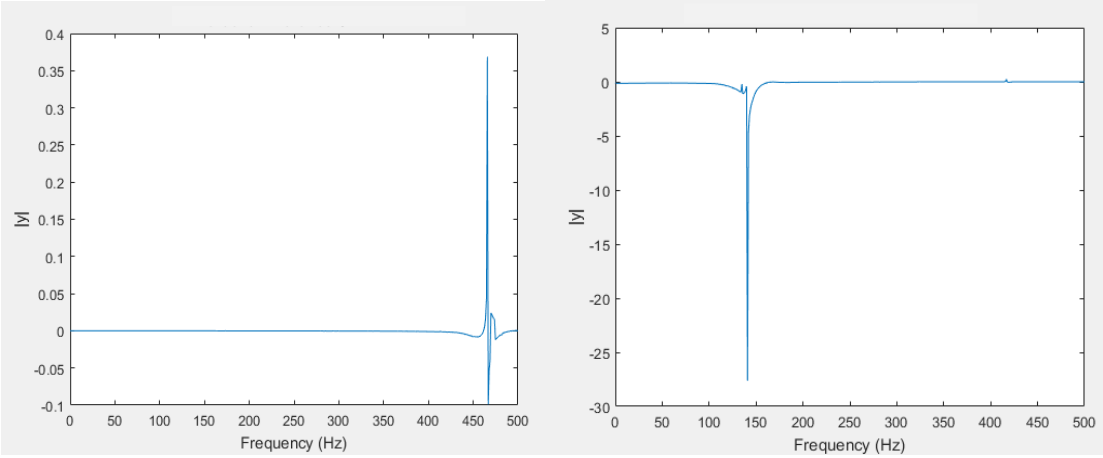

Figure 5-17: 1 Hz Bandwidth XZ-Axis Excitation Acceleration Normalized Difference
[Sample 2 (Left), Sample 5 (Right)]

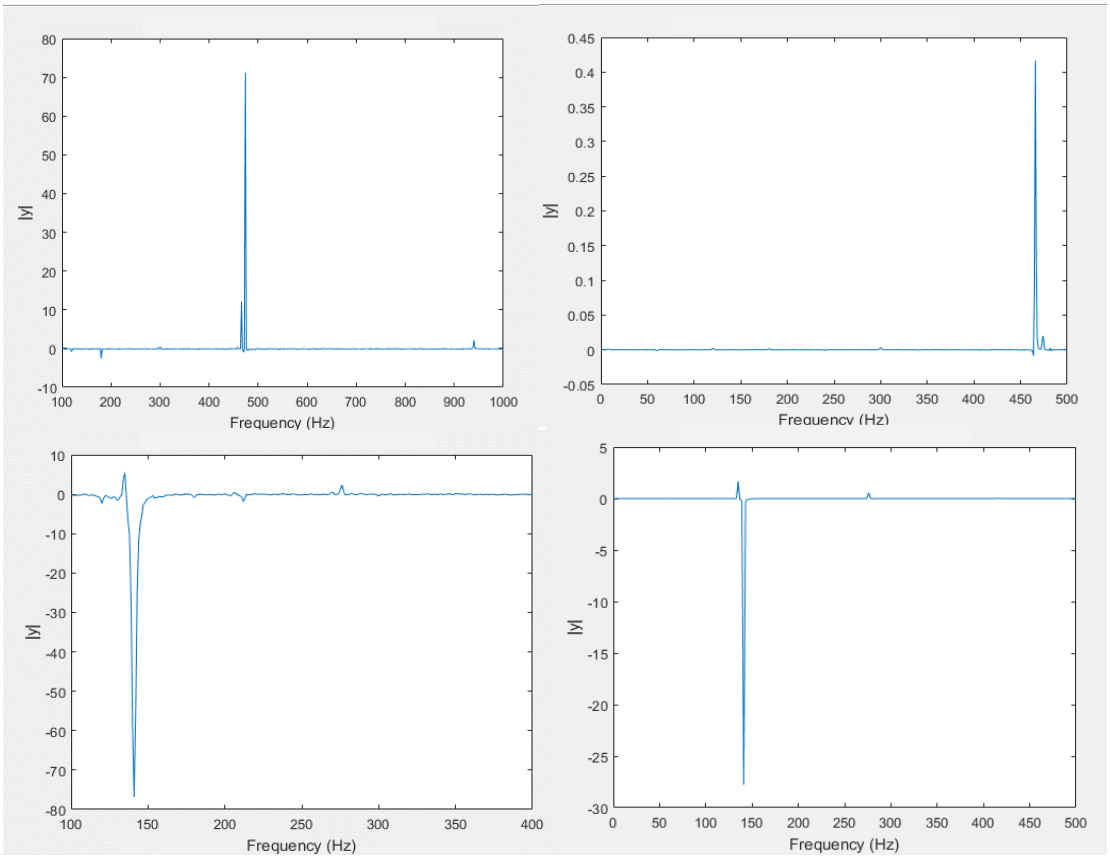

Figure 5-18: 1 Hz Bandwidth XZ-Axis Excitation Strain Gauge Normalized Difference
[Sample 2 Experiment (Top Left), Sample 2 FEA (Top Right)]
[Sample 5 Experiment (Bottom Left), Sample 5 FEA (Bottom Right)]

Before looking at the parametric result between the samples, let's discuss the results shown in Figure 5-16. On the left column is the experimental global normalized difference of the strain gauge data for the 1 Hz bandwidth random excitation under a coarse FFT resolution of 1 Hz. On the right column is the FEA strain gauge result for the 1 Hz bandwidth random excitation with a FFT resolution of around 1 Hz. Being of similar FFT resolutions, it would be expected that these figures would match. As seen, the signal shapes completely line up between the experiment and the FEA. In both cases, Sample 2 has a result of a significant positive peak with a negligible negative peak. Additionally, in both cases Sample 5 has a small positive

peak followed by a much larger negative peak. This is strong evidence that the FEA model response matches the experimental result. The main difference between the experiment and the FEA is the amplitudes. The FEA has a significantly lower peak values for both conditions.

Using these FFT peaks, a parametric look at the peaks can be seen in the figures below. The figures both show a clear trend that matches the trend from the rest of the tests done, both experimentally and in FEA. As the sample reduces in size, the nonlinear amplification dramatically reduces. This result matches the result from the experiment under 1 Hz bandwidth random excitation for fine resolutions, but deteriorated under coarse resolutions. Under the finest resolution possible, given the table acceleration input into the FEA, the trend was not distorted. This gives strong evidence that the conclusion that is drawn about the effect of mass and height on the nonlinear amplification under all tests is correct.

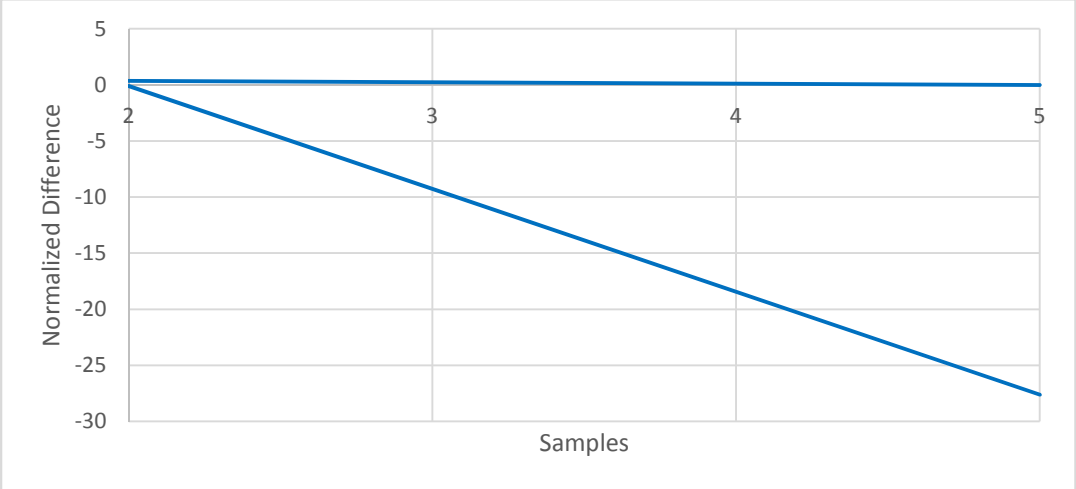

Figure 5-19: 1 Hz Bandwidth FEA FFT Acceleration Normalized Difference peaks for Tested Samples

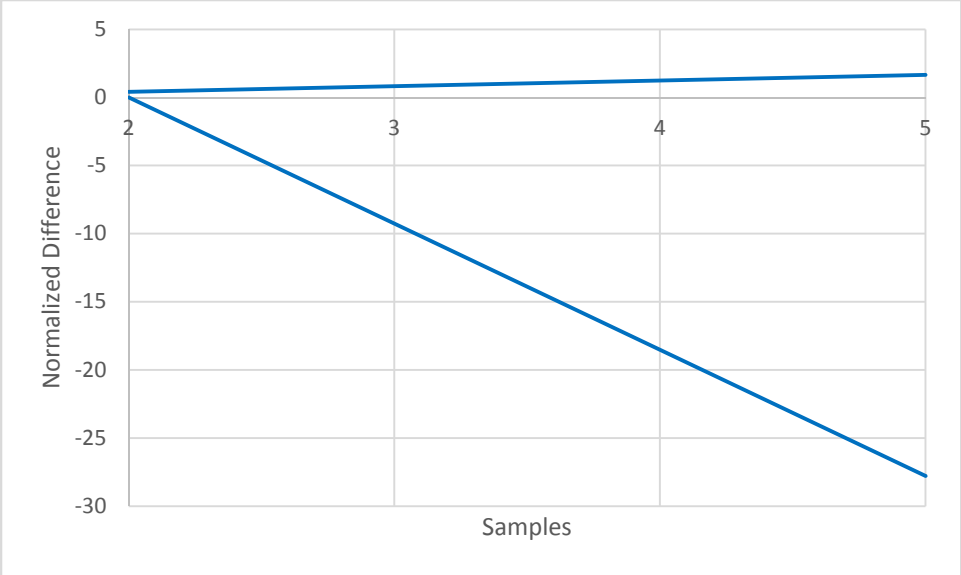

Figure 5-20: 1 Hz Bandwidth FEA FFT Strain Normalized Difference peaks for Tested Samples

Finally, if these normalized difference graphs from the FEA on 1 Hz bandwidth random excitation compared with the results from the experimental normalized difference graphs between samples under 1 Hz bandwidth random excitation, the following figures are made. In these figures, the end result for the FEA is shown in blue, while the experimental result is shown in red. The trend, similar to the broadband random excitation, for both experimental and FEA data becomes closer to zero as the sample size decreases. The main difference between the experiment and the FEA is that there were significantly lower nonlinear amplification factors measured by FEA. This difference is consistent for both the 1 Hz bandwidth random excitation and the broadband random excitation.

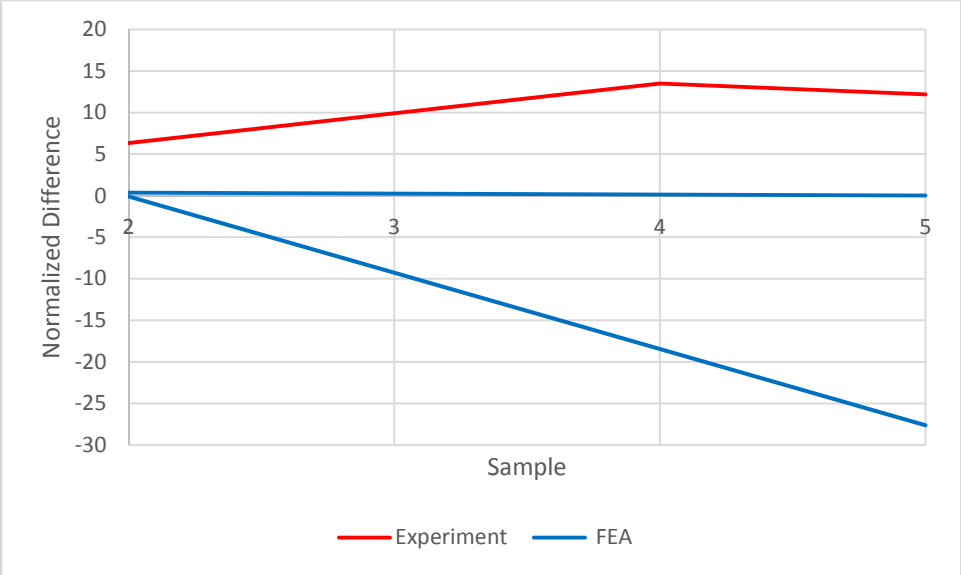

Figure 5-21: 1 Hz Bandwidth FEA vs Experiment FFT Acceleration Normalized Difference peaks for Tested Samples

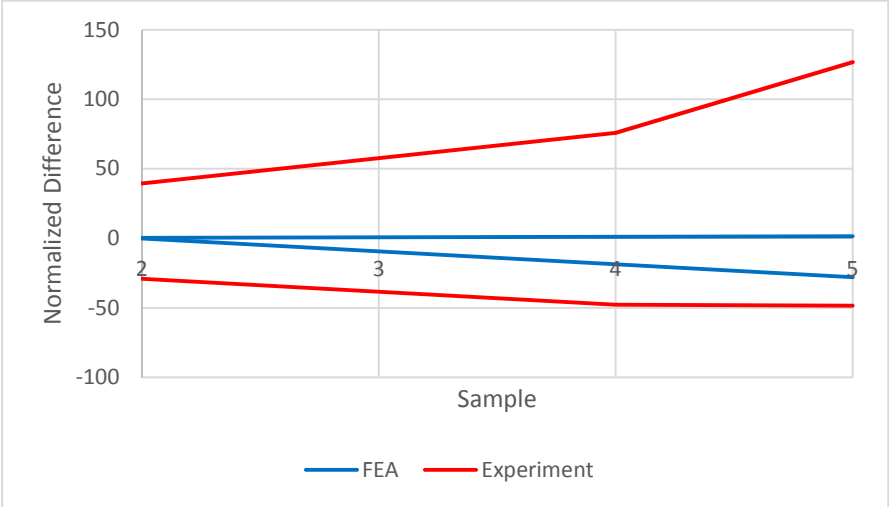

Figure 5-22: 1 Hz Bandwidth FEA vs Experiment FFT Acceleration Normalized Difference peaks for Tested Samples

Chapter 6: Summary, and Future Work

Section 6.1 Introduction

This chapter reviews the work that has been done, and some possible directions for future work that can still be done in the area of multiaxial vibration.

Section 6.2 Summary and Discussions

Revisiting Chapter 1, the goal of this paper is to reveal useful conclusions about when it is necessary to do multiaxial testing on electronic packages. In previous research, it had been discovered that the multiaxial excitation and sample architecture both play a significant rule in the nonlinear amplification. More specifically, an excitation profile with a frequency ratio as well as optimal constructive or destructive phases between axial and transverse vibration optimize the nonlinear response of a component. In addition, the effect of mass and height had been explored in FEA, but not confirmed experimentally.

Therefore, the primary goal of this present study is to experimentally verify the role of component geometry on the severity of nonlinear vibration response under multiaxial excitation along axial direction and transverse direction of the component. These two directions correspond to the out-of-plane and in-plane directions of the PWB. Therefore, five physical samples, consisting of two orthogonal beams each, are designed with a consistent modal frequency ratio of two between their axial and transverse response modes. These double-beam samples are manufactured out of aluminum with consistent cross-sectional dimensions, but with parametrically varying height and length. These samples are instrumented with accelerometers and strain

gauges and tested uniaxially as well as biaxially on the TE6-900 six degree of freedom shaker under three types of excitation profiles.

The first testing profile utilized broadband random excitation profiles with the knowledge that the samples would respond naturally at the frequency ratio of two along axial and transverse directions, due to the modal design constraints. The second testing method, narrow bandwidth random excitation, is an intermediate step for the development of the third testing method. In addition, this complex method showed that a dual frequency random profile is needed for narrow bandwidth excitations. The third method, 1 Hz narrow bandwidth random excitation, is the first time that this TE6-900 shaker has been used with a single controller, to control a shaker at different sinusoidal profiles in different orthogonal directions. This is achieved by generating a pseudo-sinusoidal excitation from narrow-band random excitation profiles.

Data was collected from the tip accelerometer and strain gauge mounted on Beam 2, under these excitation conditions. Consistent post-processing procedures are used for the data. First, an FFT is created under different FFT resolutions. Next, the FFTs are used to form a global normalized difference between the linear superposition of uniaxial testing and the actual biaxial result. The peaks of the global normalized difference are measured and graphed to quantify the trends across different samples. The conclusions formed from all testing methods are consistent, and showed evidence that samples with lower height and mass have significantly less nonlinear amplification compared to the larger, heavier samples.

Finally, the response to both the broadband random excitation and the 1 Hz bandwidth random excitations are modelled in FEA. The modeling procedure is kept

consistent across samples and testing methods. The acceleration history captured from the X-Axis table accelerometers are used as an acceleration input for the FEA model. Rayleigh Damping coefficients are tuned to calibrate the FEA model to the measured acceleration response. With this calibrated model, a biaxial excitation is simulated. Tip acceleration and Beam 2 strain gauge time histories are extracted from the FEA dynamic result. The same post-processing as the experiment is performed on the FEA measurements. First, an FFT is constructed, followed by a global normalized difference graph. The peaks of the global normalized difference are measured and plotted to allow comparison between samples. The excitation response, the FFT, the normalized difference, and the end trend of the data matched the experimental results. This provides quantification of the severity of the nonlinear amplification of the response, as a function of mass and size of the specimen.

Section 6.3 Research Contributions

There are two main contributions that this research has made to the literature on multiaxial vibration. As discussed in Chapter 1, the relation between sample architecture and nonlinear amplification has been explored in prior studies through FEA and other analysis methods. However, this study is the first one to confirm the findings of these simulations experimentally. This is important, because it furthers the understanding of when multiaxial vibration is critical for testing a specific sample. From the testing and FEA conclusion, it is known that a taller, heavier electronic package will need to be tested under multiaxial vibration to understand the overall failure of the package. However, this study provides experimental quantification and

confirmation of the severity of the nonlinear interaction, as a function of the size and mass of the component.

The second contribution this research has made is through the development of the testing method. The TE900 6 DoF shaker currently available for multiaxial testing can provide sinusoidal excitation only at the same frequency in all DOFs. This is the first study where a multiaxial shaker of this design has been used to generate pseudo-sinusoidal excitation at different frequencies along different DOFs. A similar methods exists in uniaxial vibration testing in commercial and industrial areas, such as testing with helicopters. In these methods [5], called sin-on-random profiles, a narrow bandwidth random excitation profile is used in addition to broadband excitation, but only is used in uniaxial excitation. What is new in the community of users of MDOF shakers is the use of a single controller to run different sinusoidal profiles in different directions. This research, therefore, uses narrow bandwidth random profiles to develop a new testing method for multiaxial vibration testing.

Section 6.4 Limitations and Future Work

Although this study answered the question it set out to, there are some serious limitations to the experiment. The first, being the complexity of the sample. The goal of using a double beam setup is to have a robust design of the modal frequency ratio of 2 between the axial and transverse eigen modes. Unfortunately, it is discovered that the nonlinear flexural response rigidity of the horizontal beam (Beam 1) significantly affects the vibration of the vertical beam. Therefore, a simpler specimen is very desirable, using only one nonlinear beam (the vertical beam or Beam 2 of this study), instead of two nonlinear beams. This simpler specimen there is a systematic

error will more effective and accurately quantify the multiaxial nonlinear interaction that we are seeking to experimentally confirming using this sample to accurately see the nonlinear amplification value.

Since this was an error across the board on all the sample, it did not affect the overall qualitative trend being analyzed in this paper. For future work, it would be wise to combat this issue and minimize this problem in one of two ways. The designed sample does not need to overkill the design and have the biaxial frequency ratio of two, since the testing method discovered in this paper found a way to execute the same response frequency ratio through the use of different frequencies in the excitation profiles. Therefore, the next set of samples designed for multiaxial vibration can be a simplified single beam that utilizes the excitation profiles to excite the specimen in the axial and transverse directions at the frequency ratio of two. The second way is to design a sample with a rigid horizontal beam and compliant vertical beam. Under this condition, the flexure of the horizontal beam will not affect the vibration of the vertical beam as much. Once again in this second approach, the axial and transverse excitation should be applied with a frequency ratio of 2.

The next limitation of this study is the resolution of the data collected. If future multiaxial vibration testing moves more to designing samples with the goal of using narrow bandwidth random excitation profiles, the resolution of the data is critical to the analysis of the system. As Section 4.5.2 illustrates, the results of the analyzed data can be is significantly dependent on changed with the resolution of the data under narrow bandwidth random excitation. In this study, a FFT resolution of .1 Hz is achieved in the strain gage results, by taking a round 80,000 samples with of a

5000 Hz sampling rate measurement of a strain gauge. This seems optimal for the analysis of response to 1 Hz bandwidth random excitation profiles.

Further research can also be done conducted in improving the development of the testing method. Since the use of narrow-banding random excitation profiles to achieve sinusoidal excitation is not a common practice in vibration testing, there can be a study done on the effect of a sample on a random excitation profile that parametrically changes from a narrow bandwidth sinusoid profile to a fully random broadband profile.

In addition, the excitation profiles can be pushed further by combining broadband and sinusoidal excitation in the same testing method. For example, in the proposed single-beam specimen, random vibration can be applied in the transverse direction and a sinusoidal excitation can be applied along the axial direction at twice the first modal frequency of the beam.

Finally, the modeling and implicit dynamic simulation can definitely be improved in future testing. In this study, there was a serious limitation to the resolution of the data collected. As discussed earlier, an optimal sampling rate will eliminate the issues seen, that are the cause of poor resolution. One of these errors is getting a clear implicit dynamic simulation under narrow bandwidth random excitation. An accurate simulation can be achieved with an acceleration constraint at a fine resolution and an increased length of the simulation.

Appedices

Appendix A: Design Sample Mode Shapes:

Sample 5 Mode Shapes:

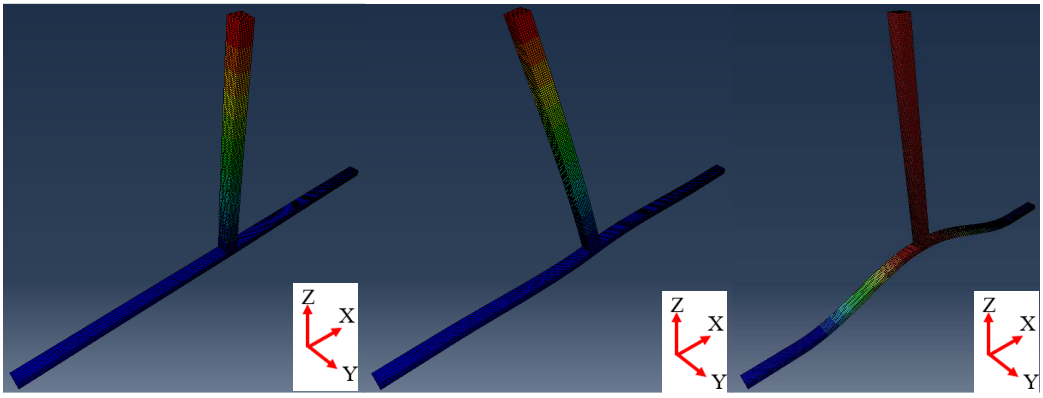

Sample 4 Mode Shapes:

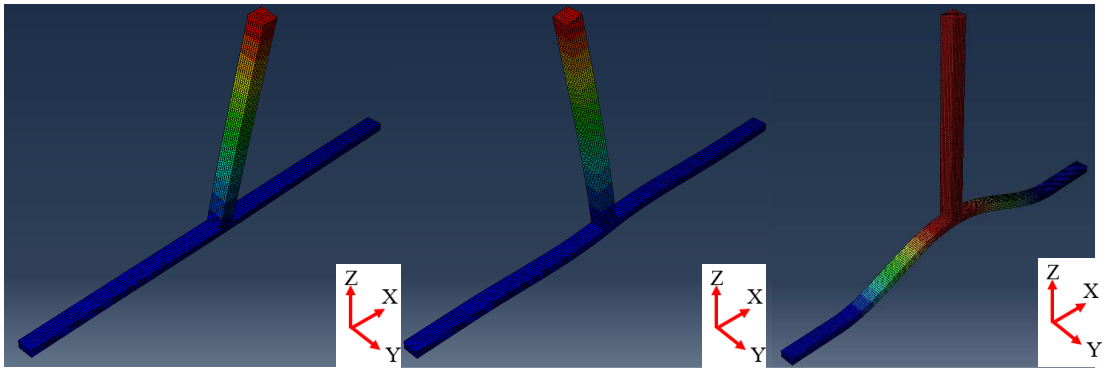

Sample 3 Mode Shapes:

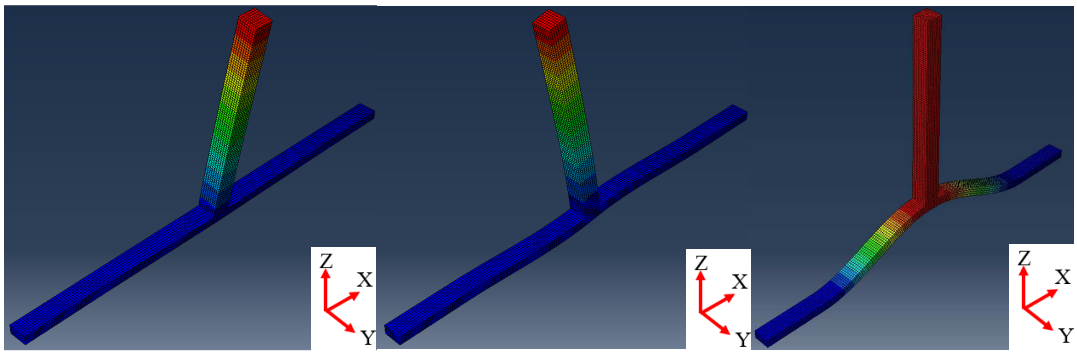

Sample 2 Mode Shapes:

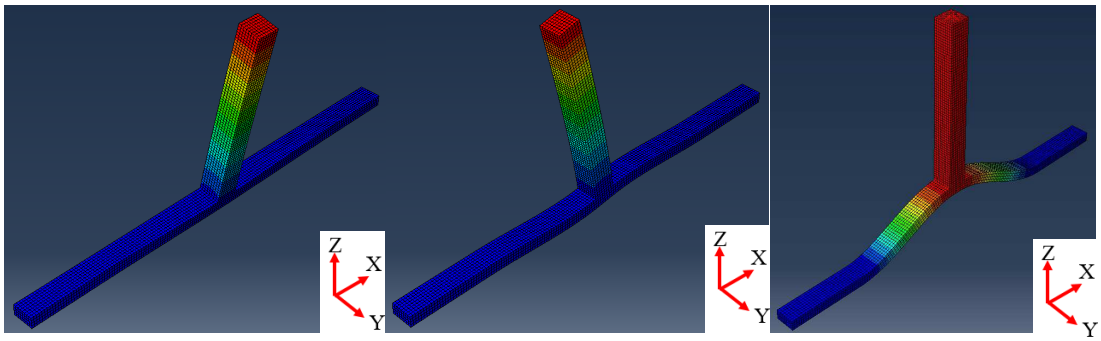

Sample 1 Mode Shapes:

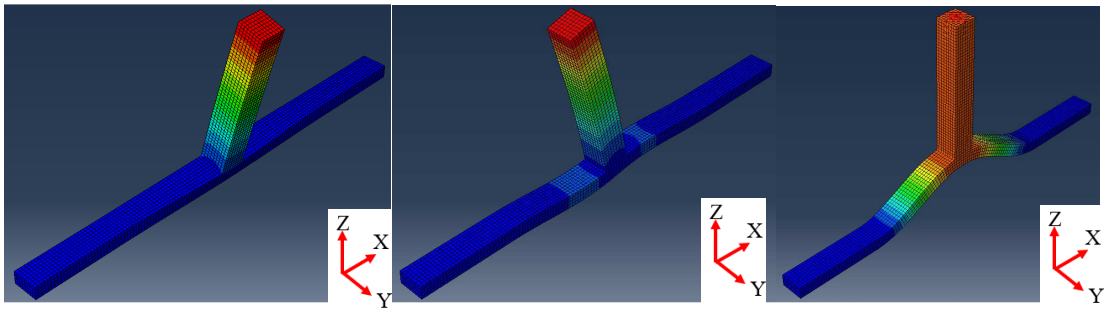

Appendix B: Sine Sweep Test Acceleration FFT Results:

Sample 1:

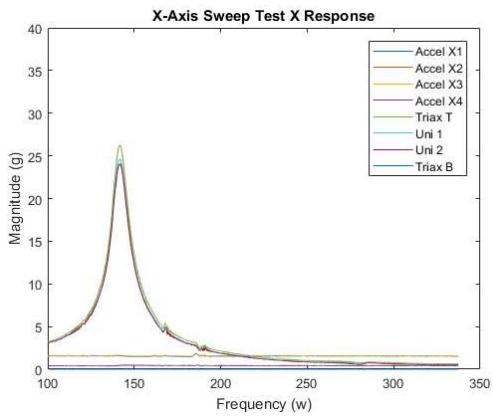

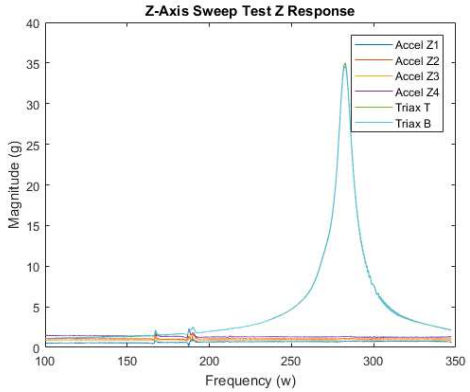

Sample 2:

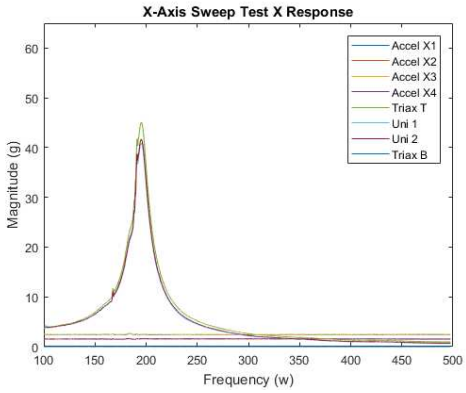

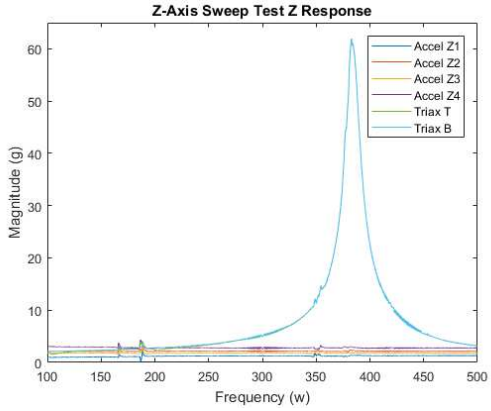

Sample 3:

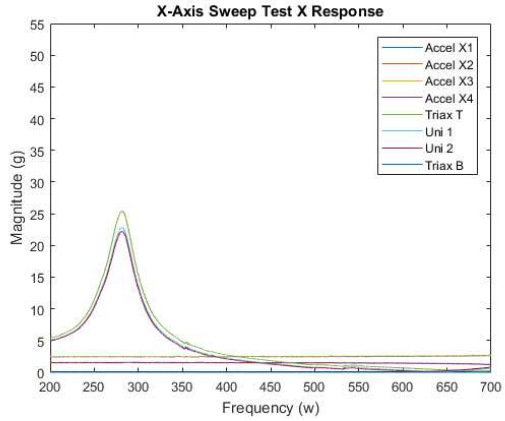

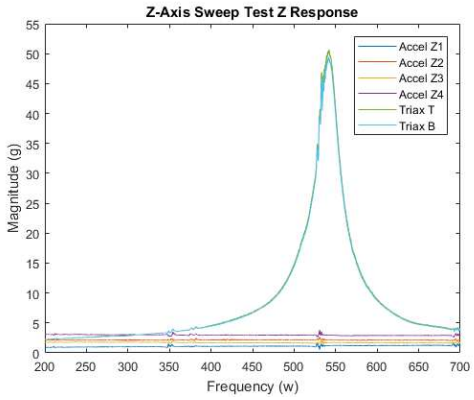

Sample 4:

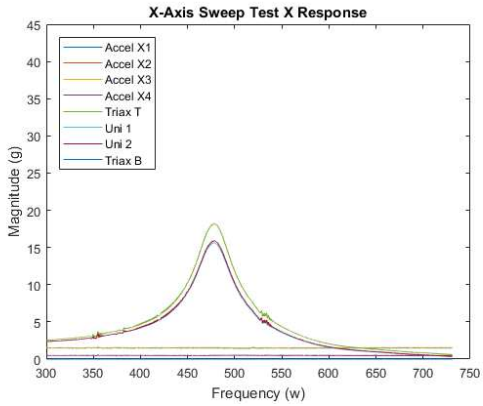

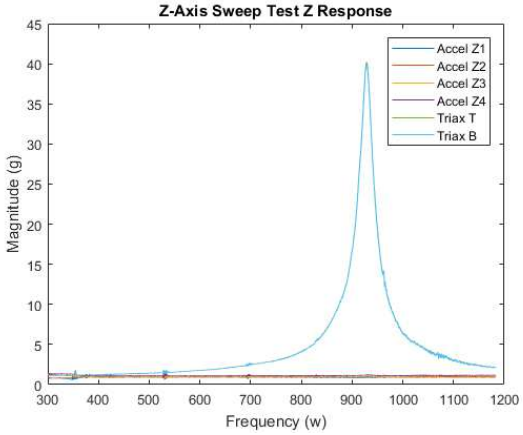

Sample 5:

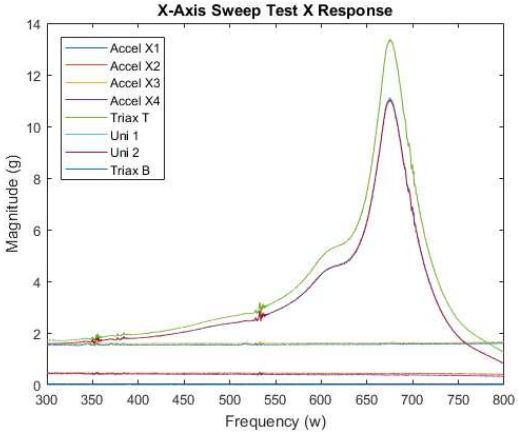

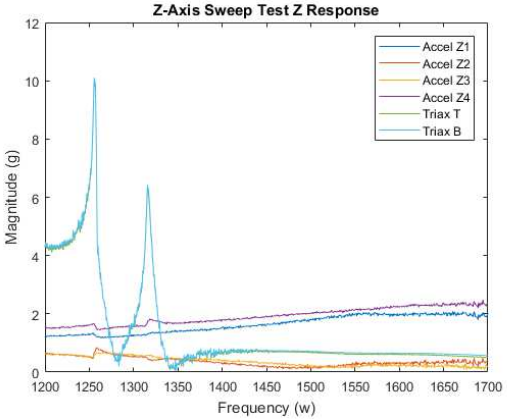

Appendix C: Broadband Random Excitation Test Acceleration FFT Results:

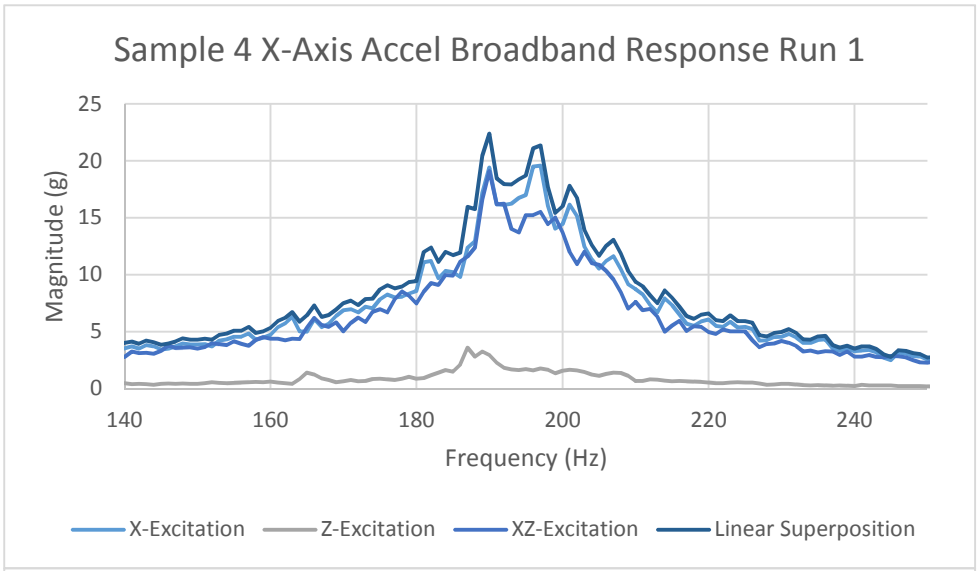

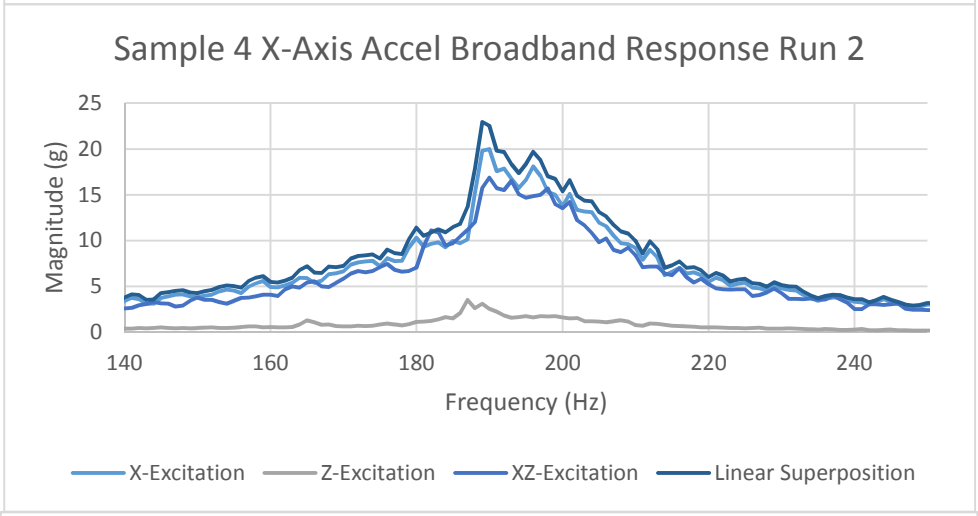

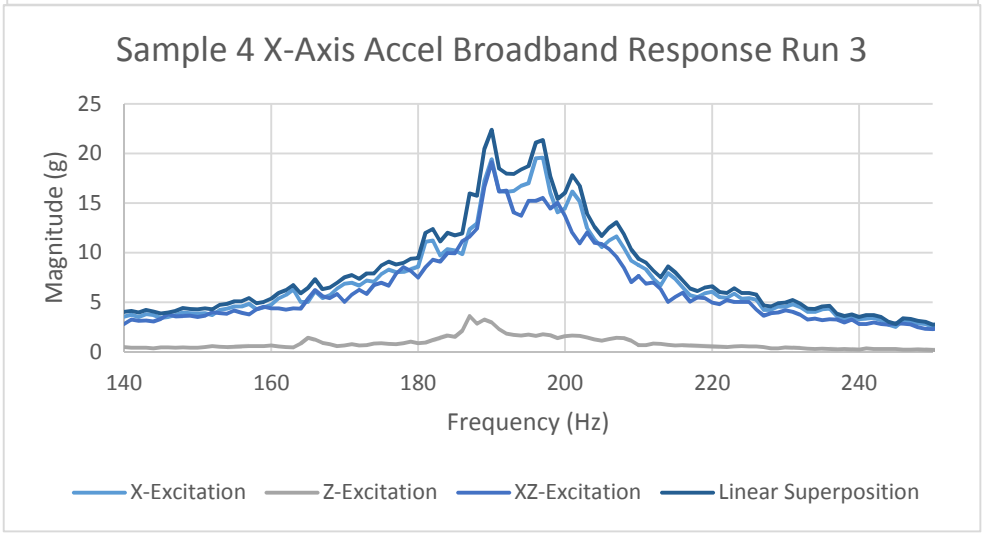

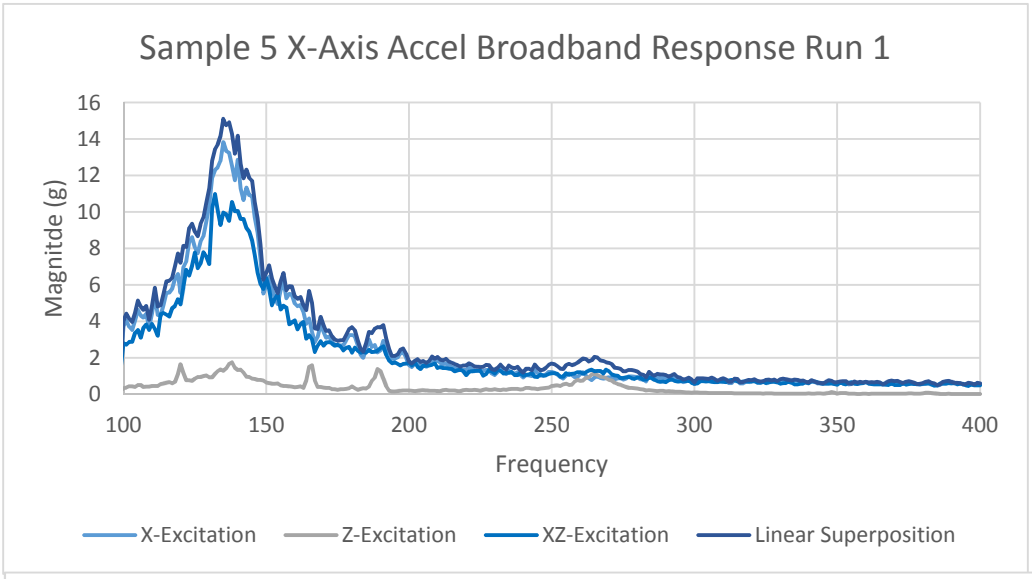
Sample 5 X-Axis Accel Broadband Response Run 1
Magnitde (g)
16
14
12
10
8
6
4
2
0
100
150
200
250
300
350
400
Frequency
X-Excitation
Z-Excitation
XZ-Excitation
Linear Superposition

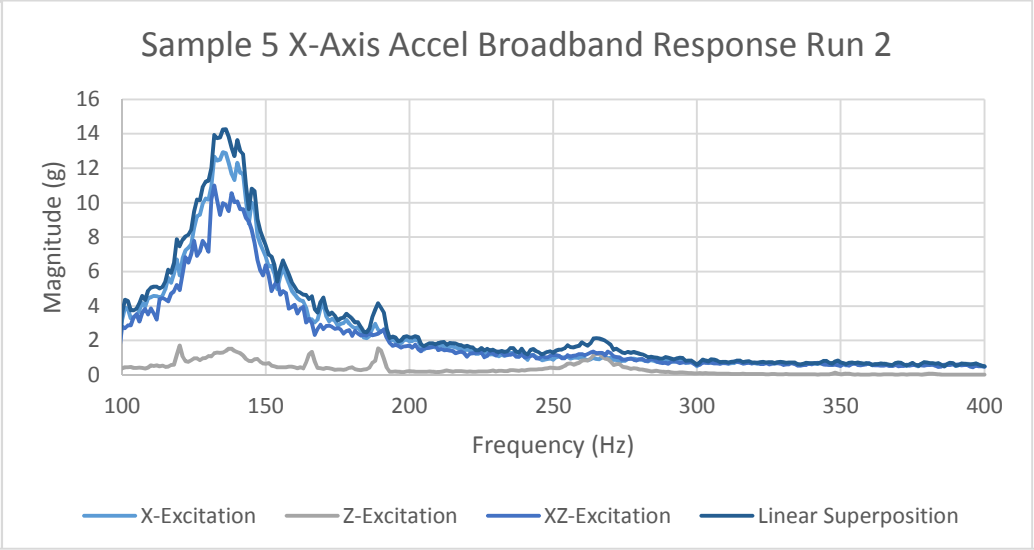
Sample 5 X-Axis Accel Broadband Response Run 2
Magnitude (g)
16
14
12
10
8
6
4
2
0
100
150
200
250
300
350
400
Frequency (Hz)
X-Excitation
Z-Excitation
XZ-Excitation
Linear Superposition

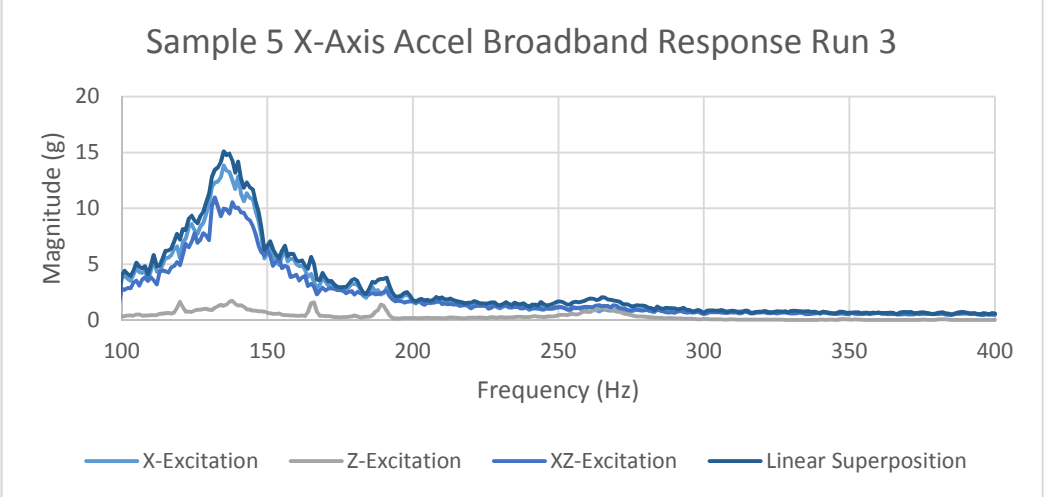
Sample 5 X-Axis Accel Broadband Response Run 3
Magnitude (g)
20
15
10
5
0
100
150
200
250
300
350
400
Frequency (Hz)
X-Excitation
Z-Excitation
XZ-Excitation
Linear Superposition

Appendix D: 6 Hz Bandwidth Random Excitation Test Acceleration FFT Results:

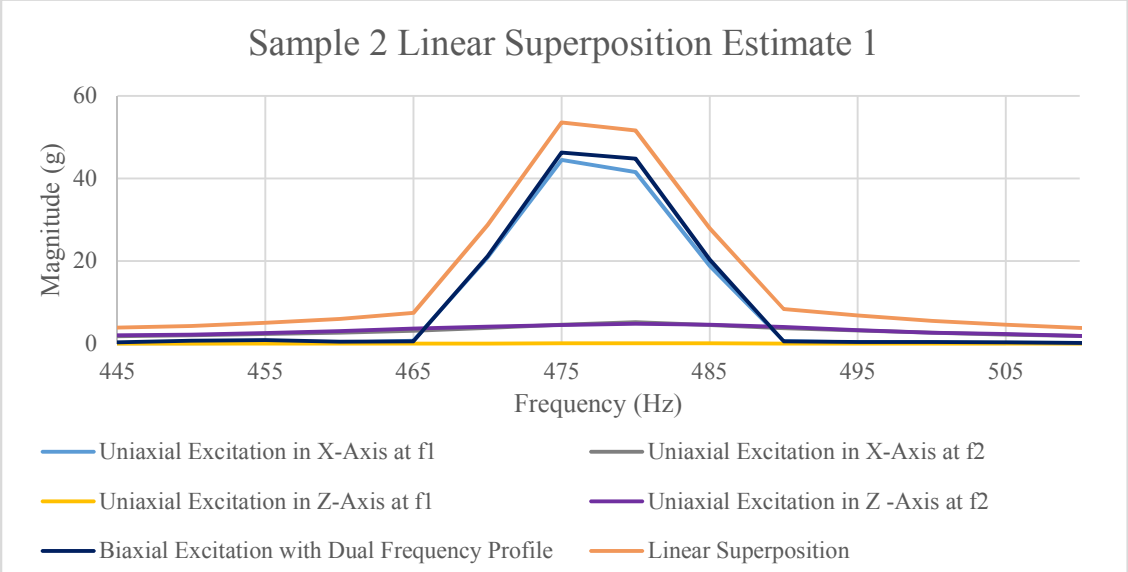

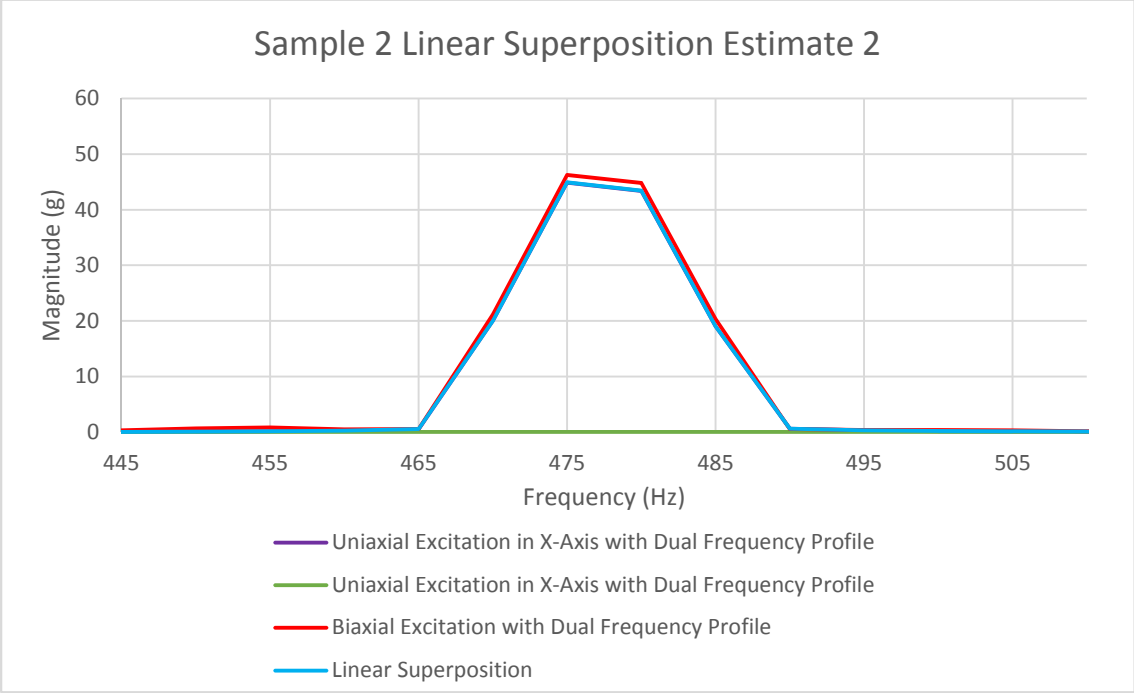

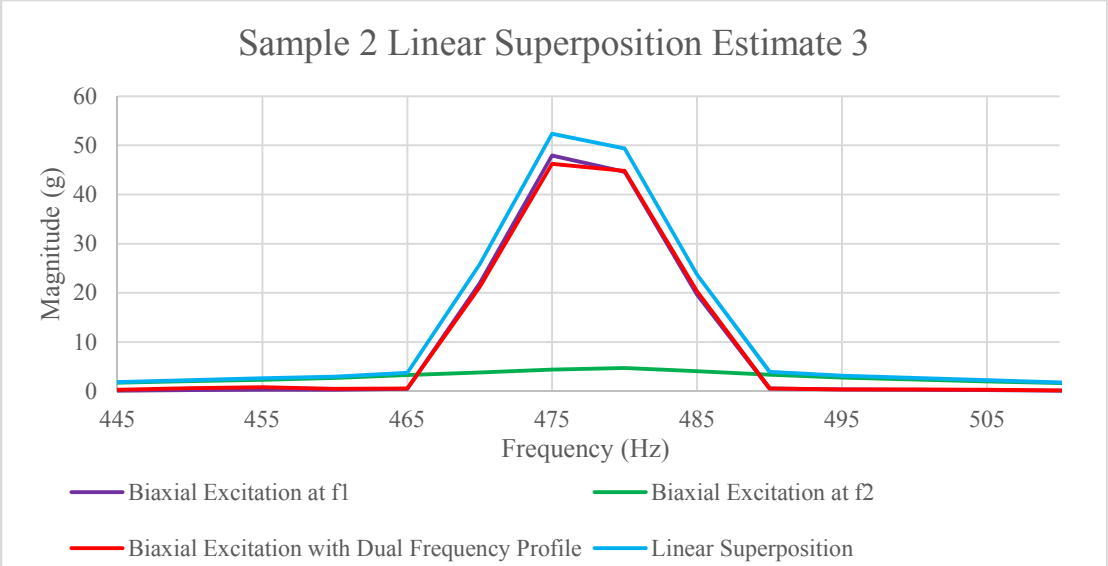
Sample 2 Linear Superposition Estimate 3
Magnitude (g)
60
50
40
30
20
10
0
445
455
465
475
485
495
505
Frequency (Hz)
Biaxial Excitation at f1
Biaxial Excitation at f2
Biaxial Excitation with Dual Frequency Profile
Linear Superposition

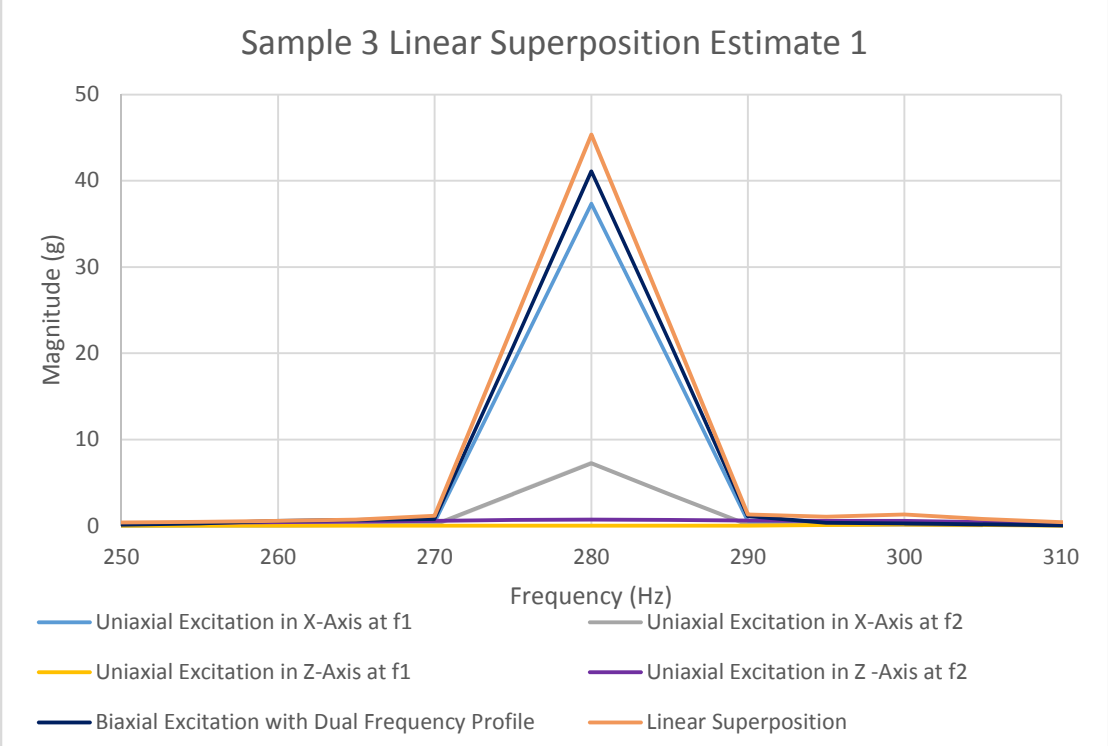
Sample 3 Linear Superposition Estimate 1
Magnitude (g)
50
40
30
20
10
0
250
260
270
280
290
300
310
Frequency (Hz)
Uniaxial Excitation in X-Axis at f1
Uniaxial Excitation in X-Axis at f2
Uniaxial Excitation in Z-Axis at f1
Uniaxial Excitation in Z -Axis at f2
Biaxial Excitation with Dual Frequency Profile
Linear Superposition

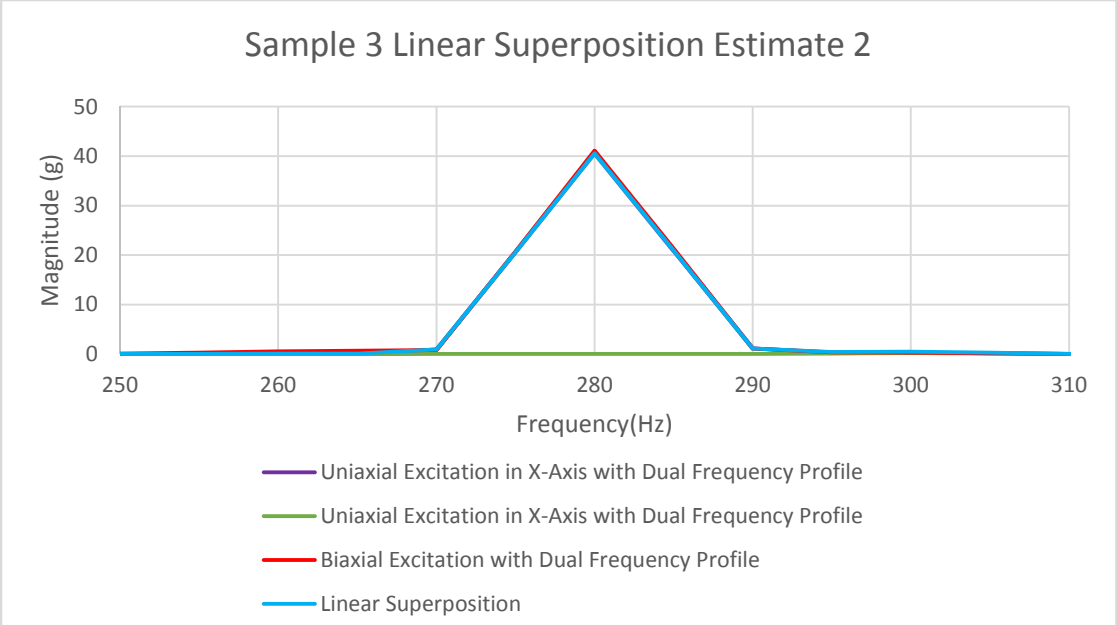
Sample 3 Linear Superposition Estimate 2
Magnitude (g)
50
40
30
20
10
0
250
260
270
280
290
300
310
Frequency(Hz)
Uniaxial Excitation in X-Axis with Dual Frequency Profile
Uniaxial Excitation in X-Axis with Dual Frequency Profile
Biaxial Excitation with Dual Frequency Profile
Linear Superposition

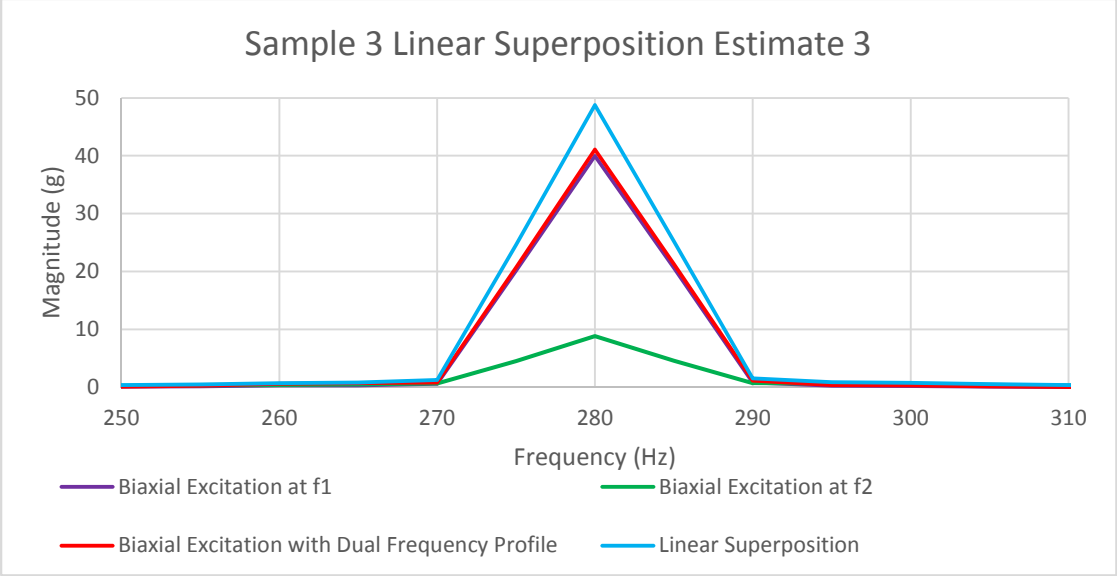
Sample 3 Linear Superposition Estimate 3
Magnitude (g)
50
40
30
20
10
0
250
260
270
280
290
300
310
Frequency (Hz)
Biaxial Excitation at f1
Biaxial Excitation at f2
Biaxial Excitation with Dual Frequency Profile
Linear Superposition

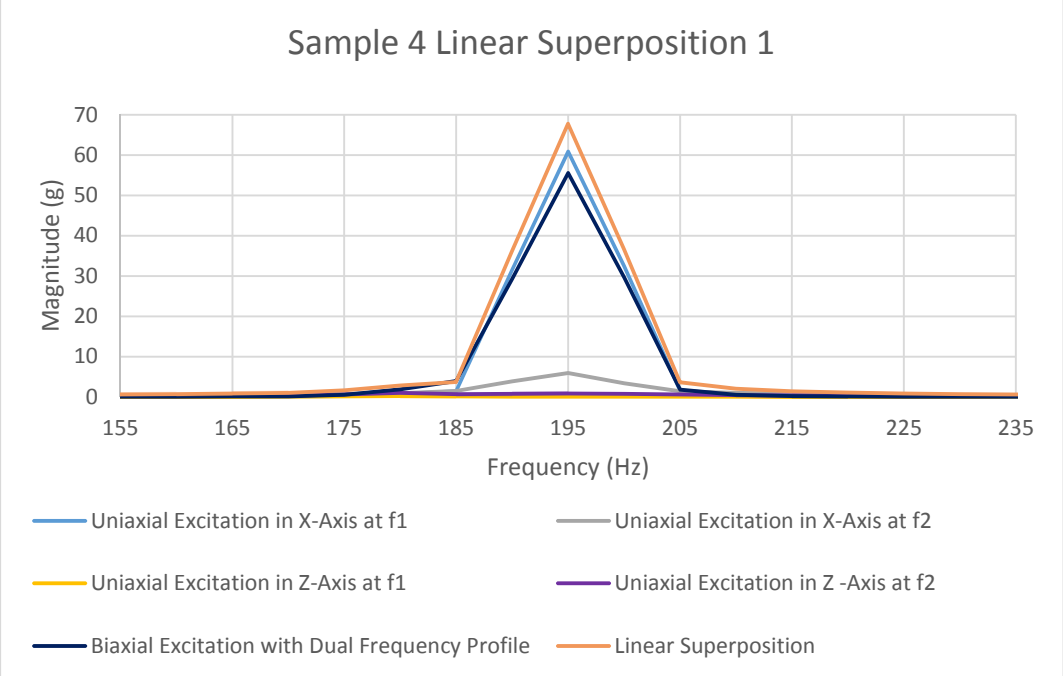
Sample 4 Linear Superposition 1
Magnitude (g)
70
60
50
40
30
20
10
0
155
165
175
185
195
205
215
225
235
Frequency (Hz)
Uniaxial Excitation in X-Axis at f1
Uniaxial Excitation in X-Axis at f2
Uniaxial Excitation in Z-Axis at f1
Uniaxial Excitation in Z -Axis at f2
Biaxial Excitation with Dual Frequency Profile
Linear Superposition

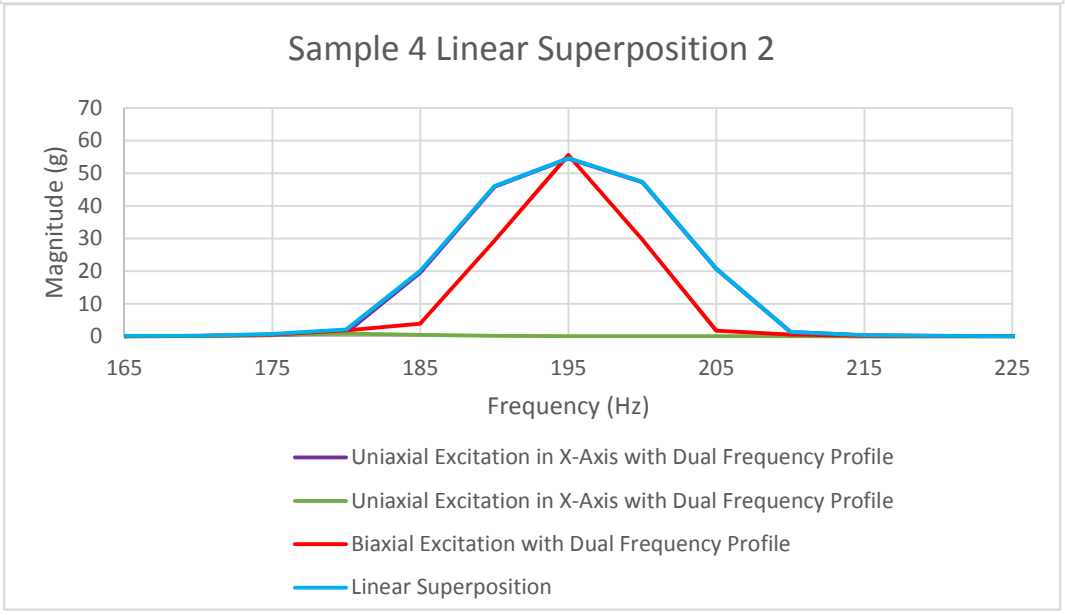
Sample 4 Linear Superposition 2
Magnitude (g)
70
60
50
40
30
20
10
0
165
175
185
195
205
215
225
Frequency (Hz)
Uniaxial Excitation in X-Axis with Dual Frequency Profile
Uniaxial Excitation in X-Axis with Dual Frequency Profile
Biaxial Excitation with Dual Frequency Profile
Linear Superposition

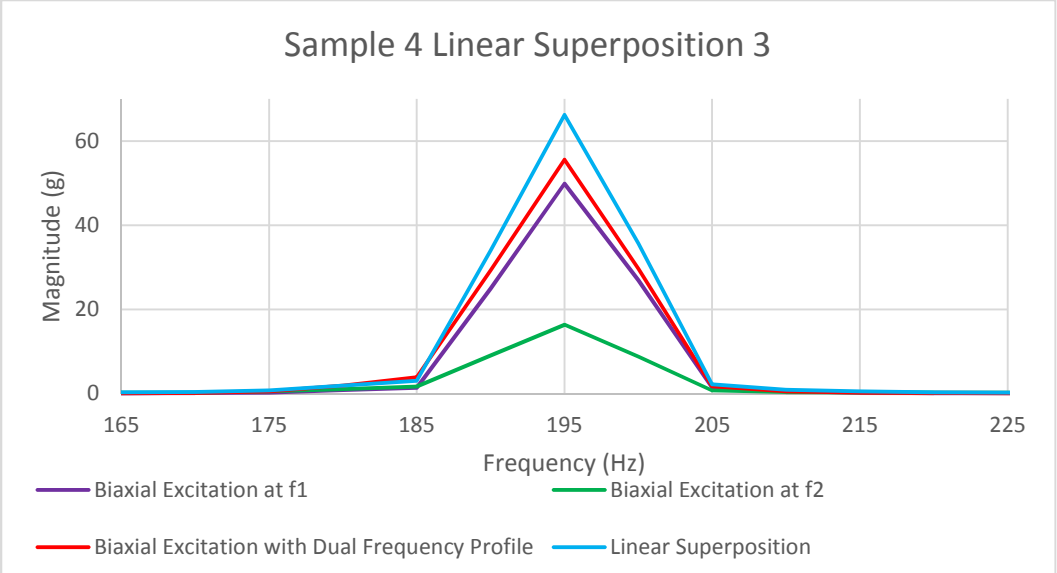
Sample 4 Linear Superposition 3
Magnitude (g)
60
40
20
0
165
175
185
195
205
215
225
Frequency (Hz)
Biaxial Excitation at f1
Biaxial Excitation at f2
Biaxial Excitation with Dual Frequency Profile
Linear Superposition

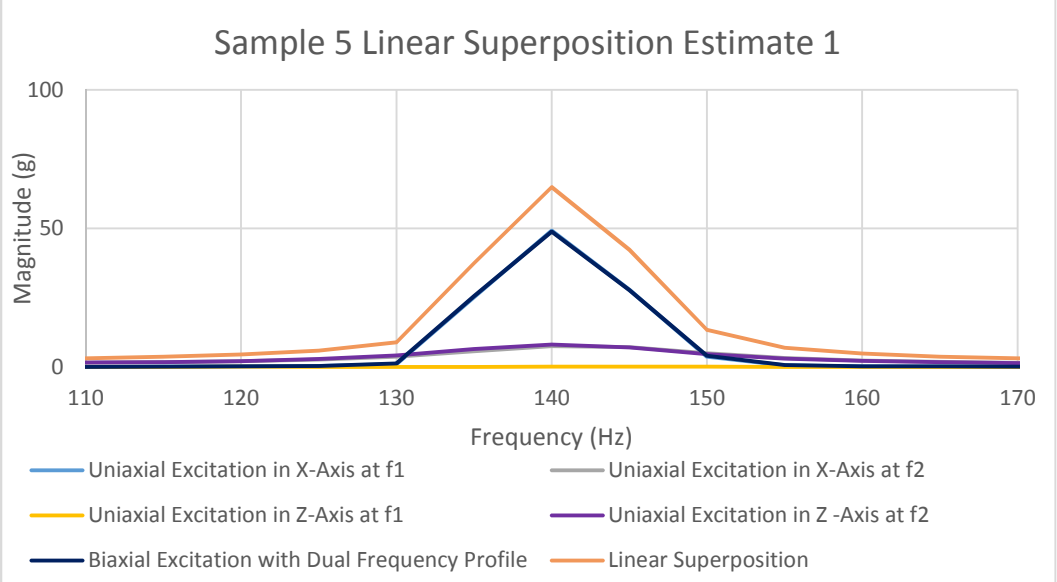
Sample 5 Linear Superposition Estimate 1
Magnitude (g)
100
50
0
110
120
130
140
150
160
170
Frequency (Hz)
Uniaxial Excitation in X-Axis at f1
Uniaxial Excitation in X-Axis at f2
Uniaxial Excitation in Z-Axis at f1
Uniaxial Excitation in Z -Axis at f2
Biaxial Excitation with Dual Frequency Profile
Linear Superposition

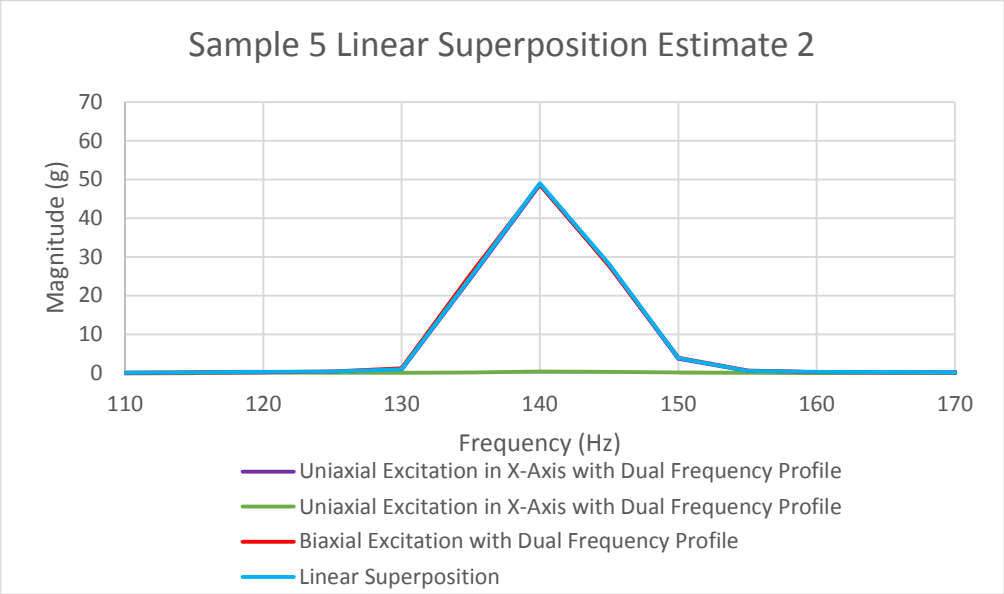
Sample 5 Linear Superposition Estimate 2
Magnitude (g)
70
60
50
40
30
20
10
0
110
120
130
140
150
160
170
Frequency (Hz)
Uniaxial Excitation in X-Axis with Dual Frequency Profile
Uniaxial Excitation in X-Axis with Dual Frequency Profile
Biaxial Excitation with Dual Frequency Profile
Linear Superposition

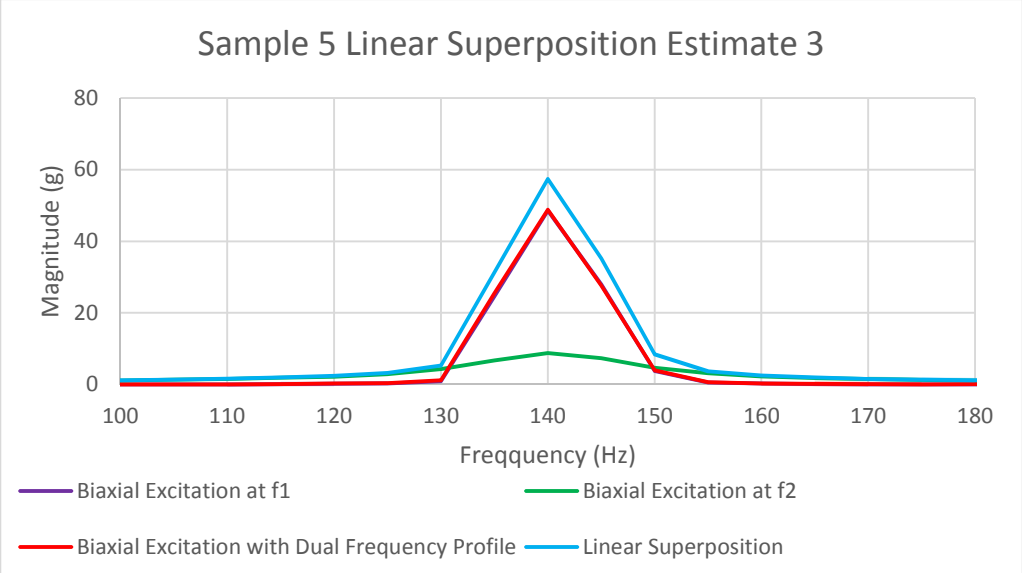
Sample 5 Linear Superposition Estimate 3
Magnitude (g)
80
60
40
20
0
100
110
120
130
140
150
160
170
180
Freqquency (Hz)
Biaxial Excitation at f1
Biaxial Excitation at f2
Biaxial Excitation with Dual Frequency Profile
Linear Superposition

Appendix E: 6 Hz Bandwidth Random Excitation Test Acceleration Global Normalized difference:

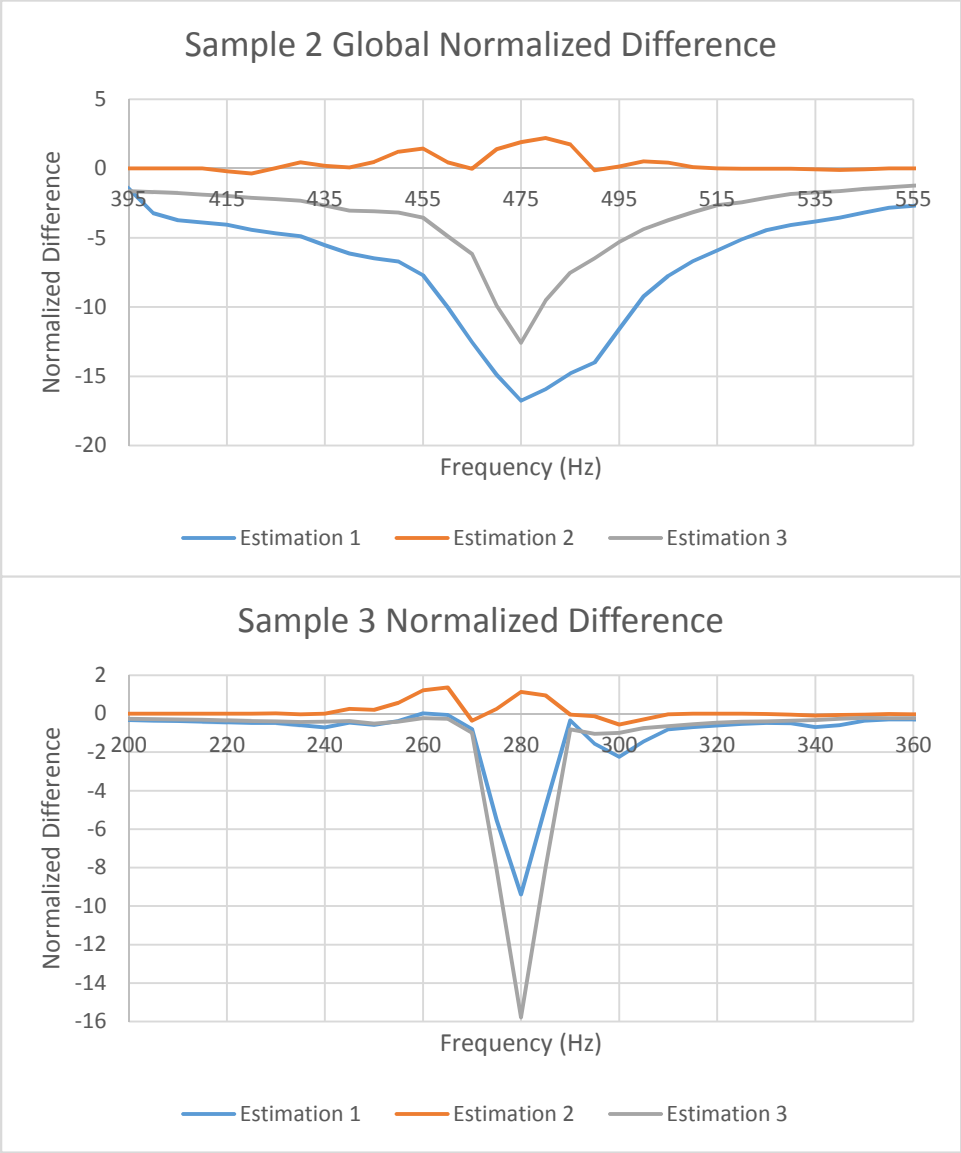

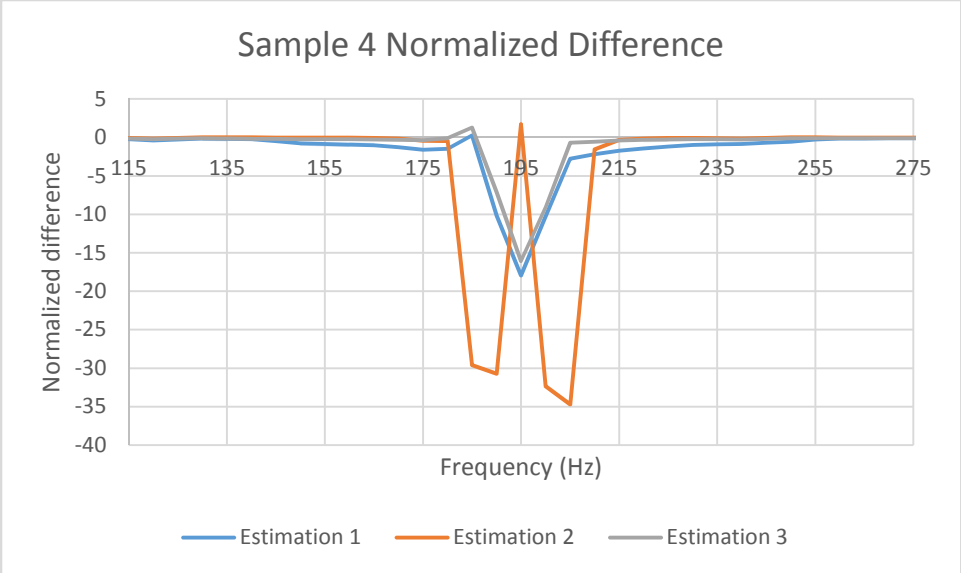
Sample 4 Normalized Difference
Normalized difference
5
0
-5
-10
-15
-20
-25
-30
-35
-40
115
135
155
175
195
215
235
255
275
Frequency (Hz)
Estimation 1
Estimation 2
Estimation 3

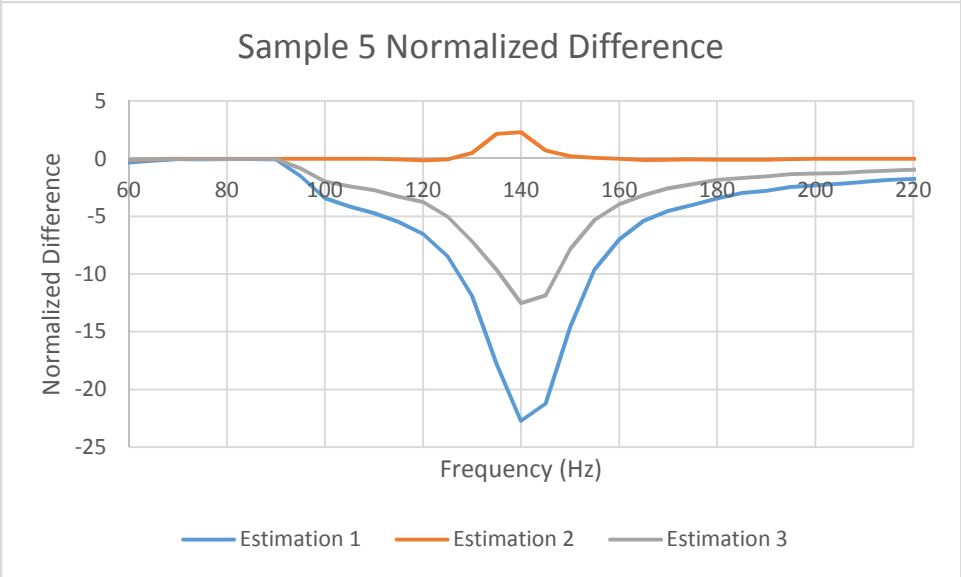
Sample 5 Normalized Difference
Normalized Difference
5
0
-5
-10
-15
-20
-25
60
80
100
120
140
160
180
200
220
Frequency (Hz)
Estimation 1
Estimation 2
Estimation 3

Appendix F: Matlab Code Excerpts

In this study, Matlab R2017a is used to post process the strain data as well as the data from the FEA simulations. As discussed in the paper, the strain data is post-processed under four different FFT resolutions. This is achieved by averaging the data in different sized data packets with around a 50% overlap. For .1 Hz resolution, the entire data is used. For .25 Hz resolution, the data is split into 10 data packets of 20,000 samples each. Below shows an excerpt of the Matlab code for both .1 and .25 Hz resolution for the first run of the broadband random excitation test uniaxially in the X-Axis.

```
%% FX Beam 2 Run 1
filename1 = 'R5_BB_RX_FX_Beam2_Run1.xlsx';

Time_X_R1 = xlsread(filename1);     %Load Data File

% FFT
Ts = Time_X_R1(4,1)-Time_X_R1(3,1);
fs = 1/Ts;                          %Sampling Frequency of Data

FFT_X_R1 =
fft(hanning(length(Time_X_R1(1:87500,2))).*Time_X_R1(1:87500,2));
l_X_R1 = length(FFT_X_R1);
f_X_R1 = (-l_X_R1/2:l_X_R1/2-1)/l_X_R1*fs;
phs_X_R1 = angle(fftshift(FFT_X_R1));
P2_X_R1 = abs(FFT_X_R1/l_X_R1);
P1_X_R1 = P2_X_R1(1:l_X_R1/2+1);
P1_X_R1(2:end-1) = 2*P1_X_R1(2:end-1);
f_X_R1 = fs*(0:(l_X_R1/2))/l_X_R1; %FFT .1 Hz Resolution

figure;
plot(f_X_R1,P1_X_R1)
xlabel 'Frequency (Hz)'
ylabel '|y|'

% FFT Chunks
FFT_X_R1_1   =
fft(hanning(length(Time_X_R1(    1:20000,2))).*Time_X_R1(    1:20000
,2));
FFT_X_R1_2   =
fft(hanning(length(Time_X_R1( 7501:27500,2))).*Time_X_R1( 7501:27500
,2));
```

```
FFT_X_R1_3   =
fft(hanning(length(Time_X_R1(15001:35000,2))).*Time_X_R1(15001:35000
,2));
FFT_X_R1_4   =
fft(hanning(length(Time_X_R1(22501:42500,2))).*Time_X_R1(22501:42500
,2));
FFT_X_R1_5   =
fft(hanning(length(Time_X_R1(30001:50000,2))).*Time_X_R1(30001:50000
,2));
FFT_X_R1_6   =
fft(hanning(length(Time_X_R1(37501:57500,2))).*Time_X_R1(37501:57500
,2));
FFT_X_R1_7   =
fft(hanning(length(Time_X_R1(45001:65000,2))).*Time_X_R1(45001:65000
,2));
FFT_X_R1_8   =
fft(hanning(length(Time_X_R1(52501:72500,2))).*Time_X_R1(52501:72500
,2));
FFT_X_R1_9   =
fft(hanning(length(Time_X_R1(60001:80000,2))).*Time_X_R1(60001:80000
,2));
FFT_X_R1_10   =
fft(hanning(length(Time_X_R1(67501:87500,2))).*Time_X_R1(67501:87500
,2));

FFT_X_R1_Average_1 = (FFT_X_R1_1 + FFT_X_R1_2 + FFT_X_R1_3 +
FFT_X_R1_4 + FFT_X_R1_5 + FFT_X_R1_6 + FFT_X_R1_7 + FFT_X_R1_8 +
FFT_X_R1_9 + FFT_X_R1_10)./10;

l_X_R1_1 = length(FFT_X_R1_Average_1);
f_X_R1_1 = (-l_X_R1_1/2:l_X_R1_1/2-1)/l_X_R1_1*fs;
phs_X_R1_1 = angle(fftshift(FFT_X_R1_Average_1));
P2_X_R1_1 = abs(FFT_X_R1_Average_1/l_X_R1_1);
FFT_X_R1_Average = P2_X_R1_1(1:l_X_R1_1/2+1); %FFT .25 Hz Resolution
FFT_X_R1_Average(2:end-1) = 2*FFT_X_R1_Average(2:end-1);
f_X_R1_1 = fs*(0:(l_X_R1_1/2))/l_X_R1_1;
```

Code Excerpt 1: FFT Creation

Now, a very similar code is used for .5 and 1 Hz FFT resolution, but with additional lines in the data chunks section with smaller data packet sizes. For .5 Hz resolution, 16 data packets of 10,000 samples are used, and for the 1 Hz resolution 34 data packets of 5,000 samples are used.

After the FFTs of various resolutions are created for each run of each individual test, the three replicates are averaged together, using the code seen below.

Note that the following code is the average of the three replicates for the X-Axis uniaxial test under broadband random excitation.

```
%% X-Excitation Average 0f Runs

% FFT .1 Hz Resolution

f_X = (f_X_R1 + f_X_R2 + f_X_R3) / 3;
P1_X = (P1_X_R1 + P1_X_R2 + P1_X_R3) / 3;

figure;
plot(f_X,P1_X)
xlabel 'Frequency (Hz)'
ylabel '|y|'

% FFT Chunks .25 Hz Resolution

f_X_average = f_X_R3_1;
FFT_X_Average = (FFT_X_R1_Average + FFT_X_R2_Average +
FFT_X_R3_Average) ./3;
```

Code Excerpt 2: Averaging of Replicates

Now, the important thing to realize about any averaging on Matlab is that the size of the averaged arrays needs to be the exact same. Once this code is completed, a single signal has been created for the X-Axis broadband excitation test. The next thing that occurs in the code is to repeat Code Excerpt 1 for the three replicates for the Z-Axis and biaxial tests followed by Code Excerpt 2 to average the replicates into a single signal.

By this point, there are three individual signals for the three tests in the test matrix. The final step is to create a normalized difference of the signals and plot the result. This is achieved first by creating a linear superposition signal by adding the signals from the two uniaxial tests. After this is done, Equation 4-1 is used to find the normalized difference between the linear superposition and biaxial test response.

```
%% Superposition

FFT_SP_Average = FFT_X_Average + FFT_Z_Average;
P1_SP = P1_X + P1_Z;

figure;
plot(f_XZ,P1_X)
hold on
plot(f_XZ,P1_Z)
plot(f_XZ,P1_XZ)
plot(f_XZ,P1_SP)
xlabel 'Frequency (Hz)'
ylabel '|y|'
legend('X-Excitation','Z-Excitation','XZ-Excitation','Linear
Superposition')

figure;
plot(f_XZ_average,FFT_X_Average)
hold on
plot(f_XZ_average,FFT_Z_Average)
plot(f_XZ_average,FFT_XZ_Average)
plot(f_XZ_average,FFT_SP_Average)
xlabel 'Frequency (Hz)'
ylabel '|y|'
legend('X-Excitation','Z-Excitation','XZ-Excitation','Linear
Superposition')

% Normalized Difference

Diff_1 = FFT_XZ_Average -FFT_SP_Average;
Diff_2 = P1_XZ -P1_SP;
Perc_Diff_1 = Diff_1 ./ max(FFT_SP_Average).*100;
Perc_Diff_2 = Diff_2 ./ max(P1_SP).*100;

figure;
plot(f_XZ_average,Perc_Diff_1)
title('Percent Difference S4 .25 hz res')
xlabel 'Frequency (Hz)'
ylabel '|y|'
xlim([100 1000])

figure;
plot(f_XZ,Perc_Diff_2)
title('Percent Difference S4 .1 hz res')
xlabel 'Frequency (Hz)'
ylabel '|y|'
xlim([100 1000])
```

Code Excerpt 3: Normalized Difference

By using the three code excerpts, the post processing of all of the experimental and simulated data was achieved. The only difference between the

experimental and simulation post-processing is the amount of samples in the FFT, and the lack of data packets to be averaged. The size of the data packet is smaller, because only 1 second worth of data is run in the implicit dynamic simulation versus the 30 seconds run in the experimental test. There are no additional data packets being averaged together, because the finest FFT resolution is needed from the FEA data to achieve a resolution of 1 Hz. If data packets were used, then the FFT resolution would be even more coarse then the most coarse FFT resolution from the experimental data.

Appendix G: 1 Hz Excitation SOP

1. Turn on Abacus Controller:
    a. There will be a two short beeps followed by to long beeps in around 30 seconds. The Signal Star software cannot be opened until the two long beeps have been signaled
2. Open Signal Star:
    a. There will be a menu bar that will open showing that it is connecting to the controller. After it is successful, the bar will close.
3. Open Multiaxial Random Excitation Test:
    a. Open or create a file that is for random excitation in multiple axes. The file name will be a .rvn file

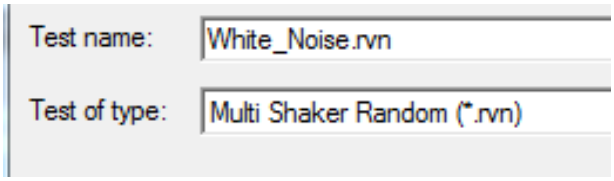

Figure G-1: Open File

4. Setup – Test:

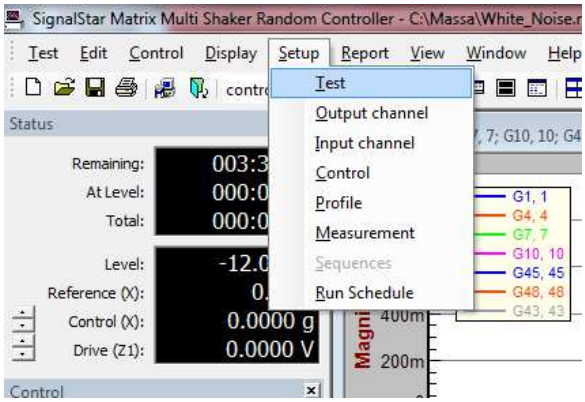

Figure G-2: Setup Test

a. Under setup test, this study used an input transformation matrix to relate the individual actuators to an output purely based on the 6 independent degrees of freedom. There exists other SOPs to describe how to setup an input transformation matrix. This SOP will focus on how to setup the test so that a 1 Hz bandwidth excitation profile can be used in multiple axes

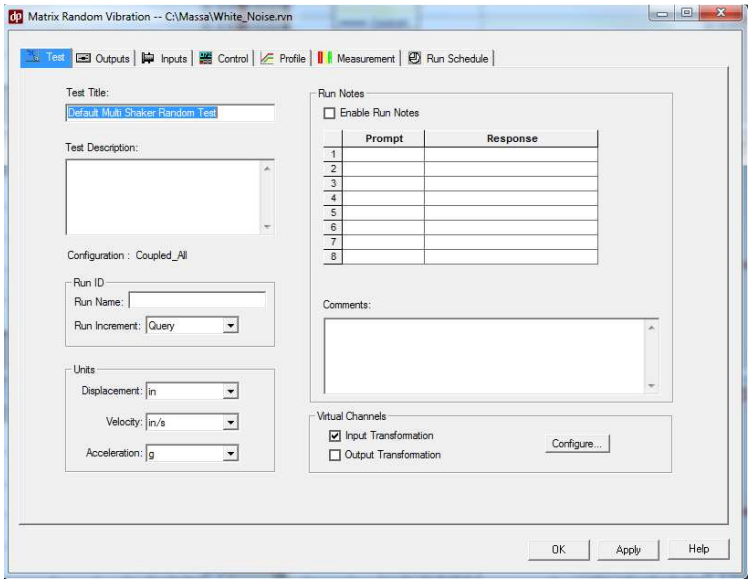

Figure G-3: Test Tab

5. Output Tab

a. Under the Output Tab, the first thing that needs to be done is setting up the configuration. The configuration should be set to Coupled_All. This allows for all of the actuators to be able to be used. In addition, under Edit in the configuration section, select Uncoupled Mode. This allows for the profiles to not have cross dependence, but also allows all actuators to be used in the test.

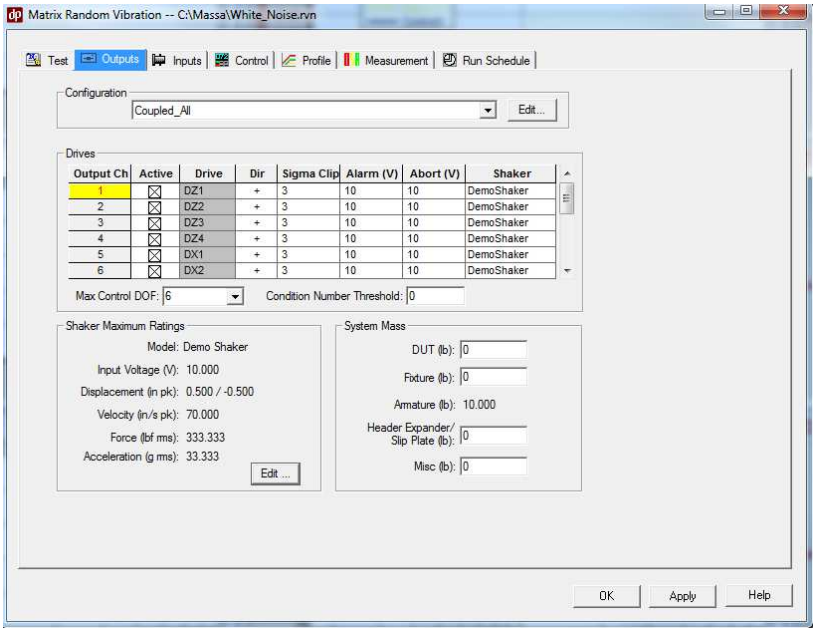

Figure G-4: Outputs Tab

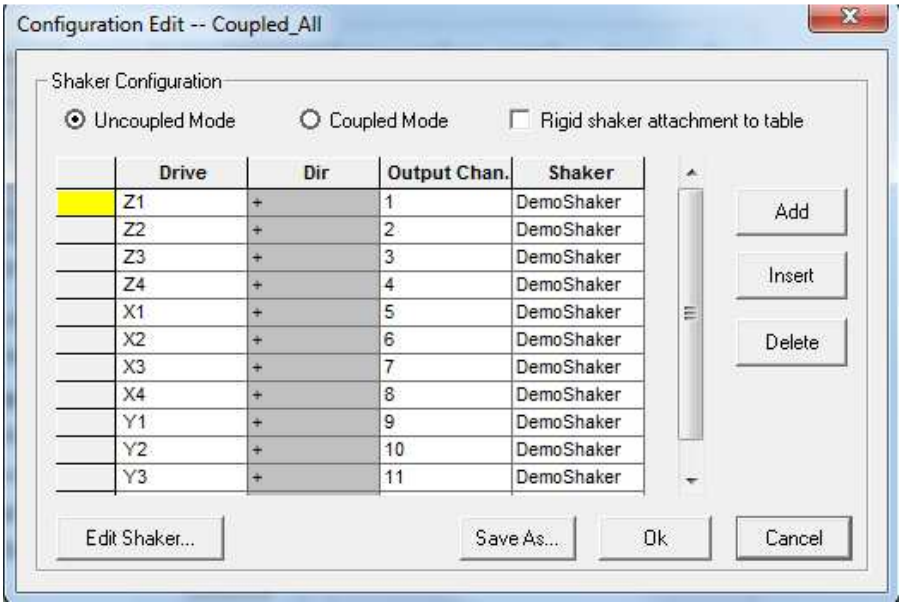

Figure G-5: Edit Configuration

b. Under the Drives section of the Outputs Tab, select all 12 actuators to be Active. In addition, set the Max Control DOF to 6. Since the configuration allowed all of the actuators to be used, this activates the actuators so that all of them are used in the test.

6. Inputs Tab

    a. Under the Inputs Tab, all of the measured quantities are listed. At the bottom of the list are the channels from the transformation matrix. Set the channels that will be controlled in this test to control. This sets the measurement that will be used in the control feedback of the shaker table to fit the vibration profile.

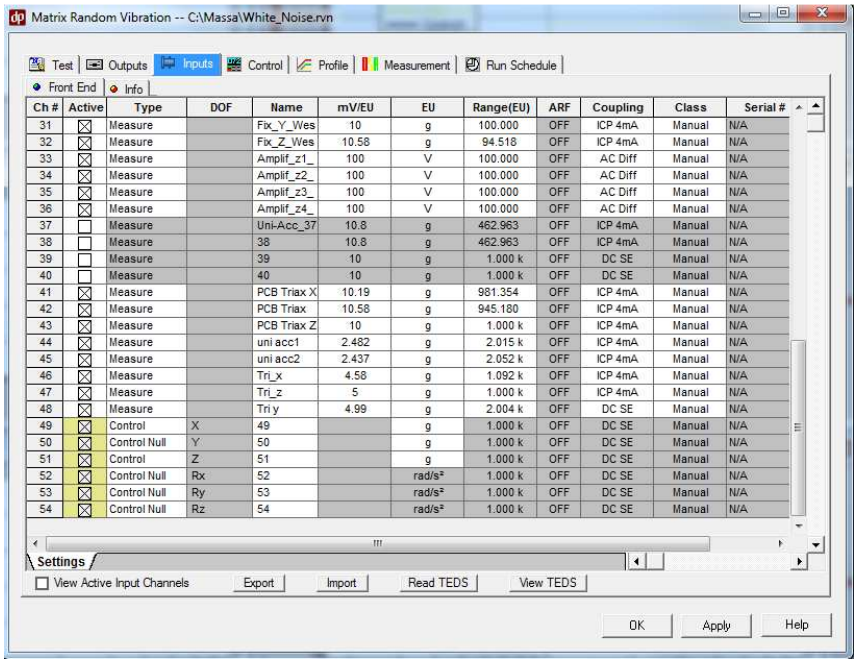

Ch #	Active	Type	DOF	Name	mV/EU	EU	Range(EU)	ARF	Coupling	Class	Serial #
31	☒	Measure		Fix_Y_Wes	10	g	100.000	OFF	ICP 4mA	Manual	N/A
32	☒	Measure		Fix_Z_Wes	10.58	g	94.518	OFF	ICP 4mA	Manual	N/A
33	☒	Measure		Amplif_z1_	100	V	100.000	OFF	AC Diff	Manual	N/A
34	☒	Measure		Amplif_z2_	100	V	100.000	OFF	AC Diff	Manual	N/A
35	☒	Measure		Amplif_z3_	100	V	100.000	OFF	AC Diff	Manual	N/A
36	☒	Measure		Amplif_z4_	100	V	100.000	OFF	AC Diff	Manual	N/A
37	☐	Measure		Uni-Acc_37	10.8	g	462.963	OFF	ICP 4mA	Manual	N/A
38	☐	Measure		38	10.8	g	462.963	OFF	ICP 4mA	Manual	N/A
39	☐	Measure		39	10	g	1.000 k	OFF	DC SE	Manual	N/A
40	☐	Measure		40	10	g	1.000 k	OFF	DC SE	Manual	N/A
41	☒	Measure		PCB Triax X	10.19	g	981.354	OFF	ICP 4mA	Manual	N/A
42	☒	Measure		PCB Triax	10.58	g	945.180	OFF	ICP 4mA	Manual	N/A
43	☒	Measure		PCB Triax Z	10	g	1.000 k	OFF	ICP 4mA	Manual	N/A
44	☒	Measure		uni acc1	2.482	g	2.015 k	OFF	ICP 4mA	Manual	N/A
45	☒	Measure		uni acc2	2.437	g	2.052 k	OFF	ICP 4mA	Manual	N/A
46	☒	Measure		Tri_x	4.58	g	1.092 k	OFF	ICP 4mA	Manual	N/A
47	☒	Measure		Tri_z	5	g	1.000 k	OFF	ICP 4mA	Manual	N/A
48	☒	Measure		Tri y	4.99	g	2.004 k	OFF	DC SE	Manual	N/A
49	☒	Control	X	49		g	1.000 k	OFF	DC SE	Manual	N/A
50	☒	Control Null	Y	50		g	1.000 k	OFF	DC SE	Manual	N/A
51	☒	Control	Z	51		g	1.000 k	OFF	DC SE	Manual	N/A
52	☒	Control Null	Rx	52		rad/s²	1.000 k	OFF	DC SE	Manual	N/A
53	☒	Control Null	Ry	53		rad/s²	1.000 k	OFF	DC SE	Manual	N/A
54	☒	Control Null	Rz	54		rad/s²	1.000 k	OFF	DC SE	Manual	N/A

Figure G-6: Inputs Tab

7. Control Tab

    a. Under the Control Tab, make sure that the bandwidth frequency is the exact same number as the frequency lines number. This limits the frequency bins of the profile to 1 Hz.

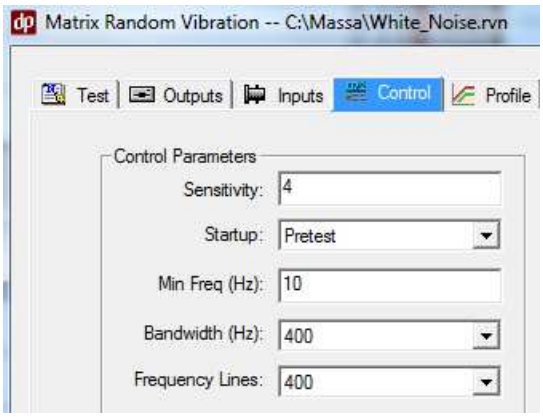

Figure G-7: Control Tab

8. Profile Tab

    a. In this Tab, the vibration profiles are set. There are two things to notice. The first is that only the diagonal terms are required for testing, because of what was done in the Outputs Tab. The second thing to notice is that the profiles are limited to the bandwidth frequency set in the Control Tab.

    b. To create a profile, select a diagonal term and select Edit in the profile box. Use the lines to set the levels of the profile. In the example given below, the range of all of the profiles was 100 to 300 Hz. Therefore, the first two and last two lines have a range when the output is 0. The third and fourth line set the bandwidth of the excitation profile to 1 Hz, which conforms to the frequency bin size set in the Control Tab. In addition, notice that .5 Hz is given as a ramp up and ramp down in between lines 2 and 3, and also between 4 and 5. The last thing to set is the acceleration RMS value for the profile. In this case, 5.5 g rms is used.

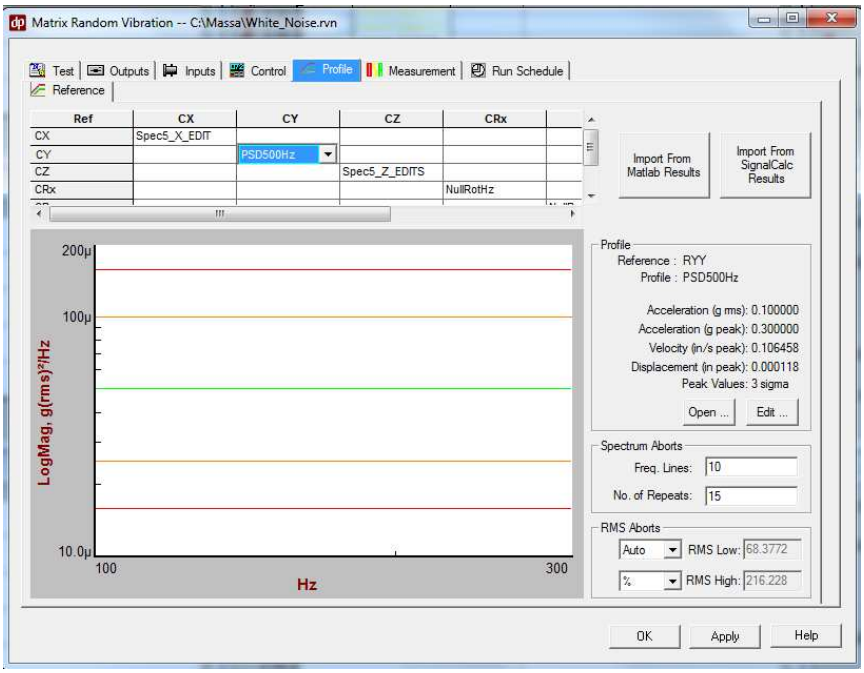

Figure G-8: Profile Tab

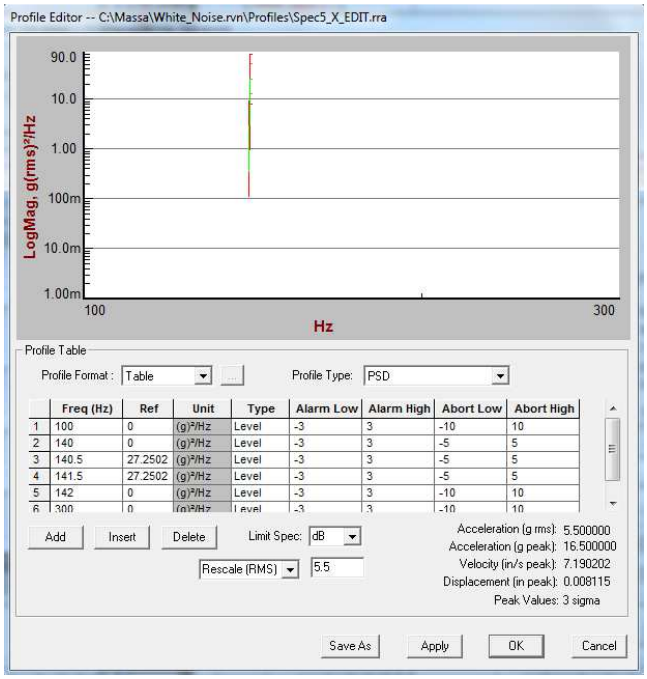

Figure G-9: Profile Edit

c. Just as the profile from Figure G-9 was set to 141 Hz, the profiles for additional directions can be set to other frequency magnitudes. In this study, the Z-Axis is set to 242 Hz. The only thing to reiterate is that the range of the frequencies of ALL profiles needs to be the same and be within the range set in the Control Tab.

9. Measurement Tab

a. Make sure that the Measurement Parameters shown are the same bandwidth and frequency lines set in the control tab. In addition, make sure that they are the same value for the same reason as in the Control Tab.

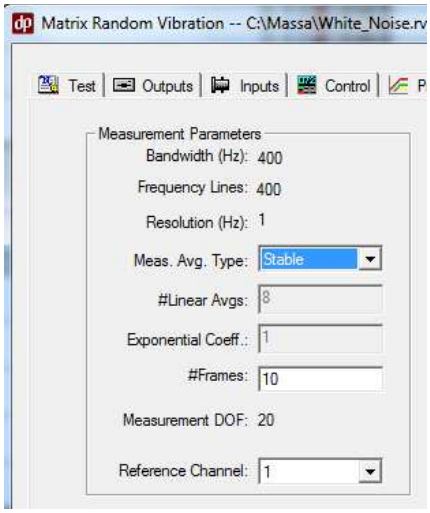

Figure G-10: Measurement Tab

10. Run Schedule Tab

a. Set the Run Schedule for the ramp up to the full vibration profile. At this point, the multiaxial 1 Hz bandwidth has been created and can be run.

Bibliography

[1] Aykan, M., and Çelik, M., *Vibration fatigue analysis and multi-axial effect in testing of aerospace structures.* Mechanical Systems and Signal Processing, vol. 23, pp. 897-907, 2009.

[2] Balachandran, B., and Edward B. Magrab. *Vibrations*. Toronto (Ont.): Cengage Learning, 2009. Print.

[3] Chen, C. *Linear systems theory and design*. New York: Holt-Saunders, 1984. Print.

[4] Choi, C., Al Bassyiouni, M., Dasgupta, A. and Osterman, M., *PoF Issues in Multi-DoF Vibration Testing: ED Shakers and RS Shakers,* in IEEE ASTR09 Workshop, NJ, October 2009.

[5] Delserro Engineering Solutions. *Mixed Mode: Sine on Random Vibration Testing, RoR, SoRoR*. July 2015.

[6] Ernst, M., Habtour, E., and Dasgupta, A. *Examining Steinberg's Octave Rule Applicability for Electronic Systems Exposed to Multiaxial Vibration*. IEEE Transactions on Components Packaging and Manufacturing Technology, 2016.

[7] French, R., Handy, R. and Cooper, H.L., *A Comparison of Simultaneous and Sequential Single-Axis Durability Testing.* Experimental Techniques, pp. 1-6, September-October 2006.

[8] Friedland, B.. *Control system design: an introduction to state-space methods*. Mineola, NY: Dover, 2005. Print.

[9] Gregory, D., Bitsie, F., and Smallwood, D. *Comparison of the Response of a Simple Structure to Single Axis and Multiple Axis Random Vibration Inputs*. 2009.

[10] Habtour, E., Drake, G.S, Dasgupta, A., Al-Bassyiouni, M. and Choi, C., *Improved Reliability Testing with Multiaxial Electrodynamics Vibration* Proceedings of the Annual Reliability and Maintainability Symposium, Jan. 2010.

[11] Habtour, E., Choi, C., Osterman, M. and Dasgupta, A., *Novel Approach to Improve Electronics Reliability in the Next Generation of US Army Small Unmanned Ground Vehicles Under Complex Vibration Conditions*. Journal of Failure Analysis and Prevention, pp. 86-95, 2012.

[12] Himelblau, H., et all. *Effects of triaxial and uniaxial random excitation on the vibration response and fatigue damage of typical spacecraft hardware.* Proc. 66th Shock and Vibration Symposium, Arlingtion, VA, October 1995

[13] *IEEE 344*. Institute of Electrical and Electronics Engineers (IEEE). PDF. 2013.

[14] Kumar, V., Miller, J., and Rhoads, J. *Nonlinear parametric amplification and attenuation in a base-excited cantilever beam* Journal of Sound and Vibration. 28, June 2011. Online.

[15] McConnell, Kenneth G.. *Vibration Testing: Theory and Practice.* John Wiley and Sons, Inc. NY, 1995. Print.

[16] *MIL-STD-810G*, Department of Defense Test Method Standard for Environmental Engineering Considerations and Laboratory Tests. PDF. United States Department of Defense. 31 Oct 2008.

[17] Sridharan, R., Dasgupta, A., Habtour, E., Choi, C. *Resilience of Large Electronic Components Undergoing Multi-Axial Vibratory Excitation*. Proceedings of the ASME 2015 International Technical Conference and Exhibition on Packaging and Integration of Electronic and Photonic Microsystems and ASME 2015 12th International Conference on Nanochannels, Microchannels, and Minichannels, InterPACKICNMM2015. July 2016.

[18] Sridharan, R. *Stress response of tall and heavy electronic components subjected to multi-axial vibration.* Maryland: University of Maryland College Park, 2017. Print.

[19] TEAM Corporation. *TENSOR Multi Axis Test System*. Burlington, WA: n.p., Feb. 2012. PDF.

[20] Underwood, M., and Tony Keller. *Recent System Developments for Multi-Actuator Vibration Control*. San Jose, CA: n.p., 2001. PDF.

[21] Whiteman, W, and Berman, M.. *Fatigue failure results for multi-axial versus uniaxial stress screen vibration testing*. Shock and Vibration, vol. 9, no. 6, pp. 319-328, March 2002.